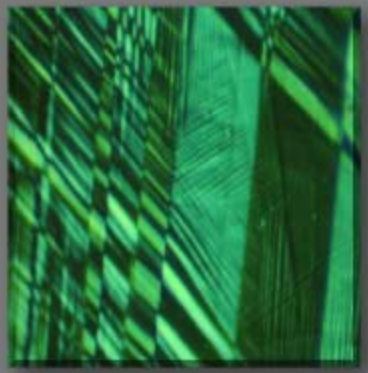

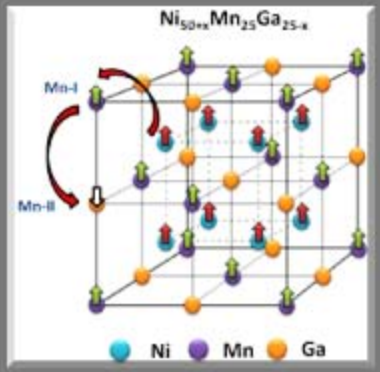

Ph. D. Thesis 2011 M. Ramudu

Ph.D. Thesis

Investigations on $Ni_{53.5}Mn_{26.0}Ga_{20.5}$ shape memory alloy and the effect of boron addition on its properties

M. Ramudu

School of Physics

University of Hyderabad

2011

Investigations on $Ni_{53.5}Mn_{26.0}Ga_{20.5}$ shape memory alloy and the effect of boron addition on its properties

A THESIS SUBMITTED FOR THE DEGREE OF
DOCTOR OF PHILOSOPHY

BY

M. RAMUDU

School of Physics
University of Hyderabad
Hyderabad – 500046, India

DECEMBER 2011

Dedicated to

my Parents

& my Teachers

DECLARATION

I hereby declare that the work reported in this thesis has been carried out by me under the supervision of ***Professor V. Seshubai***, School of Physics, University of Hyderabad, Hyderabad, India. I also declare that this has not been submitted to any University or Institution for the award of any degree/diploma.

M. RAMUDU

Date: December 08, 2011

Place: Hyderabad

CERTIFICATE

This is to certify that the research work compiled in this thesis entitled "**Investigations on $Ni_{53.5}Mn_{26.0}Ga_{20.5}$ shape memory alloy and the effect of boron addition on its properties"** has been carried out by ***Mr. M. Ramudu*** under my supervision and the same has not been submitted for the award of any degree of any University.

Dr. V. SESHUBAI

Research Supervisor
Professor, School of Physics

Date: December 08, 2011

Place: Hyderabad

DEAN

School of Physics
University of Hyderabad

ACKNOWLEDGEMENTS

I would like to express my sincere gratitude to my research supervisor ***Prof. V. Seshubai*** for her constant inspiration, continuous support during the entire course of my research work. I also admire her for the dedication that she has shown, in cultivating right concepts and igniting interest and zeal for research work.

I thank the Dean **Prof. C. Bansal**, School of Physics for enabling me to use all the central facilities of the school required for the work reported in the thesis. I also thank the former Deans of the School and other faculty of the School for their support and encouragement.

I am grateful to my doctoral committee member, **Prof. C.S. Sunandana** for the discussions and comments that helped in improving the quality of my work.

I would like to acknowledge **Dr. T. Rajasekharan**, Scientist-G, Defense Metallurgical Research laboratory, Hyderabad for his keen interest, support and suggestions at various stages of this work. Additionally, I am greatly benefited from the new ideas that emerged during discussions that I had with him.

I thank **Prof. S.N. Kaul**, Coordinator, Centre for Nanotechnology (CFN), University of Hyderabad for his suggestions during seminars and for the facilities like Physical Property Measurement System and TEM available in the centre.

I thank **Dr. Maqbool Ahmed**, PSO, Central Instrument Laboratory, University of Hyderabad for the facilities like XRD and SEM in CIL to characterize my samples. I also thank **Mr. C. S. Murthy**, Senior Scientific Officer for his interest in my work. I thank Dr. Manjunath, Mr. Pavan, Mr. Nageswara Rao, Mr. Suresh and all other technical staff of CIL for their readiness in helping me with the characterization work. I also thank Mr. Sambasiva Rao, Giri and Monto for providing me with the liquid cryogen as required during characterization of the samples.

I thank **Dr. K. Muraleedharan**, Mr. Saha, Mr. Deepak, Mr. Vijay Kumar, Dr. Gokul Lakshmi and Mr. Murali of DMRL, Hyderabad for helping me with TEM and mechanical property measurements.

I acknowledge the services of technical staff Mr. S. Satyanand, Mr. Mukanda Reddy, Mr. Srinivas, Mr. Vincent, Mr. Pentiah, Mr. Ratnam, Mr. Zaheeruddin, Mr. Ravi Shankar, Mr. Venakateswara Rao of School of Physics for their willingness to help at various stages of this work. I specially thank Mr. P. Krishna for the invaluable services rendered in connection with setting up of various experimental facilities in our lab. I also thank all the non-teaching staff, especially Mr. Abraham, Mr. G.L.N. Murthy, Mr. Anantharao, Mr. Mohan Rao, Ms. Saramma, Mr. Maschendra, Mr. Sunil etc. for their timely help at various stages of this work.

Financial assistance received in the form of fellowship from Aeronautical Development Agency and UGC-RFSMS is greatly acknowledged.

I wish to thank my seniors Dr. V.L. Kameswari, Dr. S. Santhosh; my colleagues **A. Satish Kumar**, **N. Devendra Kumar and P. M. Swaroop Raju** for their support and encouragement. I also thank my junior colleagues R. Parthasarathy, M. Mahalaxmi, S. Pavan Kumar, N. Manikanta and others at the University for their help.

I wish to acknowledge my friends Nivas, Yugi, Dileep, Lakshmi kanth, Sundara Murthy, Harinath Reddy, Shinto, Ch. Ravi Kumar, Usha, Noble, Suman, Satya and many others for their support and encouragement and also for making my stay in the campus a memorable one. I thank chaitu who made my stay colorful. I also thank my childhood friend B. Prasad for his constant encouragement. I acknowledge my friends Nagaraju, Madhavi Latha, Jaya Madhuri, Sai, Sravani and others for their help and encouragement.

I also wish to acknowledge **all my friends in School of Physics** for their cooperation in carrying out my research work and also for making my stay in the University a pleasant and beneficial experience. I also wish to acknowledge all my friends in Schools of Physics, Chemistry and Life Sciences for their cooperation in

carrying out my research work and also for making my stay in the University a pleasant and beneficial experience.

There are no words to express my gratitude towards my ***Parents*** who have borne patience and continuously supported me to make my desire a reality. I wish to extend my thanks to my brothers, sisters and in-laws.

I would like to greatly acknowledge and thank my teacher P. Sreedhar, Lecturer in Computer science, Govt. Degree College for Men, Kurnool and his family (Mrs. Kalpana and Master. Rānā) for their constant support & help in each and every aspect of my life. I also thank my post-graduate teachers for their encouragement and suggestions.

I would like to acknowledge "Kamireddy Janakamma and Rama Krishna Reddy memorial charitable trust" for the financial support. I also would like to acknowledge Sri. P. Ravindra Reddy and his family, for constantly supporting in acquiring higher studies.

Additionally, I would like to pay special respects to my aunt Late. Smt. Manikyamba for her blessings and support at times required. It is my duty to acknowledge the support received from the Komaragiri family and Lanka family. I also would like to extend my sincere thanks to Ananth, Rajiv and Vamsi for their love and affection. I would like to express my heartfelt thanks to Dr. Uma Devi, Dr. Subba Reddy, my teachers S. Chandra Sekhar Reddy and K. Srinivasulu Reddy for their valuable moral and financial support.

PLACE: HYDERABAD

DATE : December 08, 2011

(M. Ramudu)

INDEX

CHAPTER I

INTRODUCTION

CHAPTER II

EXPERIMENTAL TECHNIQUES

CHAPTER III

Investigations on $Ni_{53.5}Mn_{26.0}Ga_{20.5}$ alloy that exhibits both shape memory and magnetocaloric effects

CHAPTER IV

Influence of boron addition on the structural and microstructural properties of $Ni_{53.5}Mn_{26.0}Ga_{20.5}$ alloy

CHAPTER V

Effect of boron addition on the magnetic and mechanical properties of $Ni_{53.5}Mn_{26.0}Ga_{20.5}$ alloy

CHAPTER VI

Correlation of martensitic transformation temperatures of Ni-Mn-Ga/Al-X alloys to non-bonding electron concentration

CHAPTER VII

Summary and conclusions

Chapter 1

INTRODUCTION

1.1 Active Materials

A smart material is an engineered substance that converts one form of input energy into different form of output energy. These “active" or “smart" materials can react with a change in dimensional, electrical, elastic, magnetic, thermal or rheological properties to external stimuli such as heat, electric or magnetic-field, stress and light. In most operating regimes, smart materials have the ability to recover the original shape and properties when the external driving input is removed, which makes them suitable candidates for use in actuator and sensor applications. Smart materials can be broadly categorized into several classes based on the type of driving input and the phenomenon by which the response is produced: piezoelectric, electrostrictive, magnetostrictive, electrorheological and magnetorheological, thermal shape memory, and ferromagnetic shape memory.

The smart materials have potential to replace conventional hydraulic and pneumatic actuators. Table 1.1 shows the transduction principles or the effects that couple one domain to another. Smart materials are widely used in various commercial sensors and actuators. Major advantages of smart material actuators and sensors include high energy density, fast response, compact size, and absence of moving parts. The disadvantages of these materials are: limited strain output, limited blocking force, high cost and sensitive nature to harsh environmental conditions [1].

Table 1.1 Classification of different active materials.

Actuation mechanism	Driving Force	Max. strain	Temperature range	Band width	Examples
Piezo electric	Electric field	0.13%	253 to 473K	100 kHz	PZT $Pb(Zr_{0.5}Ti_{0.5})O_3$
Electro strictive	Electric field	0.1%	273 to 313 K	100 kHz	PMN $Pb(Mg_{1/3}Nd_{2/3})O_3$
Magneto strictive	Magnetic field	0.2%	253 to 453 K	<10 kHz	Terfenol-D $(Tb_{0.3}Dy_{0.7}Fe_2)$
Thermal shape memory	Temperature change	2%-8%	173 to 473 K	< 5 Hz	Nitinol $(Ni_{0.5}Ti_{0.5})$
Ferromagnetic Shape Memory	Magnetic field induced twin boundary motion	6-10 %	Below T_C	< 1kHz	Ni-Mn-Ga

1.2 Shape Memory Alloys

Shape memory alloys (SMA's) produce large reversible strains when subjected to heat and stress. These alloys can return to their original shape when the driving input is removed, thus behaving as if they have a "memory" of their original state. These materials undergo a phase transformation from a high temperature state called 'austenitic' phase to a low temperature state called 'martensitic' phase when sample is cooled. On application of stress to the sample existing in the twinned martensite state, deformation occurs. The material then recovers the original un-deformed shape when heat is applied. The mechanism by which these materials develop strain is by twin-boundary motion. The first discovery of shape memory effect was made in 1932 in gold-cadmium alloys and later in copper-zinc (brass) alloys in 1938. The interest in shape memory alloys increased tremendously after the discovery of a series of nickel titanium alloys by researchers at the Naval Ordinance Laboratory [2]. Nitinol (Nickel-Titanium) is one of the first shape memory alloys to find commercial applications.

Shape memory alloys like Ni-Ti, have the ability to recover plastic strain levels of up to 6% as a result of a temperature induced phase change. By heating and cooling the alloy, actuation can be achieved. However, since heating and cooling processes are relatively slow, actuation can only be achieved at low frequencies (less than 1 Hz). As a result, these materials are not suitable for primary rotor and vibration control which require much higher bandwidths. But, since these materials have high stroke and high force generation capabilities, they are suited for a variety of smart rotor applications.

1.3 Martensitic transformations

The martensitic transformation (MT) is a diffusionless phase transformation in solids, in which atoms move cooperatively, and often by a shear-like mechanism. Usually the parent phase (a high temperature phase) is cubic which has high symmetry and the martensite (a lower temperature phase) has a low symmetry. The transformation is schematically shown in Fig. 1.1.

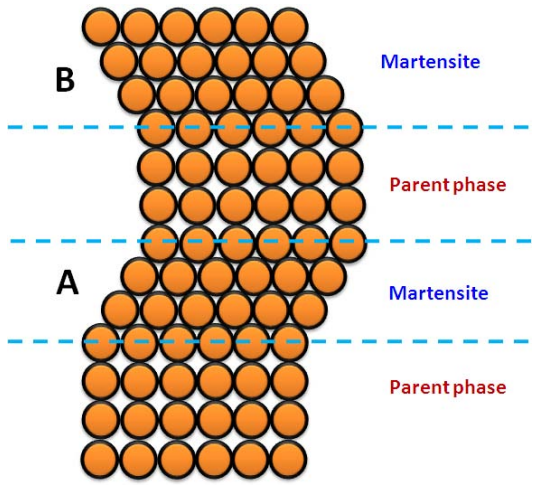

Fig. 1.1. A simplified schematic model of martensitic transformation

When the temperature is lowered below some critical point, MT starts by a shear-like mechanism, as shown in the figure. The martensites in region **A** and in region **B** have the same structure, but the orientations are different. These are called the correspondence variants of the martensites. Since the martensite has a

lower symmetry, many variants can be formed from the same parent phase. Now, if the temperature is raised, the martensite becomes unstable causing reverse transformations. If the transformation is crystallographically reversible, the martensite phase reverts to the parent phase (austenite) resulting in the original orientation.

The above example clearly shows that the characteristics of MT lie in the cooperative movement of atoms. Because of this nature, MT is sometimes called the displacive transformation or military transformation. Though the relative atomic displacements are small (compared with inter-atomic distance), a macroscopic shape change appears due to MT. This is schematically shown in Fig. 1.1. Detailed description about the thermoelastic and non-thermoelastic martensitic transformations can be found elsewhere [3].

1.4 Shape Memory Effect (SME)

An object existing in the low temperature martensitic state gets deformed on the application of stress. The stressed object regains its original shape on removal of applied stress followed by heating in a temperature interval ($A_s \rightarrow A_f$) during which the parent phase grows at the expense of the martensite. The strains (6 - 8%) describing the original deformation of the martensite are completely recovered. The recovery of the original shape is entirely due to the reverse transformation of the deformed martensite. The transformation between the low and high temperature phases is shown as a schematic in Figure 1.2.

The characteristic transformation temperatures while cooling are represented as M_s (martensite start) and M_f (martensite finish). During heating these transformation temperatures are represented as A_s (austenite start) and A_f (austenite finish). When the material is cooled from a high temperature austenite phase, a “twinned" martensite structure will form consisting of alternating rows of atoms tilted in opposite direction. The atoms form twins of themselves with respect to a plane of symmetry called as a twinning plane, or twin boundary.

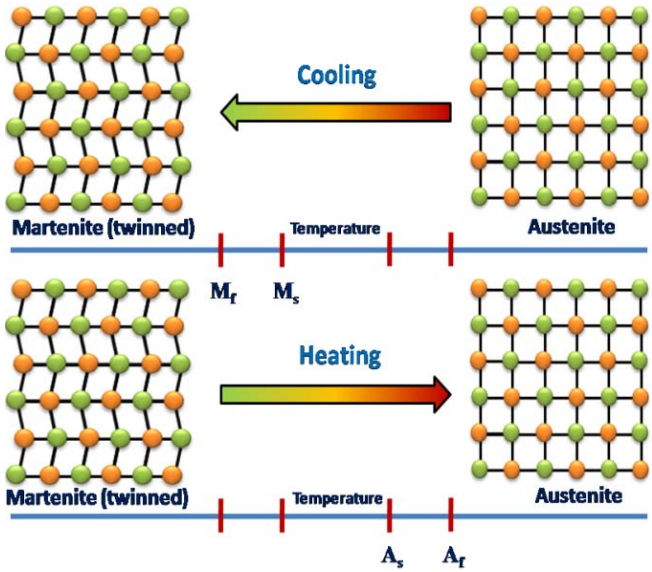

Fig. 1.2. Schematic representation of transformation between low temperature martensite and high temperature austenite phases.

When a stress is applied on the material, the twins are reoriented so that they all lie in the same direction. This process is called as “detwinning". When the material is heated, the deformed martensite reverts to the cubic austenite form, and the original shape of the component is restored. Therefore this behavior is called as “shape memory effect" since the material remembers its original shape. This entire process is shown schematically in Figure 1.3.

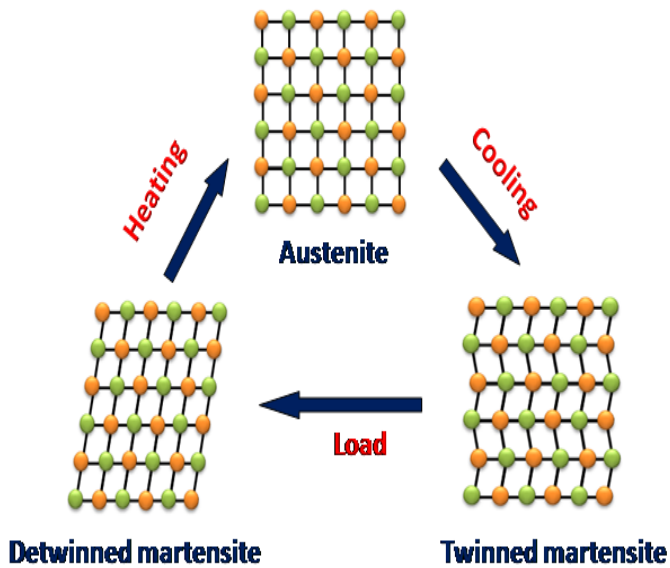

Fig. 1.3. A schematic view of the process for obtaining shape memory effect.

A single crystal of the parent phase will usually transform into 24 orientations of martensite (variants of {hkl}). But, when this mixture of many variants of martensite is deformed, the microstructure changes into a single orientation of martensite. This change occurs by the motion of martensite-martensite boundaries, during which the variant gets compatible with the applied deformation and grows at the expense of the others [4]. When a fully martensitic mixture of many orientations of martensite is deformed, one plate orientation grows at the expense of the others. The favoured martensite is that whose shear component of the shape deformation permits the maximum elongation of the specimen in the direction of the tensile axis [5]. The entire deformation is therefore due solely to martensite variant reorientation.

1.5 Ferromagnetic shape memory alloys

A major inconvenience for the practical application of the shape memory effect is the slow response of the devices inherent to the thermal control of the effect. The possibility of controlling shape memory by means of an applied magnetic field opens up a research area aimed at designing a new generation of sensors and actuators which can operate at relatively high frequencies. Additionally, since it is easier to control the magnetic field rather than the temperature, potential devices based on this effect are expected to be technologically much simpler.

A new form of magnetic-field-induced-strain (MFIS) has been observed in certain alloys that exhibit a martensitic transformation within the ferromagnetic phase. The field-induced-strain appears to arise from a mechanism different from that responsible for magnetostriction (the rotation of the magnetization direction in a material having appreciable spin-orbit coupling). This new effect is associated with the motion of twin boundaries between regions in which the magnetization direction differs and is constrained by large magnetocrystalline anisotropy. These alloys exhibit the thermoelastic shape memory effect along with field-induced

strain and hence are often called Ferromagnetic Shape Memory Alloys (FSMAs). The effect of a magnetic field on the dimensions of a magnetic material is a consequence of the interplay between structure and magnetic degrees of freedom. The strains achieved by this mechanism (up to 10% [6]) are orders of magnitude larger than those corresponding to conventional magnetostriction. Their specific feature is that there is an extra degree of freedom (the magnetic field) in addition to temperature and stress which can be tuned to achieve the desired functional effects.

The working frequency of the FSMAs is relatively high of the order ≤ 1 kHz [7, 8]. Inspired by the merits of these materials, considerable efforts have been devoted on the investigation of various aspects of these FSMAs in the past few decades [6-29]. Up to now, several alloy systems have been confirmed to exhibit the characteristics of FSMAs, including Ni-Mn-Ga [6-12], Co-Ni-Ga [13], Co-Ni-Al [14, 15], Ni-Fe-Ga [16, 17], Ni-Mn-Al [18], Fe-Pd [19-21], Fe-Pt [22], Fe-Ni-Co-Ti [23, 24] etc. Among these alloys, Ni-Mn-Ga alloys with chemical compositions close to the stoichiometric compound Ni_2MnGa are the most promising FSMAs. There are several key characteristics that make Ni-Mn-Ga alloys unique and remarkable, attracting a high degree of research interest. Ni-Mn-Ga alloys are among the first known ferromagnetic intermetallic compounds that undergo a thermoelastic martensitic transformation from a cubic $L2_1$-ordered Heusler structure to a complex martensitic structure [25, 26]. Secondly, the martensitic transformation in these alloys exhibits several active properties that are of great interest to the smart materials society, including the two-way shape memory effect [27, 28], superelasticity [29] and magnetic-field-induced strain [9, 10].

1.6 Magnetic shape memory effect (MSME)

The mechanism by which the magnetic shape memory arises is sketched schematically in Fig. 1.4. In the martensitic state, the sample is a heterophase composed by several twin-related martensitic variants (structural domains). Below the Curie temperature there are magnetic domains within each martensitic

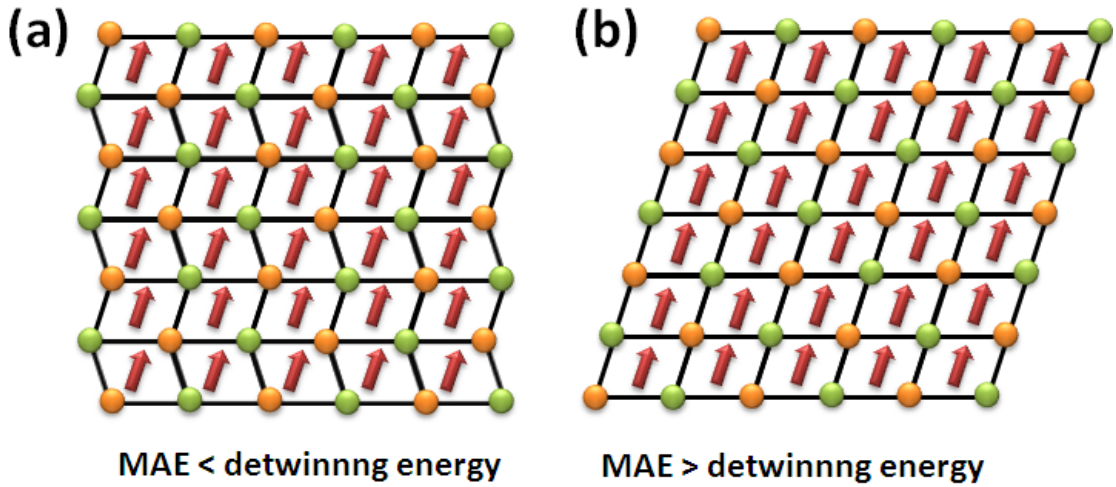

Fig. 1.4. Schematic representation of MSM effect when (a) magnetic anisotropy energy < de-twinning energy and (b) magnetic anisotropy energy > de-twinning energy.

variant with the magnetization pointing along the easy axis and organized in such a way that they minimize the magnetostatic energy [30-32]. When a magnetic field is applied, there is a tendency of the magnetic moments to align along the applied magnetic field.

If the magnetic anisotropy is small, the magnetic moments will rotate within each martensitic variant. This will result in almost no change in the sample dimensions other than those corresponding to conventional magnetostriction. However, if the magnetic anisotropy is large, rotation of magnetic domains requires a significant increase in magnetic energy. Provided that the energy to move twin boundaries is low enough, there will be a rotation of the structural domains in such a way that their easy axes become aligned with the externally applied field. In this case, the rotation of martensitic variants is promoted by the difference in the Zeeman energy between the variants and this results in a significant change in the dimensions of the sample [33]. In this process, the magnetic field plays a role similar to the mechanical stress active in conventional shape memory alloys. i.e. the application of an external field results in a large deformation of the sample. Shape memory is achieved on heating the alloy above the reverse martensitic transition temperature, where all martensitic variants disappear and the sample recovers its original shape. In magnetic alloys,

deformation is achieved by applying a magnetic field and hence this effect has been termed as magnetic shape memory (MSM).

In general, the strain achieved by the rotation of martensitic variants under an applied field is not recovered when the magnetic field is removed. It has been reported that for samples with very small strains alone can regain their shape after the applied fields are removed [9]. In addition to heating the sample, there are other ways of recovering the strain induced by applying a field. One of the approaches is to rotate the magnetic field [34]. Another approach, which is the most commonly used in magnetic shape-memory actuators, is to apply a mechanical stress perpendicular to the direction of the applied field [35-37].

Under a proper choice of the directions of the applied load and magnetic field strains as large as 10% can be obtained [6].The magnetic shape memory relies on a balance between the magnetic energy and the energy required for twin boundary motion [38]. In a general way, such a balance is expressed as

$$\Delta E \geq \epsilon_0 \sigma_{tw} \text{-------} (1.1)$$

where ΔE is the magnetic energy difference between differently oriented adjacent twin variants, ϵ_0 is the tetragonal distortion and $\sigma_{tw}$is the twinning stress [39]. If the material is magnetized to its saturation with the magnetization perpendicular to the easy axis of one variant and along the easy axis of the adjacent variant, the difference of the magnetic energy is equal to the difference of the magnetic anisotropy. Hence, the general condition for twin boundary motion is expressed as

$$\sigma_{mag} = \frac{K}{\epsilon_0} \geq \sigma_{tw} + \sigma_{ext} \text{-------} (1.2)$$

where K is the magnetic anisotropy constant and σ_{ext} is the external applied stress [31]. Equation 1.2 indicates the fact that high magnetic anisotropy and/or high twin boundary mobility are requisites for the occurrence of magnetic shape memory that will take place when the magnetic stress σ_{mag} is larger than the mechanical stress [40]. It also shows that too large external stresses will also inhibit twin boundary motion.

1.7 Structural and magnetic properties of Ni-Mn-Ga alloys

1.7.1 Phase transformations

Stoichiometric Ni_2MnGa undergoes a structural transformation upon cooling from high temperature cubic (austenitic) phase to low temperature tetragonal (martensitic phase) at 202 K. It also exhibits ferromagnetic to paramagnetic transition at Curie temperature (T_C) ~ 376 K [25]. Depending on the composition and heat treatments, the martensitic transformations can occur in

a. ferromagnetic state ($T_M < T_C$)
b. paramagnetic state ($T_M > T_C$)
c. region close to the Curie temperature ($T_M \sim T_C$).

This is of particular technological interest since combining ferromagnetic properties of martensite with thermoelastic features of the martensitic transformation allows the realization of new shape memory devices. This can be achieved either by switching of martensitic domains [9, 41] or by shifting the martensitic transformation temperature [42]. Alloys exhibiting $T_M < T_C$, $T_M > T_C$ or $T_M \sim T_C$ are investigated for their potential for applications in devices employing the magnetic shape memory (MSM) effect, the high-temperature shape memory effect (SME) and the magnetocaloric effect (MCE) [43-45], respectively.

The martensitic transition takes place when the contact between the Fermi surface and Brillouin zone boundary occurs [25]. Such a scenario implies that the change in the number of valence electrons and the alteration of Brillouin zone boundary are primary driving forces for the occurrence of structural instability in these alloys. Neglecting hybridization effects and other factors such as electronegativity difference [46], one can expect to detect a linear change of T_M with composition due to monotonous change in the number of valence electrons and in the chemical pressure, which has indeed been observed in limited composition intervals of $Ni_{2+x}Mn_{1-x}Ga$ [11], $Ni_2Mn_{1+x}Ga_{1-x}$ [47] and $Ni_{2+x}MnGa_{1-x}$ [48]. However, this picture will be no longer valid when approaching Curie point, because volume magnetostriction considerably affects crystal lattice parameters.

Phase transitions between different crystallographic modulations of martensite can be induced in off-stoichiometric Ni-Mn-Ga alloys by a change of composition, temperature or stress, or by the combination of these parameters [49]. Detailed investigations on the effect of excess Ni on T_M and T_C in $Ni_{2+x}Mn_{1-x}Ga$ system were studied. A phase diagram for $Ni_{2+x}Mn_{1-x}Ga$ system was constructed by Khovaylo *et al.* [50] from the Differential Scanning Calorimetry and magnetization measurements and is shown in Fig. 1.5.

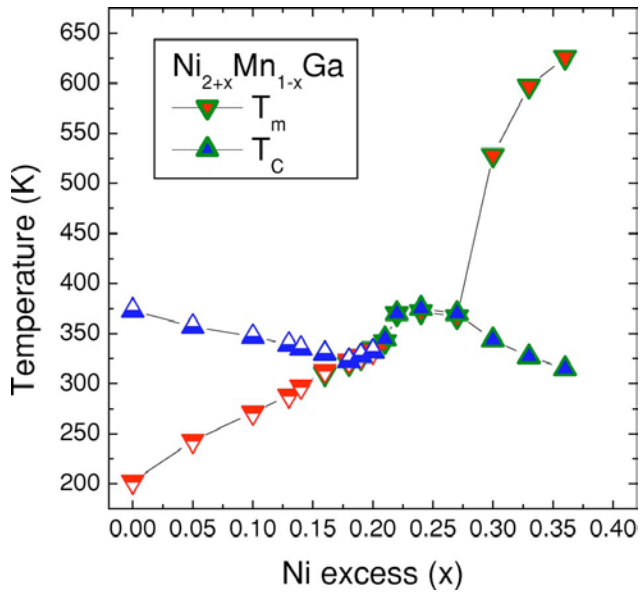

Fig. 1.5. Variation of T_M and T_C with Ni content in $Ni_{2+x}Mn_{1-x}Ga$ ($0 \leq x \leq 0.36$) system [50].

Three different regions can be distinguished from this phase diagram. The first region is characterized by the concentration of excess Ni, $x \leq 0.16$. In this region $T_C > T_M$ and the martensitic transformation takes place in the ferromagnetic state. Alloys from the second region with Ni excess $0.18 \leq x \leq 0.27$ are characterized by a coupled magnetostructural transition, i.e., $T_M \sim T_C$. Ferromagnetic transition in this compositional interval has a characteristic of a first-order phase transition, showing pronounced hysteresis on temperature and field dependence of magnetization 'M(T) and M(H)'. Such unusual magnetic properties of these alloys have been attributed to the fact that the martensitic and

ferromagnetic transitions occur simultaneously. Finally, the third region is characterized by a high martensitic transformation temperature (T_M > 550 K) and a low Curie temperature (T_C < 350 K). In this region, the Ni excess x ≥ 0.30 compounds undergo martensitic transformations in the paramagnetic state. The occurrence of martensitic transformation at high temperatures makes alloys from this region attractive for application as high temperature shape memory alloys.

At still higher contents of Ni in Ni_{50+x} $Mn_{25}Ga_{25-x}$ when x > 7, T_M remains almost a constant, which was attributed to precipitation of γ phase, which leaves the cell volume and electron concentration of the martensitic phase unaffected by further increase in Ni content. T_M increases gradually when Ni is substituted for Mn or Mn is substituted for Ga, whereas it rises much faster when Ni is substituted for Ga. [44, 47, 51]. However, the variation in T_C is marginal and in general, it decreases with increasing *e/a* for off-stoichiometric Ni-Mn-Ga alloys [50].

1.7.2 Crystal structure

Heusler alloys are ternary intermetallic compounds with the general formula X_2YZ. The Ni_2MnGa alloy, which belongs to this family, has the $L2_1$ structure at room temperature, with space group $Fm\bar{3}m$ and is schematically shown in Fig. 1.6. $L2_1$ is represented with a bcc lattice in which the Ni atoms occupy the position at the center of the cube, while the Mn and Ga atoms alternatively occupy the positions at the apexes [25]. The formation of such structure from the melt is, in principle, possible either from the fully disordered phase A2 (A2 → $L2_1$) or through the partially ordered intermediate phase B2′ (A2 → B2′ → $L2_1$), in which the Ni atoms already form the frame of the lattice, while the Mn and Ga atoms still occupy arbitrary positions. But the situation is different in Ni_2MnGa [52]. The melting point of Ni_2MnGa is ~ 1380 K. As the temperature decreases, this compound passes from the melt directly into the partially ordered phase B2′, and this phase then experiences a second-order phase transition of the disorder-order type [53].

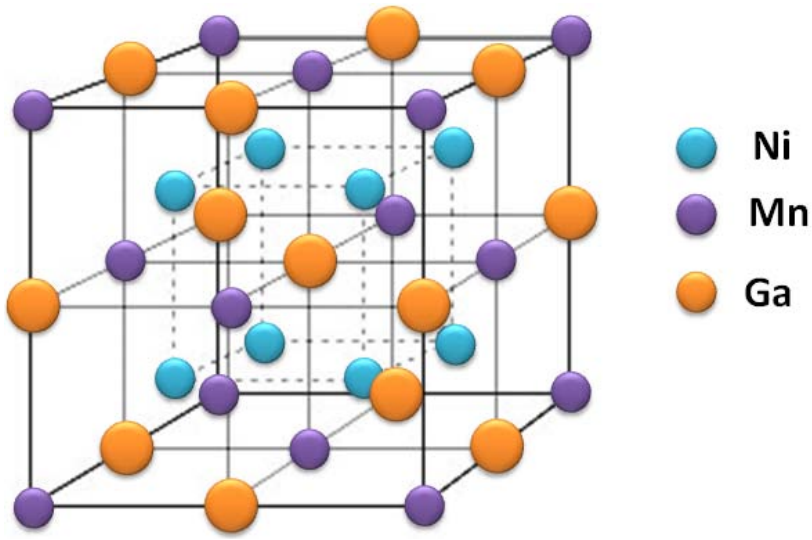

Fig. 1.6. Schematic representation of Ni_2MnGa Heusler alloy with $L2_1$ structure.

The $B2' \rightarrow L2_1$ transition temperature for Ni_2MnGa is about 1070 K. Ni_2MnGa remains in the $L2_1$ phase down to $T_M \sim 200$ K, and this Heusler alloy then undergoes a first-order phase transition to a martensitic tetragonal phase, with $c/a < 1$ having $I4/mmm$ space group. At room temperature, the cubic lattice constant *'a'* of Ni_2MnGa is 5.825 Å and the unit cell volume $V_{cub} \sim 198$ Å^3 (the number of formula units per unit cell is Z = 4). At low temperatures (at 4.2 K), the parameters of the tetragonal lattice are $a = b = 5.920$ Å and $c = 5.566$ Å, with $c/a = 0.94$, and the unit cell volume is 185 Å^3 [25].

Although the reflections observed in X-ray diffraction patterns represent only the short-range order corresponding to the B2' structure, traditionally the crystal structure of the cubic phase of the family of $Ni_{2+x+y}Mn_{1-x}Ga_{1-y}$ alloys is considered as $L2_1$ structure. In some non-stoichiometric compositions, tetragonal martensitic phases with orthorhombic and monoclinic distortions have been reported. Almost all X-ray and neutron diffraction studies involving Ni_2MnGa reveal the presence of superstructural reflections, in addition to the main reflections of the low-temperature martensitic phase. [54-56].

1.7.3 Martensitic structures in Ni-Mn-Ga alloys

The crystal structure of the martensitic phase has been found to be extremely sensitive to alloy composition. There are two kinds of distinct martensitic structures in the Ni-Mn-Ga alloys, modulated and non-modulated structures [57]. Modulated structures are mainly categorized into 5 layered (5M) and 7 layered (7M).

(a) 5M martensite

The 5M martensite was first discovered by Webster *et al.* [25] in the stoichiometric Ni_2MnGa alloy. Martynov and Kokorin [54, 58] and Fritsch *et al.* [59] reported that the crystal structure is modulated by a transverse displacive wave along the [110] direction. This may be represented as a periodic shuffling along $(110)[110]_p$ system or a long-period stacking of $\{110\}_p$ close-packed planes [54, 56]. The modulation can be directly observed in electron diffraction measurements as four additional spots between the main reflections along the [110] direction in the reciprocal space (for example, [60, 61]).

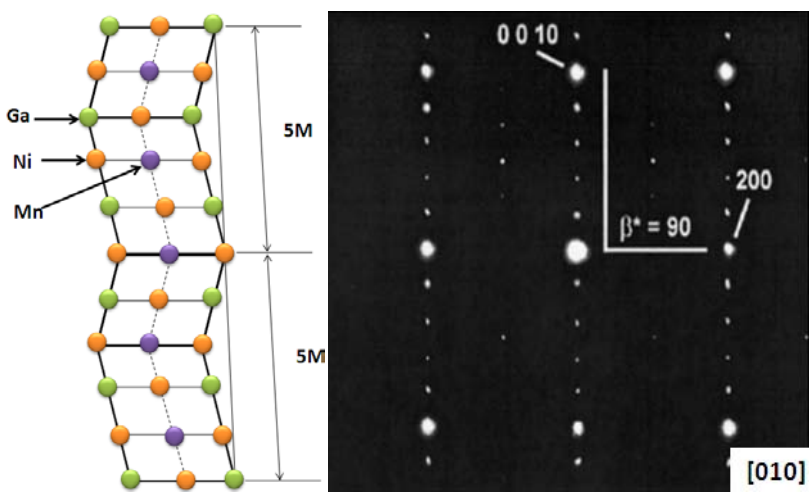

Fig. 1.7. Schematic representation of 5M martensite and the corresponding selected area electron diffraction (SAED) pattern showing the five layer modulation [56].

The average lattice is approximately tetragonal or monoclinic with a short *c*-axis, with ratio $c/a < 1$ (the cubic coordinates). The schematic representation as

well as the Selected Area Electron Diffraction (SAED) pattern of 5M martensite is shown in Figs. 1.7(a) and (b) respectively.

(b) 7M martensite

Martynov and Kokorin [54, 58] found the 7M martensite. The average lattice is approximately orthorhombic with $c/a \approx 0.89$ and $c/a<1$ (in cubic coordinates) with a monoclinic distortion as observed by Sozinov *et al.* [62]. In the orthorhombic coordinates, the lattice of the 7M martensite is seen as a monoclinic one with $\beta \approx 93\text{-}94^{o}$ [56].

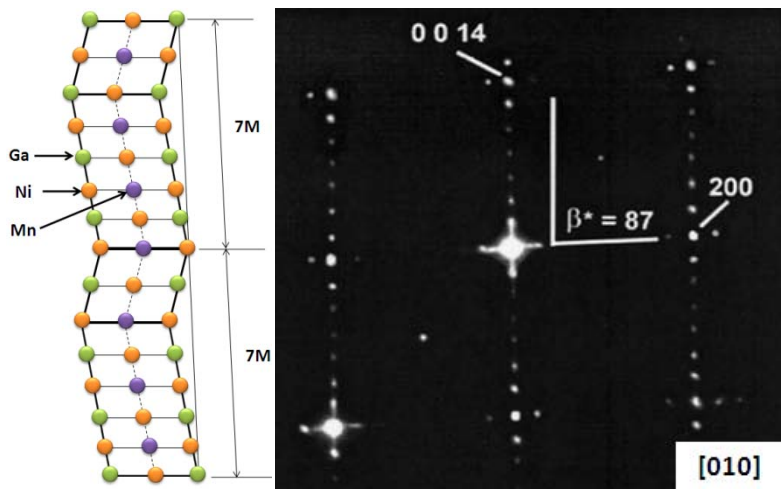

Fig. 1.8. Schematic representation of 7M martensite and the corresponding SAED pattern showing the seven layer modulation [56].

In the diffraction studies, the 7M martensite results in a pattern where the distance between the main reflection along [110] direction in reciprocal space is divided into seven parts by six additional spots, as shown by Fritsch *et al.* [59] and others [60] as well as by Lanska and Ullakko [48, 63]. Sozinov *et al.* [6] observed that the seven-layer modulation takes place along the (110)[110]*p* system. They established that, in the 7M martensite the easy axis of magnetization is the shortest *c*-axis, while the longest *a*-axis is the hard axis to magnetize and the magnetization of the *b*-axis is the intermediate one. The schematic representation of 7M martensite and the corresponding SAED pattern are shown in Figs. 1.8. (a) and (b) respectively.

(c) Non-modulated martensite

The non-modulated tetragonal (T) martensite of the Ni-Mn-Ga system was found [54] to crystallize in a tetragonal structure with a long *c*-axis and *c/a* >1 (in cubic coordinates). Non-modulated T martensite phase is the most stable one among the martensitic structures in Ni-Mn-Ga alloys [11, 64-66]. The SAED pattern of non-modulated T martensite is shown in Fig. 1.9.

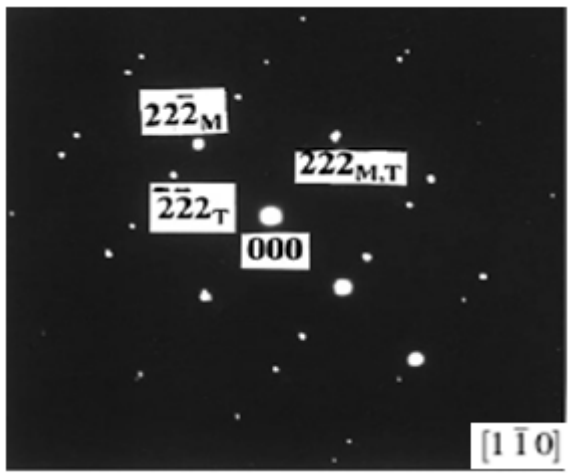

Fig. 1.9. SAED pattern in non-modulated (NM) tetragonal martensite [44]

The crystal structure of martensitic phases depends on the composition as well as on the heat treatment [67, 68]. Deviations from the stoichiometry causes different types of modulations as have been reported by many researchers [48, 56]. Keeping Ni constant and by increasing Mn content in $Ni_{50}Mn_{25+x}Ga_{25-x}$ (x = 0 - 5), Jiang *et al.* [47] have shown that the crystal structure changes from cubic to tetragonal 5M to orthorhombic 7M. The effect of composition on the crystal structures of Ni-Mn-Ga alloys was studied by many researchers [48, 69]. The crystal structure of martensitic phases (5M, 7M and NM) have been classified to be correlated to the electron per atom (*e/a*) ratio. Apart from the existence of 5M and 7M modulations, Richard *et al.* have shown that some mixed phase modulations can exist [69]. The modulated crystal structures play a major role in achieving high magnetostrains in Ni-Mn-Ga alloys and this depends on the composition.

1.7.4 Magnetic properties

(a) Saturation magnetization

Webster *et al.* [25] showed that the magnetic moment in the Heusler alloy Ni_2MnGa is localized primarily on the manganese atoms, $\mu_{Mn} \approx 4.17\ \mu_B$, while the magnetic moment on nickel atoms $\mu_{Ni} \leq 0.3\ \mu_B$. Deviation from the stoichiometry leads to the change in magnetization of the alloys. Jiang *et al.* [47] have shown that the magnetization decreases with the increase in Mn content in $Ni_{50}Mn_{25+x}Ga_{25-x}$ (x = 0 to 5). Temperature dependence of saturation magnetization (M_{sat}) of the $Ni_{2+x}Mn_{1-x}Ga$ alloys [70] have shown that M_{sat} decreases with increasing temperature and exhibits a pronounced change near the martensite to austenite transformation temperature. The magnetic moment of these alloys was found to decrease linearly with substitution of Mn by Ni. The decrease in the M_{sat} in off-stoichiometric Ni-Mn-Ga alloys is mainly dependent on the composition and the site occupancy of magnetic atoms [70, 71]. In the case of off-stoichiometric Ni- rich compositions of Ni-Mn-Ga, Richard *et al.* [72, 73] have shown that for Ni concentration of 50 at.% or more, the excess Ni displaces the Mn atoms from their regular sites (in Mn sublattice) and couple ferromagnetically with Mn moments. The excess Mn and the displaced Mn atoms occupy vacant Ga sites and couple antiferromagnetically to the Mn at regular sites. Jie *et al.* [74], from Density Functional Theory (DFT) calculations supported this view based on the preference for the smaller lattice distortions and lower-energy electronic structure.

(b) Magnetocrystalline anisotropy

Magnetocrystalline anisotropy can be considered as the determining parameter for achieving giant strains induced by a magnetic field in shape memory ferromagnets. The two main sources of the magnetic anisotropy energy (MAE) are the spin-orbit coupling and the magnetic dipole-dipole interactions. The dipole-dipole induced anisotropy depends on the shape of the sample and in many cases it is small compared to the spin-orbit coupling. Magnetic anisotropy

depends on composition and the type of martensitic structure, i.e. on the magnitude of the lattice distortion.

The stoichiometric Ni_2MnGa polycrystalline alloy is cubic austenite at ambient temperature. For alloys of Ni-Mn-Ga, magnetic anisotropy constant (K_1) is $\sim 2.5 \times 10^5$ J/m^3 in martensitic phase which is much higher than in austenite phase. Studies on magnetocrystalline anisotropy (K_u) of single crystals in $Ni_{2+x+y}Mn_{1-x}Ga_{1-y}$ system with different compositions, showed that the values of K_u at room temperature were 1.7×10^5 J/m^3 for $Ni_{48}Mn_{31}Ga_{21}$ [75] and 2.48×10^5 J/m^3 for $Ni_{49.7}Mn_{28.7}Ga_{21.6}$ [76].

1.7.5 Magnetocaloric effect

Magnetocaloric effect (MCE) occurs in a magnetic material due to the interdependence of thermal and magnetic properties [45]. They are commonly induced by the application or removal of an external magnetic field and is measured as a temperature change when the field is adiabatically swept (ΔT_{ad}), or as an entropy change when the process is isothermal (ΔS_M).

At constant pressure, the entropy of a magnetic solid (S), which is a function of both the magnetic field strength (H) and the absolute temperature (T) is given as:

$$S(T, H) = S_M(T, H) + S_{Lat}(T) + S_{El}(T) \text{ -------(1.3)}$$

Where S_M denotes magnetic entropy S_{Lat} denotes lattice entropy and S_{El} denotes electronic entropy.

ΔT_{ad} and ΔS_M are correlated with the magnetization (M), the applied magnetic field (H), the heat capacity at constant pressure (C_P), and the absolute temperature by one of the fundamental Maxwell's relations [77]

$$\left(\frac{\partial S(T,H)}{\partial H}\right)_H = \left(\frac{\partial M(T,H)}{\partial T}\right)_H \text{-------(1.4)}$$

Which for an isothermal-isobaric process after integration yields

$$\Delta S_M\,(T, \Delta H) = \int_{H_1}^{H_2} \left(\frac{\partial M\,(T,H}{\partial T}\right)_H dH \text{ -------(1.5)}$$

Eq. (1.5) indicates that the magnetic entropy change is proportional to the derivative of magnetization with respect to temperature at constant field and to the magnetic field change. The magnetocaloric effect is computed from ΔS_M the detais of which can be found in literature [78].

Optimum magnetocaloric properties were shown to occur when both the martensitic and ferromagnetic transitions occur close to each another [79]. Several researchers have reported the observation of magnetocaloric effect in off-stoichiometric Ni-Mn-Ga alloys [42, 43, 45]. More recently, other Ni–Mn-based Heusler alloys have been shown to exhibit large magnetocaloric effects. As opposed to the case of Ni–Mn–Ga mentioned above, these alloys exhibit an inverse effect for all studied magnetic fields [45, 80].

1.8 Effect of alloying with other elements

Ni–Mn–Ga alloys exhibit the highest MFIS among the magnetostrictive materials (up to 10%) [10] and hence are attractive for practical application as sensors and actuators. However, the low values of both transformation temperatures (especially T_C) and poor mechanical properties limit the use of these FSMAs in practical devices. The great prospects for application as magnetic and magneto-mechanical actuators and sensors have encouraged efforts to find new alloy compositions with correct martensite crystal and magnetic structures. In particular, alloys with higher transformation temperatures are of special interest. One possible method of increasing the operating temperatures as well of modifying the properties of a given alloy is alloying the ternary materials with additional elements. In particular, addition of small amounts of magnetic atoms like Co, Fe etc. to Ni–Mn–Ga alloys has evolved as an efficient way to modify both the T_M and T_C. Most of the literature is devoted in studying the effect of adding an element to Ni-Mn-Ga on T_M and T_C. A brief description of the effects of adding Co, Fe and a few other elements are described in the subsequent sections.

1.8.1 Effect of Co and Fe on the properties of Ni-Mn-Ga alloys

Many authors have studied the effect of Co on T_M and T_C in the literature [81-90]. Depending upon which site in Ni-Mn-Ga the Co atom gets substituted, the increase or decrease of electron concentration takes place. As Co is a magnetic atom, the exchange interactions between the magnetic atoms in the system will show an effect on T_C of the compound.

Sanchez-Alarcos *et al.* [87] have investigated the effect of Co addition on the phase transformation temperatures (martensitic and Curie point) and crystal structure of $(Ni_{50.26}Mn_{27.30}Ga_{22.44})_{100-x}Co_x$ (x = 0, 2, 4, 6) as well as on alloys having different Ni/Mn/Ga ratios with a fixed amount of Co. It has been established that in Ni–Mn–Ga–Co alloys, T_M increases with the substitution of Co for Mn or Ga site [84, 88-90] and decreases with the substitution of Co for Ni [83, 88-90]. On the other hand, T_C increases with the substitution of Co for Ni / Ga [83, 88-90] and shows a non-monotonous behavior when Mn is substituted by Co [84, 89].

The effect of addition of magnetic atom Fe to Ni-Mn-Ga system has drawn more interest in recent times [91-98]. Liu *et al.* [91] systematically investigated the effect of Fe on T_M and T_C in $Ni_{50.5}Mn_{25-x}Fe_xGa_{24.5}$ (x = 0-17) and $Ni_{50.4}Mn_{28-x}Fe_xGa_{21.6}$ (x = 0-18) alloys. Substitution of Fe for Mn decreased T_M in both the systems. The *e/a* dependence could not simply explain the T_M variation in these systems. Kikuchi *et al.* [98] have studied the effect of replacing Ga with Ni by keeping Mn and Fe content constant ($Mn_{12.5}$ and $Fe_{12.5}$) on structural and magnetic transitions of $Ni_{50+x}Mn_{12.5}Fe_{12.5}Ga_{25-x}$ ($0 \leq x \leq 5.5$) alloys. T_M was found to increase while T_C decreases with x. Following points can be drawn from the detailed investigations on the effect on structural and magnetic transitions by Fe addition to Ni-Mn-Ga system.

When Fe is substituted for Ni, T_M decreases as the amount of Fe increases (since *e/a* decreases) consistently with the behavior observed in ternary Ni–Mn–Ga alloys. The temperature of the ferromagnetic transition T_C increases with

increasing Fe content. When Fe is substituted for Mn, T_M decreases and T_C increases with increasing Fe concentration where as e/a increases. This behavior is unexpected from the scaling of the martensitic transition temperatures with the electron concentration. It has been reported in the literature [88, 91-93] that the correlation of T_M with e/a is unclear for the case of Mn getting replaced with Fe

1.8.2 Effect of other elements on the properties of Ni-Mn-Ga system

Substitution of other transition metals in Ni-Mn-Ga system has been reported to alter the transition temperatures and physical properties of the materials significantly [83, 88, 90, 93, 95, 98]. Substitutions of other elements like Ge, Si, In and C in Ni-Mn-Ga system have also been reported with regard to their effect on T_M [88, 99]. Rare-earth elements when introduced into Ni-Mn-Ga show low solubility and segregate at the grain boundaries [100]. Variation in T_M is found to increase with e/a ratio. Addition of Tb in $Ni_{49}Mn_{29}Ga_{22}$ alloy is reported to cause segregation of Tb-rich, Mn-poor phase at the grain boundaries resulting in an enhancement of Mn content in matrix phase [101]. The studies on the effect of rare -earth elements like Sm, Gd, Y and Dy on the phase transformations, microstructure and mechanical properties have been investigated [100, 102-107]. Of recent, the effect of adding a light element like boron on the properties of Ni-Mn-Ga system has gained interest [108-111]. Boron seems to alter the transformation temperatures as well as the structure and magnetic properties of the parent compound, as discussed below.

1.8.3 Effect of Boron substitution and Boron addition

Boron, when added to Ni-Mn-Ga, can occupy either the regular site in the crystal lattice or an interstitial site due to its small size. Recently, the effect of substituting boron for Mn in $Ni_2Mn_{1-x}B_xGa$ [108] and for Ga in $Ni_2MnGa_{1-x}B_x$ [109] alloys on the structural and magnetic transformation temperatures has been reported. In the former system, both T_M and T_C decreased with B substitution. For $x > 0.12$, no martensitic phase was observed. The saturation magnetization at 5 K

was found to decrease with B content and has been attributed to be a result of replacing magnetic Mn atom by non-magnetic boron atom. Substitution of B for Ga in the latter system caused an increase in T_M and a marginal reduction in T_C. The saturation magnetization at 5 K decreased by 20% for the alloy with x = 0.25 and is attributed to a decrease in the lattice parameters causing a reduction in Mn-Mn distance. Similar trend in T_M and T_C has been observed on substitution of B for Sb in $Ni_{50}Mn_{36.5}Sb_{13.5-x}B_x$ system [110]. The reduction in T_M discussed above on substitution of B for Mn in $Ni_2Mn_{1-x}B_xGa$ system follows the general trend reported in literature that T_M increases with an increase in electron concentration (e/a). However, increase in T_M observed in the other two systems where B is substituted for Ga or Sb could not be explained on similar lines.

The effect of boron addition up to 5 at.% in $Ni_{46}Mn_{43}Sn_{11}$ system [111] has been studied. It is reported that the $L2_1$ crystal structure is retained even with B addition, but a small increase in the lattice parameters is observed which is attributed to the occupation of interstitial sites by B. Addition of 5 at.% B to $Ni_{46}Mn_{43}Sn_{11}$ alloy causes an increase in T_M appreciably while T_C increases marginally. Addition of more than 3 at.% B is found to result in multi-phase system containing Mn_2B phase [111]. There are no reports in literature on the effect of boron on the microstructural features of Ni-Mn-Ga alloys. Hence the possibility of correlating the changes in transformation temperatures and magnetic properties to microstructural alterations brought about by the introduction of boron has not yet been explored. The effect of boron on the superstructural ordering and shape memory properties in Ni-Mn-Ga alloys is also yet to be investigated.

1.8.4 Role of electron/atom ratio on martensitic transformation temperatures

It is reported in the literature that the compositional dependence of the martensitic transition temperature T_M in Ni-Mn-Ga alloys is related to the valence electron concentration e/a (Hume-Rothery mechanism [65]). The martensitic

transition takes place when the contact between the Fermi surface and Brillouin zone boundary occurs [25]. Such a scenario implies that the change in the number of valence electrons and the alteration of Brillouine zone boundary are primary driving forces for the occurrence of structural instability in these alloys. The correlation of electron per atom (e/a) ratio to the martensitic transformation temperature T_M of the Ni-Mn-Ga alloys was fist suggested by Chernenko [65]. Electron concentration was calculated assuming the following configurations of the valence electrons and their number per atom (in brackets): for Ni: $3d^8 4s^2$ (10); for Mn: $3d^5 4s^2$ (7);for Ga: $4s^2 4p^1$ (3); respectively.

A typical example of calculation of e/a for $Ni_{50}Mn_{25}Ga_{25}$ compound is given below:

$$\frac{e}{a} = \frac{\big((Ni\ at.\% * 10) + (Mn\ at.\% * 7) + (Ga\ at.\% * 3)\big)}{(Ni\ at.\% + Mn\ at.\% + Ga\ at.\%)}$$

$$= \frac{\big((50 * 10) + (25 * 7) + (25 * 3)\big)}{(50 + 25 + 25)}$$

$$= 7.5$$

Variation of T_M with composition and e/a have been reported by several authors in off-stoichiometric Ni-Mn-Ga alloys. It has been observed that T_M varies linearly with e/a [47, 48, 50, 65]. In alloys with $e/a \leq 7.7$, T_M increases with e/a, with a coefficient of ~ 900 K $(e/a)^{-1}$, while for alloys with $e/a \geq 7.7$ this coefficient is of the order of ~ 500 K $(e/a)^{-1}$ [112].

Wu *et al.* [66] have investigated the effect of composition on T_M of 38 off-stoichiometric compounds of Ni-Mn-Ga system. The dependence of T_M on e/a has been formulated by taking the at.% of Ni, Mn and Ga as:

T_M (in K) = 25.44 Ni (at.%) – 4.86 Mn (at.%) – 38.83 Ga (at.%).

Ma *et al.* [201] have studied the effect of excess Ni on phase transformations in Ni_{50+x} $Mn_{25}Ga_{25-x}$ (x = 2 – 11). Nearly linear increase of T_M (~358 K) with Ni content (increase in *e/a*) was observed when x < 7. But when x > 7, the T_M remains almost constant. From the crystal structure and microstructural studies, it was found that for x > 7, the cell volume and *e/a* of the martensitic phase was not affected by increase in Ni content due to the formation of the γ-phase. The variation of T_M with Ni content was correlated to the changes in size factor, *e/a* and precipitation of γ-phase.

The *e/a* [65, 113] and the size factor [44, 113, 114] were thought to be the means by which composition influences the T_M in Ni-Mn-Ga alloys. From a systematic investigation on the effect of substituting Si, Ge, C and Co for Ga in off-stoichiometric Ni-Mn-Ga alloys, Chen *et al.* [100] suggested that electron density (*n*) is an appropriate parameter to describe the way composition influences T_M compared to size factor and *e/a*. The electron density (*n*) was defined as

$$n = \frac{(e/a)*n_1}{V_{cell}} \text{-------(1.6)}$$

where V_{cell} is the volume of the unit cell in the austenite state, n_1 represents the average number of atoms contained within a unit cell.. Apart from these factors, the grain size and atomic order of parent phase was suggested to affect T_M [115-117].

In the alloy systems $Ni_{50.5}Mn_{25-x}Fe_xGa_{24.5}$ (x = 0-17), $Ni_{50.4}Mn_{28-x}Fe_xGa_{21.6}$ (x = 0-18), $Ni_{48.7}Mn_{30.1-x}Fe_xGa_{21.2}$ (x = 0, 2, 5, 8 and 11) and $Ni_2Mn_{1-x}Fe_xGa$ ($0 \leq x \leq 1$) [91-93] where Fe is substituted for Mn, it is reported that T_M decreases monotonously with the increase in *e/a*. In these systems, a linear dependence of T_M with *e/a* was not observed. The decrease of T_M with increase in *e/a* in Ni-Mn-Ga-Fe alloys is unexpected from the scaling of the martensitic transformations with *e/a*. From the above results, it was suggested that apart from *e/a* other parameters like size factor [113], magnetic interactions [91, 85] and sites occupied in the crystalline structure [95] affect the phase stability.

In $Ni_2MnGa_{1-x}In_x$ [118], increasing In content results in a linear decrease of T_M. Since In and Ga are isoelectronic, substitution of Ga with In is not expected to change the net conduction electron density. Therefore the decrease in T_M and T_C cannot be explained in terms of *e/a*. The decrease of T_M with constant *e/a* is attributed to an increase in the cell volume by substitution of larger ionic radius of In. Similarly, isoelectronic substitution of Al for Ga is found to decrease T_M in $Ni_{54}Mn_{25}Ga_{21-x}Al_x$ (x = 0, 4, 18 and 21) system [119] and size factor was considered to be the reason for decrease in T_M in these systems.

The above results reveal that a systematic dependence of T_M on *e/a* is observed in Ni-Mn-Ga and Ni-Mn-Ga-Co systems, where as for Ni-Mn-Ga-Fe, $Ni_2MnGa_{1-x}In_x$ and $Ni_{54}Mn_{25}Ga_{21-x}Al_x$ anomalous behavior is reported. The reasons for the observed anomalies have been attributed to the factors like size factor, magnetic interaction and the site occupancy of various atoms in the crystal structure, other than electron concentration to play a role in determining the martensitic transformations [44, 85, 91, 113, 115-119].

1.9 Microstructural and mechanical properties

1.9.1 Microstructural properties

The performance of FSMAs especially the MSME and mechanical behavior, is strongly dependent on the microstructure of these alloys. Hence, it is very important to have a good understanding of the microstructural characteristics of these FSMAs. There are only scattered investigations on the microstructure of Ni-Mn-Ga alloys available. The microstructure of the martensitic phase is a result of a temperature-induced martensitic transformation and consists of an aggregate of elastically self-accommodated martensitic variants [56] which account for the minimization of strain energy during martensitic transformation.

The temperature dependence of microstructure in Ni_2MnGa at 202 K, above and below 202 K was investigated by Webster *et al.* [25] using optical microscopy. Above 202 K, faint grain boundaries were observed. At 202 K, the formation of martensitic plates was observed and below 202 K, it was observed

that the martensitic plates grew over the whole surface. From optical microscopy studies, typical morphologies of three kinds of martensites 5M, 7M and NM were reported by Jiang *et al.* [47]. There is an obvious difference in the twin widths for the three kinds of martensites. Twin widths were found to be wider for 5M, finer for 7M and intermediate for NM. Ullakko *et al*. [120] have observed typical optical microstructure of $Ni_{49.6}Mn_{28.4}Ga_{22.0}$ which indicate that the width of the martensitic bands varied from a few microns to hundreds of microns. Some of the martensitic bands showed presence of fine internal structure. The effect of excess Ni on the microstructural features in $Ni_{50+x}Mn_{25}Ga_{25-x}$ (x = 2 – 11) alloys was reported [44]. With Ni content x > 7, formation of γ phase has been observed which increases with increase in Ni content. Crossing twins of different sizes with twin variant widths mostly ranging from 6 to 10 μm in nickel rich $Ni_{53.5}Mn_{26.0}Ga_{20.5}$ (monoclinic 7M) [121] are observed at different locations of the sample. The formation of a large variety of twin modes, like parallel bands, twins within twins and crossing twins, throughout the sample is attributed to low residual stresses in the martensitic phase.

Boron introduction into Ni_3Al [122] and Ti-Pd-Ni [123] compounds is known to cause considerable changes in the microstructures which in turn alters their mechanical properties [122-124]. It has been suggested that the boron has strong tendency to segregate to grain boundaries. It is well known that boron is very beneficial in improving room temperature ductility of $L1_2$ type Ni_3Al ordered intermetallics which are inherently brittle [125]. This improvement in ductility has been attributed to boron segregation at the grain boundaries. The boron addition is believed to cause grain size refinement in addition to grain boundary strengthening.

1.9.2 Microhardness

The hardness of a material is a measure of its resistance to penetration by an indenter. Hardness is also a measure of strength and often has the units of

stress [126]. Microhardness study has been carried out by Liu *et al.* in order to reveal the mechanical state of the Ni-Mn-Ga alloys [127]. Using Vickers Hardness (HV_5) measurements, microhardness studies were carried out on Ni–Mn–Ga alloys of three different crystal structures: (1) $Ni_{51.8}Mn_{25.5}Ga_{22.7}$ (Cubic austenite), (2) $Ni_{50.7}Mn_{28.4}Ga_{20.9}$ (5M) and (3) $Ni_{50.7}Mn_{28.4}Ga_{20.9}$ (NM-T), $Ni_{51.7}Mn_{27.7}Ga_{20.6}$ (NM-T) at ambient temperature. The measured hardness values for Cubic, 5M and NM-T samples are 275 ± 1.3, 240 ± 2.7, 213 ± 1.0 and 208 ± 4.4 respectively.

In the measurement of $Ni_{51.7}Mn_{27.7}Ga_{20.6}$ alloy, a new surface relief around the indentation of the diamond tip was observed, indicating that it was easy for the structure of this alloy to undergo twin variant redistribution. Micro-cracks were observed around the indentation in the measurement of alloy with 5M martensite, suggesting the brittleness of this alloy. The highest microhardness value observed for the cubic austenite alloy, has been directly correlated to high stress values needed for induced martensite formation [127]. However, it should be understood that the recorded microhardness values of the studied Ni–Mn–Ga alloys might not reflect the bulk alloy properties. This is due to the fact that the deformations under indentation were partially recoverable. Therefore, the recorded microhardness values can be considered only as relative factors for a mechanical state assessment.

Mechanical properties like hardness [92], fracture behavior [128], compressive stress-strain behavior and MFIS measurements [97] were carried out in Fe-doped Ni-Mn-Ga alloys. From the Vickers micro-hardness studies in $Ni_{48.7}Mn_{30.1-x}Fe_xGa_{21.2}$ [92], it is shown that hardness increases abruptly with increasing Fe content (from 0 to 5 at.%) but the overall change is small (from 5 to 11 at.%).

1.9.3 Compressive stress-strain

Due to the brittleness of the Ni-Mn-Ga alloys, most of the investigations on mechanical behaviors are focused on the compressive properties of these alloys. Among these investigations, many have studied the stress-strain behavior only in

the stress region needed for the twin boundary motion [130-133], while studies were limited to the compressive properties when whole stress regions were considered [134]. A schematic illustration of the compressive stress-strain curve of Ni-Mn-Ga single crystals is shown in Fig. 1.10.

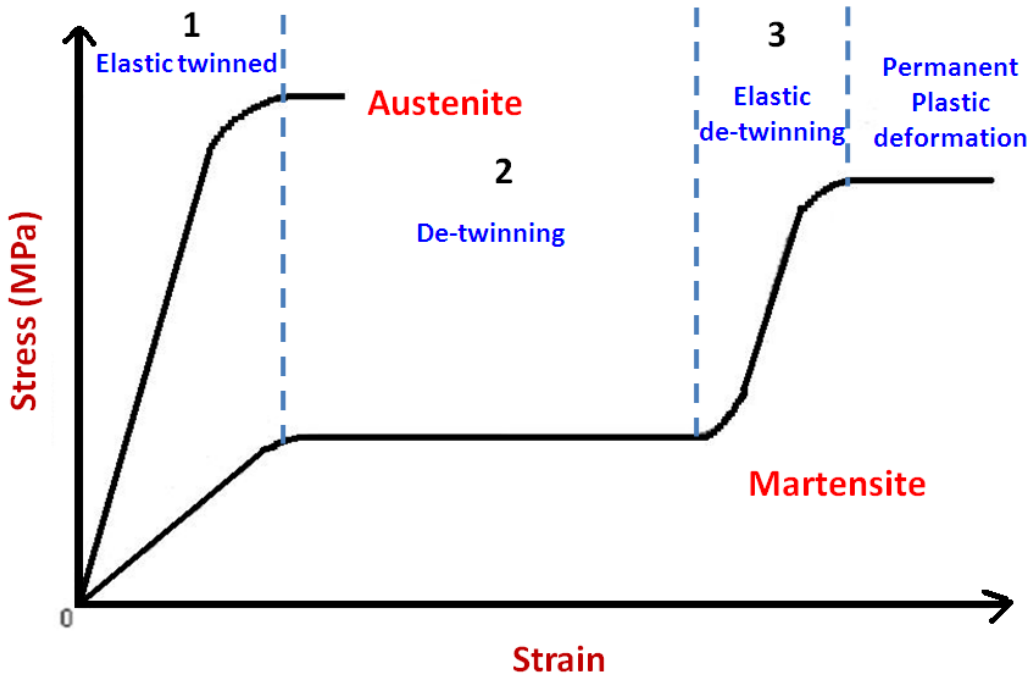

Fig. 1.10. Schematic representation of stress-strain curves showing different regimes governed by different mechanisms in martensitic and austenite states.

The Ni-Mn-Ga single crystal whose initial microstructure consists of self-accommodated multivariants is compressed under an applied uniaxial stress. As the stress is increased, a region of elastic deformation of the multivariants occur where the strain increases linearly with stress, the region between 0 and 1 in Fig. 1.15. At a critical stress level, σ_{cr}, the martensitic twin boundaries become mobile and the reorientation of martensitic variants (i.e. detwinning) starts. Since these twin boundaries can move easily, the slope of this region (indicated as the region between 1 and 2 in the figure) is very small and generally there appears a characteristic stress plateau in the stress-strain curve. The material undergoes an apparent plastic deformation in this region. However, this plastic deformation due

to the twin boundary motion can be recovered by applying proper stress and/or magnetic fields, or by heating the sample to the temperature above its martensitic transformation temperature (i.e. by reverse transformation).

After the completion of detwinning process, the elastic deformation of the fully reoriented variant begins. The slope of the stress-strain curve in this region (the region between 2 and 3 in the figure) increases and becomes much larger than that in the detwinning region. Eventually, when a limiting value of strain is reached, slip begins to occur and the material deforms plastically. The plastic strain in this region is permanent and cannot be recovered. Thus, there are two distinct yield points in the stress-strain curve. The first occurs just before twin boundary motion is activated and the second occurs at the onset of slip long after the material has been completely detwinned.

Okamoto *et al.* [38] have reported the compressive stress-strain properties in Ni_2MnGa (10M), $Ni_{2.02}Mn_{1.09}Ga_{0.89}$ (14M) and $Ni_{2.14}Mn_{0.92}Ga_{0.94}$ (2M) single crystals at 160 K, 300 K and 300 K respectively. It shows that the stress required for martensitic re-orientation is less than 4 MPa for 10M and 14M phases, where as more than 10 MPa is required for 2M martensitic phase. Xu *et al.* [133] investigated the room temperature compressive properties of the $Ni_{54}Mn_{25}Ga_{21}$ single crystal with $T_M \sim 533$K. The compressive strain is as large as 20.5% and the compressive strength reaches 845 MPa. Shape memory effect of 6.1% and a recovery ratio of 93% has been observed in this alloy. Ma *et al.* [44] studied the SME of $Ni_{50+x}Mn_{25}Ga_{25-x}$ ($x \geq 4$) in single crystalline specimens. Decrease in SME from 6.1% to 0% as well as strain recovery ratio from 93.8 to 0% respectively has been observed for x = 4 to x = 11 alloys. The decrease in both these effects is attributed to the formation of γ phase which increases with the Ni content. From the compressive stress-strain properties of $Ni_{49.2}Mn_{29.6}Ga_{21.2}$ and $Ni_{52.1}Mn_{29.3}Ga_{20.6}$ single crystal alloys [134], it is revealed that the twinning stresses required to move the twin boundary is relatively small of about ~ 2 MPa for $Ni_{49.2}Mn_{29.6}Ga_{21.2}$ and ~ 15-20 MPa for $Ni_{52.1}Mn_{29.3}Ga_{20.6}$. Cheng *et al.* [135]

have studied the effect of repeated application of mechanical forces on the mechanical behavior of single crystalline Ni-Mn-Ga alloys at different temperatures.

Gaitzsch *et al.* [136, 137] have reported the effect of training on the mechanical properties in textured polycrystalline $Ni_{50}Mn_{29}Ga_{21}$ (5M) and $Ni_{50}Mn_{30}Ga_{20}$ (7M) alloys. During the mechanical training, the twin microstructure is changed causing coarsening of twins which increases the internal stress. This resulted in an enhanced strain recovery with increasing number of training cycles. SME of 1.6% and a strain recovery ratio of 89% have been reported in polycrystalline Ni-rich $Ni_{53.5}Mn_{26.0}Ga_{20.5}$ alloy with 7M monoclinic crystal structure at room temperature [121], which forms part of the present work and is discussed in Chapter 3.

1.9.4 Applications

Ni-Mn-Ga alloys have attracted wide attention for a variety applications due to the multifunctional nature of their properties like magnetic field induced strain, magnetocaloric effect and high temperature shape memory effect. Depending on the temperature regime between T_M and T_C different applications are realized. When $T_M < T_C$, the materials can be used for actuator and sensor applications [112, 138]. The alloys with coupled transformation ($T_M \sim T_C$) have potential for application as magnetic refrigerants [45, 140]. The alloys possessing high martensitic transformation temperature ($T_M > 400$ K), excellent thermal stability, high compression strength and plastic deformation find application as high temperature shape memory alloys (HTSMA) in many engineering devices used in aerospace and automotive engines [29, 44, 141] .

Several applications of the magnetic shape memory materials have been proposed in literature which employ magnetic field as driving force. Applications such as actuators, couplers, fluidics, positioning devices, vibrators, sensors and generators can be implemented with MSM material [138, 140]. The MSM actuator can also be used in a proportional valve to control airflow. In valve application the

fast response (< 4 ms) of the MSM actuator is utilized. Benefits of the MSM actuators have been fast motion, high operating frequencies, high strains and large damping ability. Another application is in MSM pumps which use both directions of the motion of the MSM material. In sensor applications, magnetic permeability of the material can be used as function of strain, stress or field. In the actuator applications, the ability of the MSM element can be used to generate force and displacement controlled by driving magnetic field. However, in order to realize MSM applications for the alloys of Ni-Mn-Ga, further research directed towards enhancing compression strength and reducing brittleness of these materials in polycrystalline products is required.

1.10 Objectives and scope of the present work

The structural and magnetic properties are very sensitive to the composition of the alloy. Such an effect has been seen in the off-stoichiometric alloys $Ni_{50}Mn_{25+x}Ga_{25-x}$, $Ni_{2+x}Mn_{1-x}Ga$ and $Ni_{50+x}Mn_{25}Ga_{25-x}$ [44, 47, 50]. Coupled magnetostructural transformations (with $T_M \sim T_C$) have been reported for $Ni_{2+x}Mn_{1-x}Ga$ (x = 0.18-0.28) alloys [14], which crystallize in non-modulated tetragonal structure. Considerable magnetocaloric effect has been seen in these alloys. In this system, T_M is found to increase systematically from 202 K for x = 0 to 330 K for x = 0.28 with an increase in the electron per atom (e/a) ratio. Alloys with x > 0.28 exhibit T_M above T_C, and they often crystallize in non-modulated tetragonal structure. There are numerous reports on the properties of off-stoichiometric Ni-Mn-Ga alloys of different compositions in literature. However, since the physical properties depend not only on the composition but also on the atomic order, the processing conditions play an important role. As a result, correlation between various properties can be drawn only from a series of alloys processed under similar conditions.

The $Ni_{53.1}Mn_{26.6}Ga_{20.3}$ alloy [29] is reported in literature to exhibit T_M close to T_C. It crystallizes in non-modulated structure and is proposed for high temperature shape memory application. We have chosen a close by composition

$Ni_{53.5}Mn_{26.0}Ga_{20.5}$ for detailed study in the present work. This alloy is rich in Ni compared to the stoichiometric Ni_2MnGa and shows lattice modulation in martensitic state at room temperature (RT). It exhibits a coupled magnetostructural transformation at around 347 – 351 K. In the present work detailed investigations are carried out on this alloy with regard to its structural, microstructural, magnetic and mechanical properties.

In order to tune the martensitic transformation temperatures to the desired values to suit applications at RT, doping other elements into the parent compound have been attempted. The effects of substitution of elements like cobalt [82, 83, 85, 87, 90, 141], iron [85, 91-93, 95, 97], rare-earths [100-107] and boron [108, 109] in Ni-Mn-Ga system have been reported by many groups. Most of the reports are focused on the effect of the dopant on structural and magnetic transformation temperatures. It is interesting to note that T_M and T_C are strongly influenced, not only by magnetic dopants like Co and Fe but also by a non-magnetic dopant such as boron.

It is well known that the Ni-Mn-Ga alloys are brittle limiting their applications as actuators to a few mechanical cycles. Introduction of boron is known to influence the microstructural and mechanical properties of intermetallic compounds. In Ni_3Al [122, 125, 143], addition of boron refines the grains and improves ductility. Boron is reported to segregate at the grain boundaries and modify the mechanical properties of Ni_3Al. In the case of Ti-Pd-Ni [123], 0.2 at.% boron addition increases ductility by reducing grain size, without affecting the shape memory effect. In the recent past, investigations on the structural and magnetic properties of $Ni_2Mn_{1-x}GaB_x$, $Ni_2MnGa_{1-x}B_x$ [108, 109], $Ni_{50}Mn_{36.5}Sb_{13.5-x}B_x$ [110] and $Ni_{43}Mn_{46}Sn_{11}B_x$ [111] systems have been reported. Except in the first system where boron is substituted for Mn, the martensitic transformation temperature is reported to increase with B doping in all other systems. The alloys of the first two systems of Ni-Mn-Ga studied are all in the austenitic phase at RT and hence are not suitable for applications at RT. There are no reports on the effect of B on the mechanical properties of the above systems.

In literature, there are no systematic investigations on the effect of boron on the superstructural ordering, the microstructural and mechanical properties of Ni-Mn-Ga alloys. The work presented in this thesis addresses this problem through a systematic investigation of the effect of boron addition on the properties of the parent alloy $Ni_{53.5}Mn_{26.0}Ga_{20.5}$.

We then focused on the linear correlation of T_M with e/a, as reported in literature on off-stoichiometric Ni-Mn-Z (Z = Ga, Sb, Sn and In) alloys [45, 48, 50, 65, 99] and Ni-Mn-Al [144, 145] alloys. This provides a guide to predict the variations in T_M, on substitution of another element in Ni-Mn-Ga alloys. However, several groups reported anomalies in the correlation of T_M with e/a in the case of quasi-ternary systems like Ni-Mn-Ga-Al [119], Ni-Mn-Ga-In [118] and Ni-Mn-Ga-Fe [85, 91, 93]. We propose in this work, a new scheme of counting electron / atom ratio to resolve the anomaly and thus contribute to prediction of T_M for alloy design.

1.11 Organization of the thesis

The **first** chapter presents a brief introduction to the area of active materials, in general, and thermal shape memory and magnetic shape memory alloys, in particular. Initially, the reported work on the physical properties of Ni-Mn-Ga alloys and their dependence on composition are reviewed. Effect of doping non-magnetic light elements like boron and magnetic elements like Fe and Co in Ni-Mn-Ga alloys, on the phase transformation temperatures, crystal structure and magnetic properties, as gathered from various reports in literature, are discussed. There are very few reports relating the mechanical properties to microstructural features in off-stoichiometric and quasi-ternary alloys derived from Ni-Mn-Ga system, which are summarized. The present work aims at systematic investigations on $Ni_{53.5}Mn_{26.0}Ga_{20.5}B_x$ (x = 0, 0.5 and 1).

The **second** chapter describes the method followed for the preparation of the Ni-rich $Ni_{53.5}Mn_{26.0}Ga_{20.5}$ alloy (the parent compound) and the alloys with boron addition, viz. $Ni_{53.5}Mn_{26.0}Ga_{20.5}B_x$ (x = 0, 0.5 and 1) alloys. The optimized

processing conditions involving induction melting, quenching and the subsequent heat treatments for homogenization are discussed. This chapter also discusses the basic principles involved in various techniques used to characterize different properties like structural, microstructural, magnetic and shape memory of the samples.

The **third** chapter deals with investigations of the Ni-rich $Ni_{53.5}Mn_{56.0}Ga_{20.5}$ alloy. Transformation temperatures and the crystal structure are determined. The microstructural properties are correlated to the mechanical properties. This alloy is found to exhibit shape memory as well as magneto-caloric effects.

The **fourth** chapter describes the influence of boron addition on the structural and microstructural properties of $Ni_{53.5}Mn_{26.0}Ga_{20.5}B_x$ (x = 0, 0.5 and 1.0) alloys. Effect of boron on lattice modulation and the grain size are studied. Compositional analysis of second phase segregation at the grain boundaries and the matrix are determined from detailed FESEM studies.

The **fifth** chapter describes the effect of boron on the mechanical and magnetic properties of the above $Ni_{53.5}Mn_{26.0}Ga_{20.5}B_x$ alloys. Mechanical properties like compression strength and shape memory properties were studied using compressive stress-strain measurements. A detailed microstructural study at higher magnification carried out using FESEM show that the above results are correlated to the presence of precipitates of a secondary phase at the grain boundaries. The observed results on alterations in shape memory properties and the low temperature saturation magnetization on boron addition are explained in terms of second phase segregation and the compositional shift of the matrix.

In **sixth** chapter, we examine the general trend that T_M varies linearly with *e/a* ratio for off-stoichiometric Ni-Mn-Ga /Al alloys, while anomaly is observed for Ni-Mn-Ga-Fe. A modified scheme is proposed for computing effective electron / atom ratio by counting only the non-bonding electrons instead of all the electrons outside the rare gas shell, which resolves the anomaly in Fe doped alloys. This method also enables prediction of T_M in iso-electronic substitutions like in Ni-Mn-Ga-Al and Ni-Mn-Ga-In alloys.

Seventh chapter presents a summary of the work done. Various conclusions that can be drawn from the present investigations are discussed.

References

[1] M.J. Dapino, *Encyclopedia of Smart Materials.* John Wiley and Sons, Inc., New York, NY, 2000.

[2] G.B. Kauffman and I. Mayo, *The Chemical Educator* **2** (1997)1-21.

[3] K. Otsuka and C.M. Wayman, *Shape memory materials*, Cambridge University Press (1998).

[4] C.M. Wayman, *Phase transformations, Nondiffusive* (Chapter 15), *Physical Metallurgy*, Third edition, Elsevier Publishers (1983).

[5] T. Saburi, S. Nenno and C.M. Wayman, *Proc. ICOMAT-79* (1979) 619.

[6] A. Sozinov, A.A. Likhachev, N. Lanska and K. Ullakko, *Appl. Phys. Lett.* **80** (2002) 1746.

[7] R.N. Couch and I. Chopra, *Proceedings of SPIE* **5053** (2003) 169.

[8] P. Henry, D. Bono, J. Feuchtwanger, S.M. Allen and R.C. O'Handley, *J. Appl. Phys.* **91** (2002) 7810.

[9] K. Ullakko, J. K. Huang, C. Kantner, R.C. O'Handley and V.V. Kokorin, *Appl. Phys. Lett.* **69** (1996) 1966.

[10] S.J. Murray, M.A. Marioni, A.M. Kukla, J. Robinson, R.C. O'Handley and S.M. Allen, *J. Appl. Phys.* **87** (2000) 5774.

[11] A.N. Vasil'ev, A.D. Bozhko, V.V. Khovailo, I.E. Dikshtein, V.G. Shavrov V.D. Buchelnikov, M. Matsumoto, S. Suzuki, T. Takagi and J. Tani, *Phys. Rev. B* **59** (1999) 1113.

[12] R.D. James, R. Tickle and M. Wuttig, *Mater. Sci. Eng. A* **273-275** (1999) 320.

[13] M. Wuttig, J. Li and C. Craciunescu, *Scripta Mater.* **44** (2001) 2393.

[14] H. Morito, A. Fujita, K. Fukamichi, R. Kainuma, K. Ishida and K. Oikawa, *Appl. Phys. Lett.* **81** (2002) 1657.

[15] K. Oikawa, L. Wulff, T. Iijima, G. Gejima, T. Ohmori, A. Fujita, K. Fukamichi, R. Kainuma and K. Ishida, *Appl. Phys. Lett.* **79** (2001) 3290.

[16] Y. Murakami, D. Shindo, K. Oikawa, R. Kainuma and K. Ishida, *Appl. Phys. Lett.* **82** (2003) 3695.

[17] K. Oikawa, T. Ota, T. Ohmori, Y. Tanaka, H. Morito, A. Fujita, R. Kainuma, K. Fukamichi and K. Ishida, *Appl. Phys. Lett.* **81** (2002) 5201.

[18] A. Fujita, K. Fukamichi, F. Gejima, R. Kainuma and K. Ishida, *Appl. Phys. Lett.* **77** (2000) 3054.

[19] R.D. James and M. Wuttig, *Phil. Mag. A* **77** (1998) 1273.

[20] T. Kubota, T. Okazaki, Y. Furuya and T. Watanabe, *J. Mag. Mag. Mater.* **239** (2002) 551.

[21] Y. Liang, T. Wada, H. Kato, T. Tagawa, M. Taya and T. Mori, *Mater. Sci. Eng. A* **338** (2002) 89.

[22] T. Takashita, T. Takeuchi, T. Fukuda, M. Tsujiguchi, T. Saburi, R. Oshima and S. Muto, *Appl. Phys. Lett.* **77** (2000) 1502.

[23] V.V. Kokorin, Thesis for Doctorate of Physico-Mathematical Sciences (Kiev, 1978).

[24] T. Kakeshita, K. Shimizu, T. Maki, I. Tamura, S. Kijima and M. Date. *Scripta Metall.*, **19** (1985) 973.

[25] P.J. Webster, K.R.A. Ziebeck, S.L. Town and M.S. Peak, *Phil. Mag. B* **49** (1984) 295.

[26] B. Wedel, M. Suzuki, Y. Murakami, C. Wedel, T. Suzuki, D. Shindo, K. Itagaki, *J. Alloys Compd.* **290** (1999) 137.

[27] W.H. Wang, G.H. Wu, J.L. Chen, C.H. Yu, S.X. Gao, W.S. Zhan, Z. Wang, Z.Y. Gao, Y. F. Zheng and L.C. Zhao, *Appl. Phys. Lett.* **77** (2000) 3245.

[28] W.H. Wang, Z.H. Liu, Z.W. Shan, J.L. Chen, G.H. Wu and W.S. Zhan, *J. Phys. D: Appl. Phys.* **35** (2002) 492.

[29] V.A. Chernenko, V. L'vov, J. Pons and E. Cesari, *J. Appl. Phys.* **93** (2003) 2394.

[30] R. Tickle, R.D. James, T. Shield, M. Wuttig and V. V. Kokorin, *IEEE Trans. Magn.* **35** (1999) 4301.

[31] Q. Pan and R.D. James, *J. Appl. Phys.* **87** (2000) 4702.

[32] Y.W. Lai, N. Scheerbaum, D. Hinz, O. Gutfleisch, R. Schäfer, L. Schultz and J. McCord, *Appl. Phys. Lett.* **90** (2007) 192504.

[33] R.C. O'Handley, *Modern Magnetic Materials: Principles and Applications* (New York: Wiley) (2000).

[34] P. Müllner, *Zeitschrift fur Metallkunde* **97** (2006) 205.

[35] P. Müllner, V.A. Chernenko and G. Kostorz, *J. Mag. Mag. Mater.* **267** (2003) 325.

[36] P. Müllner, V.A. Chernenko and G. Kostorz, *Scripta Mater.* **49** (2003) 129.

[37] P. Müllner, V.A. Chernenko and G. Kostorz, *Mater. Sci. Eng. A* **387-389** (2004) 965.

[38] N. Okamoto, T. Fukuda and T. Kakeshita, *Mater. Sci. Eng.* A **481-482** (2008) 306.

[39] O. Heczko, *J. Magn. Magn. Mater.* **290-291** (2005) 787.

[40] T. Kakeshita, T. Fukuda and T. Kakeuchi, *Mater. Sci. Eng.* A **438–440** (2006) 12.

[41] K. Ullakko, J.K. Huang, V.V. Kokorin and R.C. O'Handley, *Scripta. Mater.* **36** (1997) 1133.

[42] A.A. Cherechukin, I.E. Dikshtein, D.I. Ermakov, A.V. Glebov, V.V. Koledov, D.A. Kosolapov, V.G. Shavrov, A. A. Tulaikova, E.P. Krasnoperov and T. Takagi, *Phys. Lett.* A **291** (2001)175.

[43] X. Zhou, W. Li, H.P. Kunkel, G. Williams, *J. Magn. Magn. Mater.* **293** (2005) 854.

[44] Y. Ma, C. Jiang, Y. Li, H. Xu, C. Wang and X. Liu, *Acta Mater.* **55** (2007) 1533.

[45] A. Planes, L. Mañosa and M. Acet, *J. Phys. Condens. Matter* **21** (2009) 233201.

[46] R.E. Watson and M. Weinert, *Solid State Physics* (Academic Press, New York, 2001), Vol. 56, p. 1.

[47] C. Jiang, Y. Muhammad, L. Deng, W. Wu, and H. Xu, *Acta Mater.* **52**, 2779 (2004).

[48] N. Lanska, O. Söderberg, A. Sozinov, Y. Ge, K. Ullakko, and V.K. Lindroos, *J. Appl. Phys.* **95** (2004) 8074.

[49] A.N. Vasil'ev, A.R. Keiper, V.V. Kokorin, V.A. Chernenko, T. Takagi, and J. Tani, *Int. J. Appl. Electromag. Mater.* **5** (1994) 163.

[50] V.V. Khovaylo, V.D. Buchelnikov, R. Kainuma, V.V. Koledov, M. Ohtsuka, V.G. Shavrov, T. Takagi, S.V. Taskaev, and A.N. Vasiliev, *Phys. Rev. B* **72** (2005) 224408.

[51] C. Jiang , G. Feng, S. Gong and H. Xu, *Mater. Sci. Eng. A* **342** (2003) 231.

[52] R.W. Overholser, M. Wuttig and D.A. Neumann, *Scripta Mater.* **40** (1999) 1095.

[53] V.V. Khovailo, T. Takagi, A.N. Vasilev, H. Miki, M. Matsumoto and R. Kainuma, *Phys. Status Solidi A* **183** (2001) R1.

[54] V.V. Martynov, *J. Phys. IV* (Paris) **5** (1995) C8-91.

[55] V.A. Chernenko, C. Seguí, E. Cesari, J. Pons and V.V. Kokorin, *Phys. Rev. B* **57** (1998) 2659.

[56] J. Pons, V.A. Chernenko, R. Santamarta and E. Césari, *Acta Mater.* **48** (2000) 3027.

[57] A.A. Likhachev, A. Sozinov and K. Ullakko, *IEEE Trans. Magn.* **38** (2002) 2814.

[58] V.V. Martynov and V.V. Kokorin *, J. de Phys. III* **2** (1992) 739.

[59] G. Fritsch, V.V. Kokorin, V.A. Chernenko, A. Kempf and I.K. Zasimchuk, *Phase Transitions* **57** (1996) 233.

[60] Y. Ge, O. Söderberg, N. Lanska, A. Sozinov, K. Ullakko and V.K. Lindroos, *J. de Phys. IV* **112** (2003) 921.

[61] N. Glavatska, G. Mogilniy, I. Glavatsky, S. Danilkin, D. Hohlwein, A. Beskrovnij, O. Söderberg and V.K. Lindroos, *J. de Phys. IV* **112** (2003) 963.

[62] A. Sozinov, A.A. Likhachev, N. Lanska, K. Ullakko and V.K. Lindroos, *Proc. SPIE*, **4699** (2002) 195.

[63] N. Lanska and K. Ullakko, *J. de Phys. IV* **112** (2003) 925.

[64] V.A. Chernenko, V.V. Kokorin and I.N. Vitenko, *Scripta Mett. Mater.* **33** (1995) 1239.

[65] V.A. Chernenko, *Scripta Mater.* **40** (1999) 523.

[66] S.K. Wu and S.T. Yang, *Mater. Lett.* **57** (2003) 4291.

[67] U. Gaitzsch, S. Roth, B. Rellinghaus and L. Schultz, *J. Mag. Mag. Mater.* **305** (2006) 275.

[68] U. Gaitzsch, M. Pötschke, S. Roth, N. Mattern, B. Rellinghaus and L. Schultz, *J. Alloys Compd.* **443** (2007) 99.

[69] M. Richard, J. Feuchtwanger, D. Schlagel, T. Lograsso, S.M. Allen and R.C. O'Handley, *Scripta Mater.* **54** (2006) 1797.

[70] V.V. Khovailo, V. Novosad, T. Takagi, D.A. Filippov, R.Z. Levitin and A.N. Vasil'ev, *Phys. Rev. B* **70** (2004) 174413.

[71] A. Satish Kumar, M. Ramudu and V. Seshubai, *Phys. Status Solidi B*, (2011) 1–7.

[72] M.L. Richard, J. Feuchtwanger, S.M. Allen, R.C. O'Handley, P. Lázpita, J.M. Barandiaran, J. Gutierrez, B. Ouladdiaf, C. Mondelli, T. Lograsso and D. Schlagel, *Phil. Mag.* **87** (2007) 3437.

[73] P. Lázpita, J.M. Barandiarán, J. Gutiérrez, J. Feuchtwanger,V.A. Chernenko and M.L. Richard, *New J. Phys.* **13** (2011) 033039.

[74] C. Jie, L.I. Yan, S. Jia-Xiang and X.U. Hui-Bin, *Chin. Phys. Lett.* **26** (2009) 047101.

[75] O. Heczko, A. Sozinov and K. Ullakko, *IEEE Trans. Magn.* **36** (2000) 3266.

[76] B.D. Shanina, A.A. Konchits, S.P. Kolesnik, V.G. Gavriljuk, I.N. Glavatskij, Ni.I. Glavatska, O. Söderberg, V.K. Lindroos and J. Foct, *J. Mag. Mag. Mater.* **237** (2001) 309.

[77] A.H. Morrish, *The Physical Principles of Magnetism,* Wiley, New York, (Chapter 3) (1965).

[78] V.K. Pecharsky and K.A. Gschneidner Jr., *J. Mag. Mag. Mater.* **200** (1999) 44.

[79] L. Pareti, M. Solzi, F. Albertini and A. Paoluzi, *Eur. Phys. J.* B **32** (2003) 303.

[80] T. Krenke, E. Duman, M. Acet, E.F. Wassermann, X. Moya, L. Mañosa and A. Planes, *Nat. Mater.* **4** (2005)450.

[81] A.A. Cherechukin, T. Takagi, H. Miki, M. Matsumoto and M. Ohtsuka, *J. Appl. Phys.* **95** (2004) 1740.

[82] X.Q. Chen, X. Lu, D.Y. Wang and Z.X. Qin, *Smart Mater. Struct.* **17** (2008) 065030.

[83] D.Y. Cong, S. Wang, Y.D. Wang, Y. Ren, L. Zuo and C. Esling, *Mater. Sci. Eng. A* **473** (2008) 213.

[84] M. Khan, I. Dubenko, S. Stadler and N. Ali, *J. Appl. Phys.* **97** (2005)10M304.

[85] D.E. Soto-Parra, X. Moya, L. Mañosa, A. Planes, H. Flores-Zúñiga, F. Alvarado-Hernández, R.A. Ochoa-Gamboa, J.A. Matutes-Aquino and D. Ríos-Jara, *Phil. Mag.* **90** (2010) 2771.

[86] S. Fabbrici, J. Kamarad, Z. Arnold, F. Casoli, A. Paoluzi, F. Bolzoni, R. Cabassi, M. Solzi, G. Porcari, C. Pernechele and F. Albertini, *Acta Mater.* **59** (2011) 412.

[87] V. Sánchez-Alarcos, J.I. Pérez-Landazábal, V. Recarte, C. Gómez-Polo and J. A. Rodríguez-Velamazán, *Acta Mater.* **56** (2008) 5370.

[88] I. Glavatskyy, N. Glavatska, O. Söderberg, S. P. Hannula and J. U. Hoffmann, *Scripta Mater.* **54** (2006) 1891.

[89] V.V. Khovailo, T. Abe, V.V. Koledov, M. Matsumoto, H. Nakamura, R. Note, M. Ohtsuka, V.G. Shavrov and T. Takagi, *Mater. Trans.* **44** (2003) 2509.

[90] A. Satish Kumar, M. Ramudu and V. Seshubai, *J. Alloys Compd.* **509** (2011) 8215.

[91] Z.H. Liu, M. Zhang, W.Q. Wang, W.H. Wang, J.L. Chen, G.H. Wu, F.B. Meng, H.Y. Liu, B.D. Liu, J.P. Qu and Y.X. Li, *J. Appl. Phys.* **92** (2002) 5006.

[92] F. Chen, H.B. Wang, Y.F. Zheng, W. Cai and L.C. Zhao, *J. Mater. Sci.* **40** (2005) 219.

[93] D. Kikuchi, T. Kanomata, Y. Yamaguchi, H. Nishihara, K. Koyama and K. Watanabe, *J. Alloys Compd.* **383** (2004) 184.

[94] D. Soto, F.A. Hernandez, H.F. Zuniga, X. Moya, L. Mañosa, A. Planes, S. Aksoy, M. Acet and T. Krenke, *Phys. Rev. B* **77** (2008) 184103.

[95] D.E. Soto-Parra, F. Alvarado-Hernandez, O. Ayala, R.A. Ochoa-Gamboa, H. Flores-Zúñiga and D. Rios-Jara, *J. Alloys Compd.* **464** (2008) 288.

[96] H. Luo, F. Meng, Z. Feng, Y. Li, W. Zhu, G. Wu, X. Zhu, C. Jiang and H. Xu, *J. Appl. Phys.* **107** (2010) 013905.

[97] K. Koho, O. Söderberg, N. Lanska, Y. Ge, X. Liu, L. Straka, J. Vimpari, O. Heczko and V.K. Lindroos, *Mater. Sci. Eng. A* **378** (2004) 384.

[98] D. Kikuchi, T. Kanomata, Y. Yamaguchi, and H. Nishihara, *J. Alloys Compd.* **426** (2006) 223.

[99] X.Q. Chen, F.J. Yang, X. Lu and Z.X. Qin, *Phys. Stat. Sol. (b)* **244** (2007) 1047.

[100] K. Tsuchiya, A. Tsutsumi, H. Ohtsuka and M. Umemoto, *Mater. Sci. Eng. A* **378** (2004) 370.

[101] R. Wroblewski, M. Leonowicz, Z. Zengqi and J. Liping, *J. Mag. Mag. Mater.* **316** (2007) e595.

[102] Z.Y. Zhang, Z.W. Du, B.L. Shao, A.S. Liu and Z.M. Sun, *Mater. Characterization* **59** (2008) 1041.

[103] L. Gao, W. Cai, A.L. Liu and L.C. Zhao, *J. Alloys Compd.* **425** (2006) 314.

[104] J. Sui, X. Zhang, L. Gao and W. Cai, *J. Alloys Compd.* **509** (2011) 8692.

[105] W. Cai, L. Gao, A.L. Liu, J.H. Sui and Z.Y. Gao, *Scripta Mater.* **57** (2007) 659.

[106] L. Gao, Z.Y. Gao, W. Cai and L.C. Zhao, *Mater. Sci. Eng. A* **438-440** (2006) 1077.

[107] L. Gao, J.H. Sui, W. Cai and Z.Y. Gao, *Solid State Commn.* **149** (2009) 257.

[108] B.R. Gautam, I. Dubenko, A.K. Pathak, S. Stadler and N. Ali, *J. Mag. Mag. Mater.* **321**(2009) 29.

[109] B.R. Gautam, I. Dubenko, A.K. Pathak, S. Stadler and N. Ali, *J Phys: Condens. Matter* **20** (2008) 465209.

[110] H. Luo, F. Meng, Q. Jiang, H. Liu, E. Liu, G. Wu and Y. Wang, *Scripta Mater.* **63** (2010) 569.

[111] H.C. Xuan, D.H. Wang, C.L. Chang, Z.D. Han, B.X. Gu and Y.W. Du, *Appl. Phys. Lett.* **92** (2008) 102503.

[112] A.N. Vasil'ev, V.D. Buchel'nikov, T. Takagi, V.V. Khovaílo and É.I. Éstrin, *Physics - Uspekhi* **46** (2003) 559.

[113] V.V. Kokorin, I.A. Osipenko and T.V. Shirina, *Phys. Met. Metallography* **67** (1989) 173.

[114] C.B. Jiang, G. Feng, S.K. Gong and H.B. Xu, *Mater. Sci. Eng. A* **14** (2003) 231.

[115] V. Sánchez-Alarcos, J.I. Pérez-Landazábal, V. Recarte, J.A. Rodriguez-Velamazán and V.A. Chernenko, *J. Phys. Condens. Matter.* **22** (2010) 166001.

[116] J. Font, J. Muntasell, R. Santamarta, J. Pons, E. Cesari, V. Recarte, J.I. Pérez-Landazábal, C. Gómez-Polo and J. Dutkiewicz, *Mater. Sci. Eng. A* **481–482** (2008) 262.

[117] J. X. Wu, B.H. Jiang and T.Y. Hsu, *Acta Metall. Sinica* **2** (1989) 326.

[118] M. Khan, I. Dubenko, S. Stadler, and N. Ali, *J. Phys.: Condens. Matter.* **16** (2004) 5259.

[119] Y. Xin, Y. Li, C. Jiang and H. Xu, *Mater. Sci. Forum* **475-479** (2005) 1991.

[120] K. Ullakko, Y. Ezer, A. Sozinov, G. Kimmel, P. Yakovenko and V.K. Lindroos, *Scripta Mater.* **44** (2001) 475.

[121] M. Ramudu, A. Satish Kumar, V. Seshubai, K. Muraleedharan, K. S. Prasad and T. Rajaekharan, *Scripta Mater.* **63** (2010) 1073.

[122] L. Hui, L. Xiang, G. Jianting and H.U. Zhuangqi, *Acta Metall. Sinica* **2** (1989) 256.

[123] Y. Suzuki, Y. Xu, S. Morito, K. Otsuka and K. Mitose, *Mater. Lett.* **36** (1998) 85.

[124] I. Sen, S. Tamirisakandala, D.B. Miracle and U. Ramamurthy, *Acta Mater.* **55** (2007) 4983.

[125] S. Ghosh Chowdhury, *Phil. Mag. Lett.* **74** (1996) 327.

[126] W. Soboyejo, *Mechanical properties of engineered materials*, Marcel Dekker, New York (2002).

[127] X.W. Liu, O. Söderberg, K. Koho, N. Lanska, Y. Ge, A. Sozinov and V.K. Lindroos, *Wear* **258** (2005) 1364.

[128] H.B. Wang, F. Chen, Z.Y. Gao, W. Cai and L.C. Zhao, *Mater. Sci. Eng. A* **438–440** (2006) 990.

[129] O. Söderberg, Doctoral Thesis TKK-ME-DT-2 (2004).

[130] A. Sozinov, A.A. Likhachev, N. Lanska, O. Söderberg, K. Ullakko and V.K. Lindroos, *Proc. SPIE* **5053** (2003) 586.

[131] A. Sozinov, A.A. Likhachev, N. Lanska, O. Söderberg, K. Ullakko and V.K. Lindroos, *Mater. Sci. Eng. A* **378** (2004) 399.

[132] A. Sozinov, A.A. Likhachev, N. Lanska, O. Söderberg, K. Koho, K. Ullakko and V.K. Lindroos, *J. de Phys. IV* **115** (2004) 121.

[133] H. Xu, Y. Ma and C. Jiang, *Appl. Phys. Lett.* **82** (2003) 3206.

[134] A. Sozinov, A.A. Likhachev and K. Ullakko, *Proc. SPIE.* **4333** (2001) 189.

[135] L.M. Cheng, Ph. D. Thesis (2004).

[136] U. Gaitzsch, M. potschke, S. Roth, B. Rellinghaus and L. Schultz, *Scripta Mater.* **57** (2009) 365.

[137] U. Gaitzsch, M. potschke, S. Roth, B. Rellinghaus and L. Schultz, *Scripta Mater.* **57** (2007) 493.

[138] J. Tellinen, I. Suorsa, A. Jääskeläinen, I.Aaltio, K. Ullakko, *Actuator 2002* (2002)

[139] *Advances in shape memory materials*, edited by V.A. Chernenko, Trans Tech Publications (2008).

[140] I. Aaltio and K. Ullakko, *Actuator 2000* (2000) 527.

[141] Y. Ma, S. Yang, Y. Liu and X. Liu, *Acta Mater.* **57** (2009) 3232.

[142] I. Suorsa, J. Tellinen, E. Pagounis, I. Aaltio and K. Ullakko, *Proc. Actuator 2002* (2002) 158.

[143] N. Masahashi, *Mater. Sci. Eng. A* **223** (1997) 42.

[144] R. Kainuma, H. Nakano and K. Ishida, *Metall. Mater. Trans.* **27A** (1996) 4153.

[145] R. kainuma, W. Ito, R.Y. Umetsu, K. Oikawa and K. Ishida, *Appl. Phys. Lett.* **93** (2008) 091906.

Chapter 2

EXPERIMENTAL TECHNIQUES

In the present study, following experimental techniques were used in order to characterize the samples made. A flow-chart indicating the details of sample preparation and their characterization methods employed is provided in Fig. 2.1

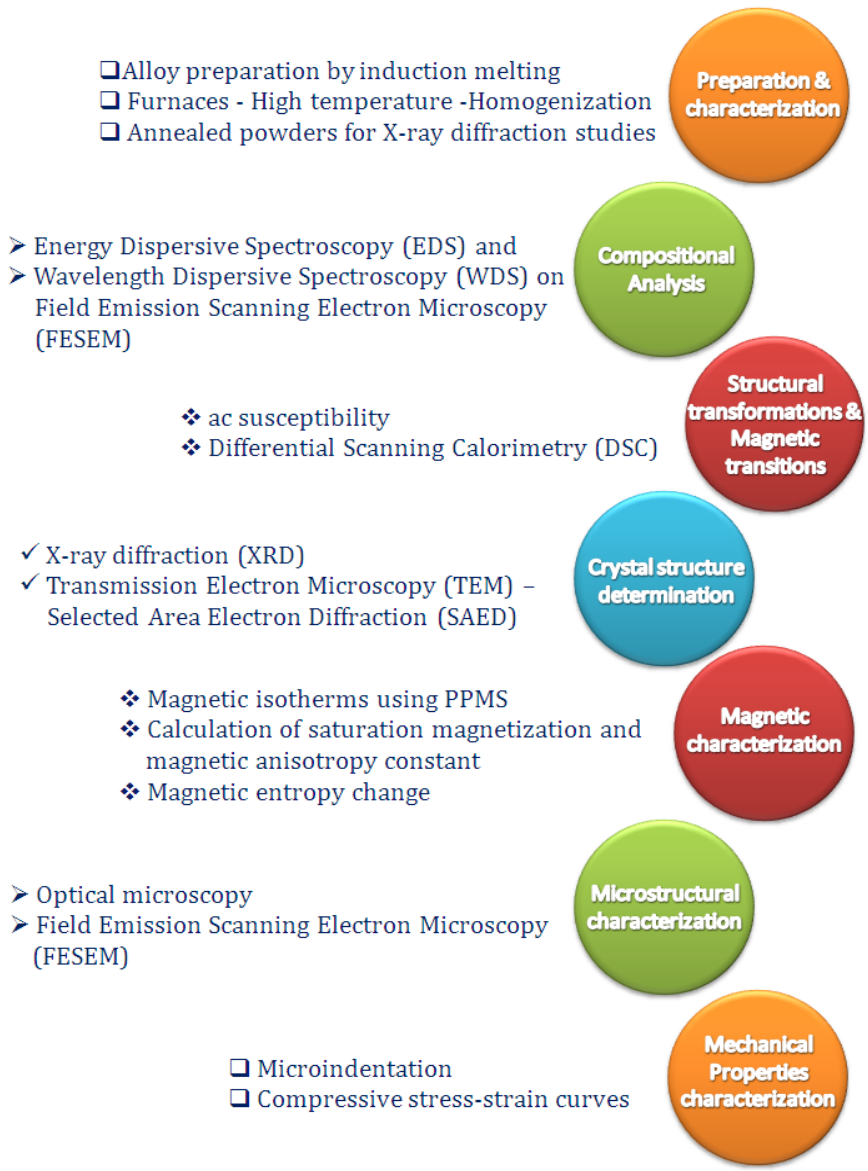

Fig. 2.1. A flow-chart indicating a list of methods employed in the present work for sample preparation and their characterization.

2.1 Preparation and characterization of Ni-Mn-Ga alloys

2.1.1 Alloy Preparation by Induction melting

When a ferromagnetic work-piece is placed in an alternating magnetic field, opposing eddy currents are induced in the work-piece causing resistive losses. The heating effect thus produced is Induction Heating [1]. The quantum of heat produced is a function of density of the electromagnetic field present around the work piece, its rate of change and time of exposure. The frequency determines the depth of penetration of the eddy currents from the outer surface of the work piece. The frequency along with the time of exposure thus defines the profile of the heated zone in the work piece.

The output of the oscillatory system is variable in frequency. The output of the alternating current source is coupled to the induction heating coil. We have used an Induction Heater (Monga Electronics make, Model IH-120) with 12 kW power output and operating at a frequency of 125 kHz which is connected with a generator and an induction coil connected to the output of the alternating current source. The induction coil is cooled with the chilled water maintained at 20-23 ^{o}C using a chiller.

Table 2.1 List of Ni-Mn-Ga alloys prepared by induction melting.

Code	Amount of Boron addition (at.%)	Starting Composition
B-0	0	$Ni_{53.5}Mn_{26.0}Ga_{20.5}$
B-0.5	0.5	$Ni_{53.5}Mn_{26.0}Ga_{20.5}B_{0.5}$
B-1.0	1.0	$Ni_{53.5}Mn_{26.0}Ga_{20.5}B_{1.0}$

The polycrystalline ingots were prepared by induction melting method by taking the constituent elements of Ni (99.999% pure), Ga (99.999% pure), Mn (99.99% pure) and B (99.99% pure) in stoichiometric proportions in quartz ampoules by sealing them under high vacuum followed by water quenching. After first melting, the obtained ingot, in each case, is again resealed in another quartz

ampoule under high vacuum for second melting. The repeated melting will help in obtaining a homogeneous composition in the ingot. A set of samples containing different amounts of boron additions were made. The details of the compositions made are provided in Table 2.1.

2.1.2 Furnaces – High temperature - Homogenization

The pictorial representation of sample preparation is shown in Fig. 2.2. The ingots obtained after double melting were then sealed in a quartz ampoule under vacuum and were annealed at 830 ^{o}C for 7 days followed by ice water quenching.

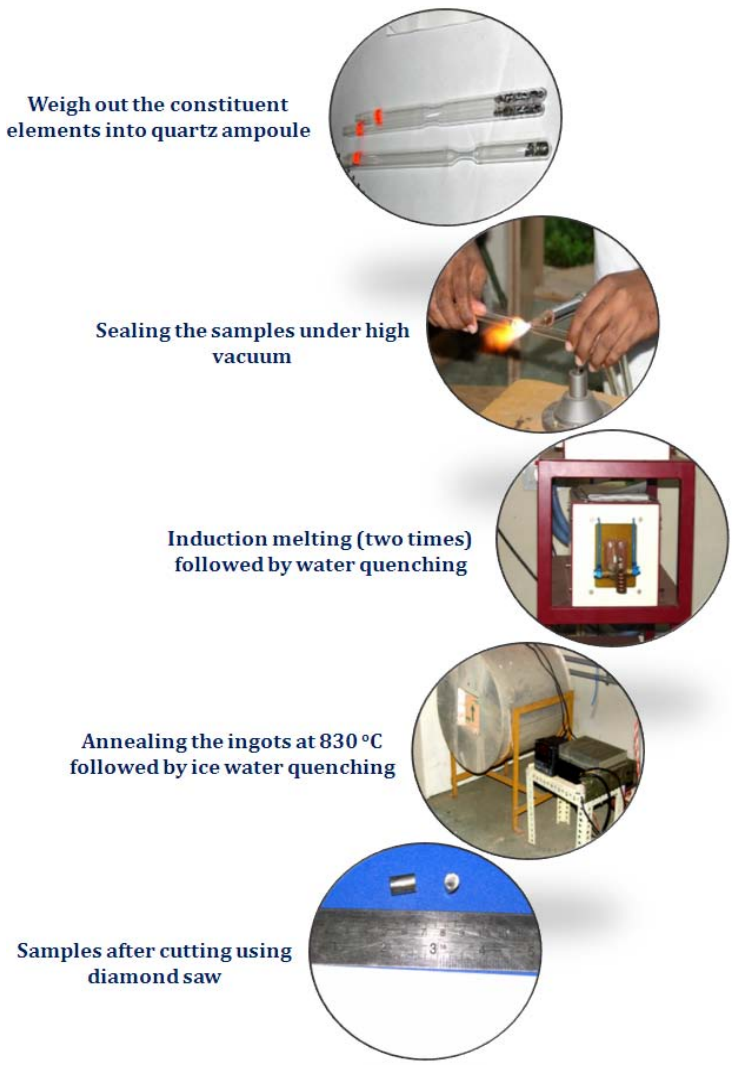

Fig. 2.2. Pictorial representation of sample preparation of Ni-Mn-Ga alloys.

The ingots obtained after annealing were sliced into sections using a low speed diamond saw, as required for various magnetic and microstructural studies.

2.1.3 Annealed powders for X-ray diffraction studies

For X-ray diffraction measurements, small portions of the samples were crushed into fine powders using an agate mortar in the presence of toluene medium. The fine powders thus obtained were vacuum sealed under argon atmosphere and were annealed at 500 ^{o}C for 12 hours to release the stresses developed in the sample during the crushing process. These were then furnace cooled to room temperature.

2.2 Compositional analysis

A Scanning Electron Microscope (SEM) employs a high energy (in keV) electron beam and helps in imaging the topography of the sample surface by operating in a raster scanning mode. In the case of a Field Emission Scanning Electron Microscope (FESEM), a field emission cathode in the electron gun of a SEM provides narrower probing beams at low as well as high electron energy, resulting in both improved spatial resolution and minimized sample charging and damage.

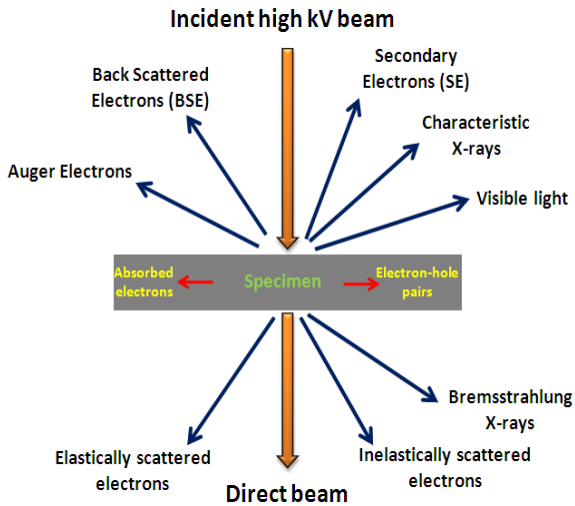

Fig. 2.3. Schematic of generation of various effects that are used to probe the sample properties using SEM technique.

When the electrons interact with the atoms of the sample, produce secondary electrons, back-scattered electrons, transmitted electrons, characteristic X-rays etc. A typical schematic sketch representing the above mentioned process is shown in Fig. 2.3. Compositional analysis in the present samples was carried out using Field Emission Scanning Electron Microscope facility equipped with Energy Dispersive Spectroscopy (EDS) as well as Wavelength Dispersive Spectroscopy (WDS) attachments.

2.2.1 Energy Dispersive Spectroscopy (EDS)

Energy Dispersive X-ray Spectroscopy is relatively a simple yet powerful technique used to identify the elemental composition in a material. The equipment is attached to the FESEM which provides the elemental information to be gathered about the specimen under investigation.

EDS works by detecting X-rays that are produced by a sample placed in an electron beam. The electron beam excites the atoms in the sample that subsequently produce X-rays to discharge the excess energy. The energy of the X-rays is characteristic of the atoms that produced them, forming peaks in the spectrum. Typical EDS attachment with FESEM is shown in Fig. 2.4.

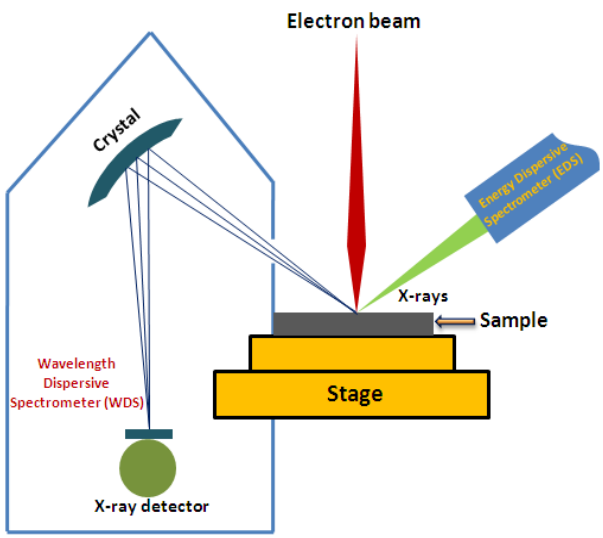

Fig. 2.4. Schematic representation of EDS and WDS attachments employed in FESEM.

As the electron beam can be precisely controlled, EDS spectra can be collected from a specific point/particle on the sample, giving an analysis of a few cubic microns of material. Alternatively, the beam can sweep over a selected area of the sample to identify the elements in that region. In addition, line profiles and X-ray maps can be acquired which depict the elemental distribution across the specimen. In the present work, the compositional studies were carried out using FESEM of Zeiss make ULTRA 55 model with EDS attachment. Electron beam of 20 keV has been employed in order to determine composition of the alloys.

2.2.2 Wavelength Dispersive Spectroscopy (WDS)

Wavelength Dispersive Spectroscopy (WDS) identifies the elemental composition of materials imaged in the SEM with an order of magnitude better spectral resolution and sensitivity compared to EDS [2]. WDS, hence is very useful in determining concentrations of light elements (atomic number < 5) which is quite complex in EDS. Most elements are detected below 0.1% and some as low as a few ppm. When an electron beam of sufficient energy interacts with a sample target it generates X-rays, as well as derivative electrons (e.g. secondary, back-scattered, auger). A wavelength-dispersive spectrometer uses the characteristic X-rays generated by individual elements to enable quantitative analyses (down to trace element levels) to be measured at spot sizes as small as a few micrometers. Typical WDS attachment with FESEM is shown in Fig. 2.4. WDS can also be used to create elemental X-ray compositional maps over a broader area by means of rastering the beam. This technique is complementary to energy-dispersive spectroscopy (EDS) in that WDS spectrometers have significantly higher spectral resolution.

We could determine the concentrations of Ni, Mn and Ga in our samples using EDS to an accuracy of ± 0.2 at.%. Boron, which is a light element, cannot be detected in EDS scan. Hence we attempted to detect boron using WDS facility with

higher resolution, but we were not fruitful, probably due to very small amounts of it being present in our alloys.

2.3. Structural transformations and magnetic transitions

In order to determine the structural phase transformation temperatures (M_s, M_f, A_s and A_f) and magnetic transition temperature (T_C), techniques like temperature dependence of ac susceptibility and Differential Scanning Calorimetry (DSC) were employed.

2.3.1. ac susceptibility

A block diagram for measuring low field ac susceptibility as a function of temperature of a given sample is shown in Fig.2.5.

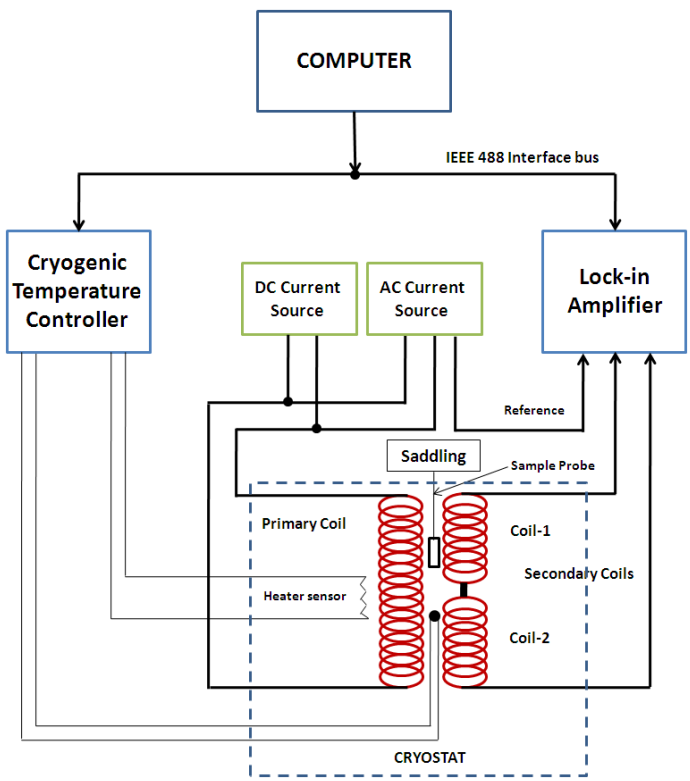

Fig. 2.5. Block diagram of mutual inductance assembly used to measure ac susceptibility.

In ac magnetic measurements, a small ac magnetic field (drive field) is applied causing a time-dependent moment in the sample. The field of the time dependent moment induces a current in the pickup coils, allowing the measurement without the sample motion. The detection circuitry is configured to detect only in a narrow frequency band, normally at the fundamental frequency of the ac drive field.

If the applied voltage is $H = H_o \cos \omega t$, where ω is the angular frequency ($=2\pi f$), the resulting magnetization amounts to

$$M = H_0 (\chi' \cos \omega t + \chi'' \sin \omega t) \quad \text{---------- (2.1)}$$

where χ' and χ'' represents the real and imaginary components of the fundamental ac susceptibility.

The fundamental principle on which this measurement works is based on the mutual induction (Faraday's law)

$$\nabla \times \boldsymbol{E} = -\frac{\partial \boldsymbol{B}}{\partial t} \quad \text{---------- (2.2)}$$

Basically the assembly comprises a mutual inductance coil assembly with two secondary coils co-axially mounted in a primary solenoid. The two secondary coils are identical and are connected in opposition in order to cancel the voltages induced by the ac field itself. A constant current source is employed to drive an ac current in the primary solenoid. The field produced by a current with root mean square (r.m.s.) value 'I_{rms}' in a solenoid is given by

$$H_{rms} = \left(\frac{\mu_0 N_p}{L_p}\right) I_{rms} \quad \text{---------- (2.3)}$$

where N_p is the number of turns in the primary coil, L_p is the length of the primary coil (in m) and I_{rms} is the r.m.s. value of the ac current through the primary coil. The field amplitude H_{ac} in Oe is $\sqrt{2}\, H_{rms}$.

When the induced voltages in the secondaries is sensed at the input of the dual phase lock-in amplifier, it gives out a signal in the form of dc voltages (V' and V'') which are proportional to the real and imaginary parts of M that are in in-phase and out-of phase, respectively, with respect to the reference signal which is in-phase with the applied field *H*.

The real and imaginary components of the ac susceptibility χ' and χ'' are proportional to the measured V' and V''. Detailed description of this technique can be found elsewhere [3, 4]. Following this procedure, the temperature variations of χ' and χ'' are obtained from the measured V' and V''.

In the present study we have used a home built ac susceptibility setup which is shown in Fig. 2.6 for measuring the characteristic transformation temperatures like martensitic start (M_s), martensitic finish (M_f) obtained during cooling the sample and austenite start (A_s), austenite finish (A_f) obtained during heating the sample in the temperature range 100-400 K.

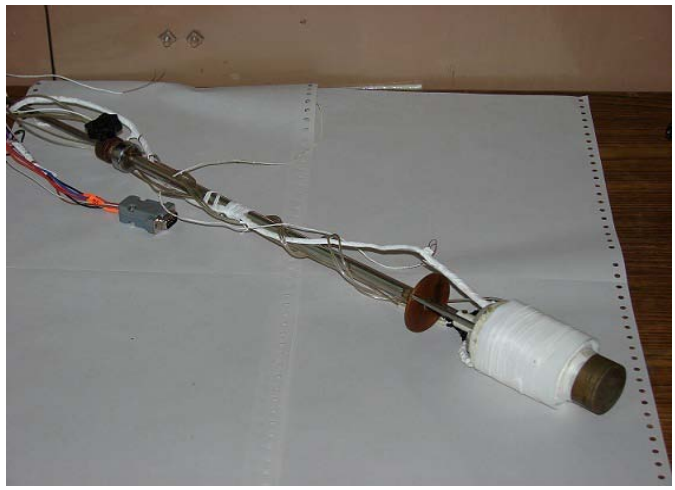

Fig. 2.6. Sample holder of the home built ac susceptibility setup.

2.3.2 Differential Scanning Calorimetry (DSC)

Differential Scanning Calorimetry (DSC) is a thermo-analytical technique in which the difference in the amount of heat required to increase the temperature of a sample puck and reference puck is measured as a function of temperature [5].

Both the sample and reference pucks are maintained at the same temperature throughout the experiment.

The basic principle underlying this technique is that when the sample undergoes a physical transformation such as phase transitions, more (or less) heat will flow to the sample puck compared to the reference puck in order to maintain both the pucks at the same temperature. Whether heat is added to the sample puck or heat is released by the sample puck depends on whether the process is exothermic or endothermic during the transformation. By observing the difference in heat flow between the sample and reference, differential scanning calorimeters are able to measure the amount of heat absorbed or released during such transitions.

In the present work, DSC (of Mettler make, Model Toledo DSC1) has been used for determination of transformation temperatures obtained during heating and cooling cycles in the temperature range 125 K to 525 K with a scan rate of 10 K/min.

2.4 Crystal structure determination

2.4.1 X-ray diffraction

When a parallel monochromatic beam of X-rays of approximately 0.1 nm wavelength strikes a crystal, the crystal acts as a three dimensional diffraction grating and produces an X-ray diffraction pattern [6]. This diffraction comprises a three dimensional array of reflections which satisfy the condition of Bragg's law

$$2d\ Sin\ \theta = n\lambda \text{ ---------- } (2.4)$$

where 'n' represents the order of diffraction, 'λ' represents the wavelength of X-rays, 'd' is the distance between a set of parallel atomic planes in the lattice and 'θ' is the angle between the incident X-ray beam and the atomic plane. The reflection angle for a particular set of lattice planes indicated by (hkl) is

$$2\theta = 2\,Sin^{-1}\left(\frac{\lambda}{2d_{hkl}}\right) \text{ ---------- (2.5)}$$

where (hkl) are Miller indices, which define the orientation of the plane with respect to the crystallographic axes. In general, the powder X-ray diffraction pattern is a set of reflections in which the lattice spacing and relative intensities are unique from each crystalline substance.

In the present work, powder X-ray diffraction patterns were recorded at room temperature using Philips X-pert X-ray diffractometer with Cu K_α radiation. The data were collected in the 2θ range of 25-100^o using a step scan, with a step size $\Delta 2\theta$ = 0.02^o and a scan rate of 10 s per step. For X-ray diffraction measurements, powders were prepared by crushing the ingot. They were sealed in quartz ampoules under high vacuum and were annealed at 500 ^{o}C for 12 h, which were then furnace cooled. X-ray diffraction patterns indicate the presence of superstructure, but the type of lattice modulation present cannot be determined precisely in Ni-Mn-Ga alloys. This is because the atomic scattering factors of Ni and Mn are very close by. For this purpose, Selected Area Electron Diffraction (SAED) patterns were obtained using Transmission Electron Microscope (TEM) facility and the lattice modulation is determined accurately.

2.4.2 Transmission Electron Microscopy (TEM)

The Transmission Electron Microscopy (TEM) is used to characterize the microstructure of materials with very high spatial resolution [7]. Information about the morphology, crystal structure and defects, crystal phases, composition and microstructure can be obtained by a combination of electron-optical imaging (2.5 Å point resolution in TECNAI) and electron diffraction.

Electrons are emitted in the electron gun by thermionic, Schottky, or field emission. The latter are used when high gun brightness and coherence are needed. A three- or four-stage condenser-lens system permits variation of the illumination

aperture and the area of the specimen illuminated. The electron intensity distribution behind the specimen is imaged with a lens system, composed of three to eight lenses, onto a fluorescent screen. The image can be recorded by direct exposure of a photographic emulsion or an image plate inside the vacuum, or digitally via a fluorescent screen coupled by a fiber-optic plate to a CCD camera. Electrons interact strongly with atoms by elastic and inelastic scattering. The specimen must therefore be very thin, typically of the order of 5−100 nm for 100 keV electrons, depending on the density and elemental composition of the object and the resolution desired.

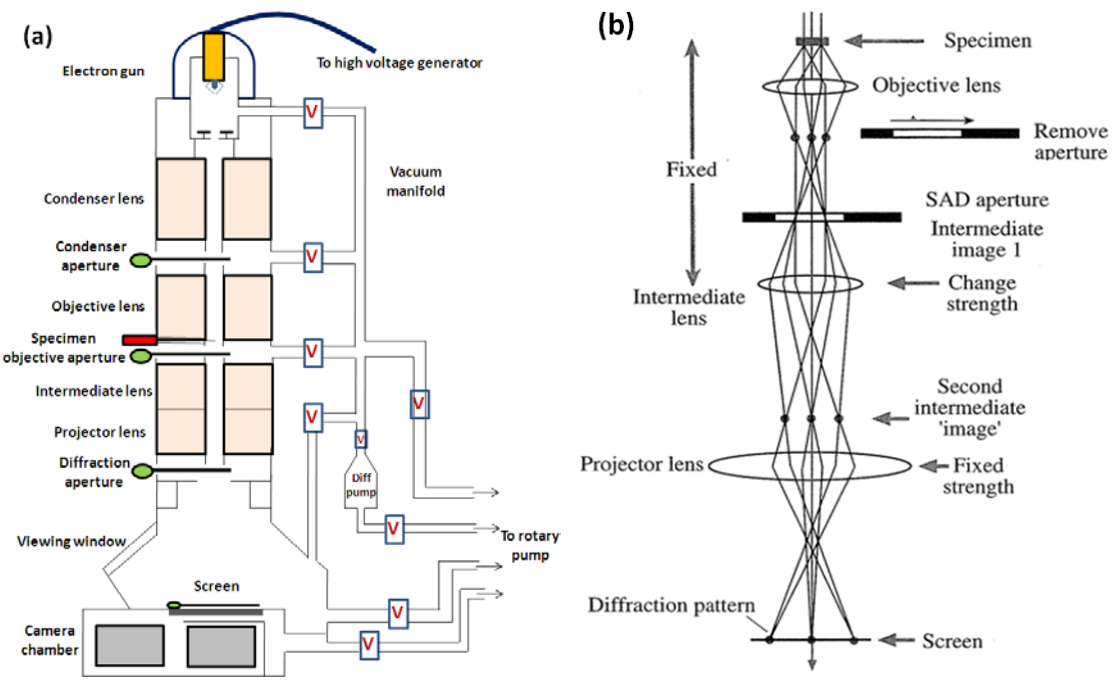

Fig. 2.7. (a) Schematic representation of TEM and (b) Ray diagram for recording the selected area electron diffraction (SAED) pattern.

Bright-field contrast is produced either by intercepting the electrons scattered through angles larger than the objective aperture (scattering contrast) or by interference between the scattered wave and the incident wave at the image point (phase contrast). Dark-field contrast is obtained by tilting the primary beam or by hollow-cone illumination so that the primary beam falls on the objective

diaphragm. In crystalline specimen, the use of the primary beam (bright field) or a Bragg-reflected beam on-axis (dark field) gives rise to diffraction contrast, which is important to image crystal defects. [7]. A schematic representation of TEM is shown in Fig. 2.7(a).

2.4.3 Selected Area Electron Diffraction (SAED)

In order to find out the crystal structure and the type of modulation, SAED patterns using TEM were carried out in the present work. If we wish to obtain a diffraction pattern with a parallel beam of electrons, the standard way is to use a selective aperture. This operation is called selected area electron diffraction, which was invented by Le Poole in 1947 [8].

Figure 2.7 (b) shows the ray diagram of this technique. A selector diaphragm of diameter d situated in the intermediate image plane (magnification $M \simeq 20 - 50$) in front of the intermediate or diffraction lens selects an area of the specimen of diameter d/M. This area can be chosen in the normal bright-field mode, in which the primary beam passes through the objective diaphragm.

2.4.4 TEM sample preparation

Initially, a thin slice of 300 μm with 3 mm dia was sectioned from the ingot using low speed diamond saw and then thinned down to a size of 80-100 μm using mechanical grinding. Further thinning to electron transparency was carried out using Precision Ion Polishing System (PIPS) in an argon atmosphere. A schematic sketch showing the method of preparing the sample for observation under TEM is shown in Fig. 2.8. SAED patterns and micrographs were recorded at RT using TECNAI G^2 TEM operated at 200 kV. The modulation present in the samples were determined by recording the SAED patterns along the [010] zone axis and observing the number of spots between the main reflections.

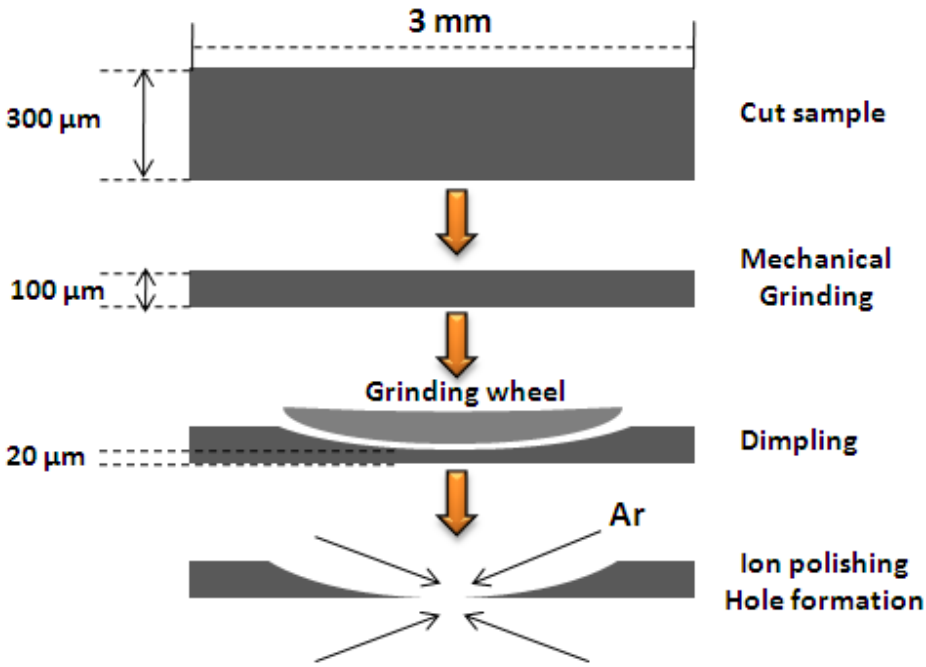

Fig. 2.8. Schematic representation of sample preparation for TEM studies.

The lattice parameters and the angle between the axes were estimated from the SAED patterns. These parameters were used in analyzing the X-ray diffractograms. Least square fitting method was used in order to determine the structure and lattice parameters of the samples under investigation accurately. Microscopic morphologies of the samples were also obtained using TEM.

2.5 Magnetic characterization

2.5.1 Magnetic Isotherms

Initial magnetization curves as a function of field (M-H) were recorded at different temperatures using Physical Property Measurement System (PPMS) with Vibrating Sample Magnetometer (VSM) attachment (Quantum Design, Model 6500). Isotherms were recorded in the temperature range of 5 – 370 K and a field range of 0-5 T. The working principle of VSM attachment in PPMS is briefly described below.

2.5.2 Physical Property Measurement System – Vibrating Sample Magnetometer

The basic measurement is accomplished by oscillating the sample near a detection (pickup) coil and synchronously detecting the voltage induced [9]. A compact pickup coil configuration was employed which delivers signal with large oscillation amplitude (1.3 mm peak) operating at a frequency of 40 Hz. The VSM option for the PPMS consists of primarily a VSM linear motor transport (head) for vibrating the sample, a coil-set puck for detection, electronics for driving the linear motor transport and detecting the response from the pickup coils. The working principle of VSM is based on the Faraday's law of induction [10]. When a magnetic sample is placed in a magnetic field, an electro motive force (e.m.f.) will develop in the pickup coil because of the sample vibration which results in the change of magnetic flux seen by the sample. The induced e.m.f. is directly proportional to the magnetization of the vibrating sample. The time-dependent induced voltage is given by the following equation,

$$V_{Coil} = \frac{d\Phi}{dt} = \left(\frac{d\Phi}{dz}\right)\left(\frac{dz}{dt}\right) \text{---------- (2.6)}$$

where Φ is the magnetic flux enclosed by the pickup coil, z is the vertical position of the sample with respect to the coil, and t is time involved.

For a sinusoidally oscillating sample position, the voltage developed is based on the following equation,

$$V_{Coil} = 2\pi f C m A \sin(2\pi f t) \text{ ---------- (2.7)}$$

where: C is a coupling constant, m is the DC magnetic moment of the sample, A is the amplitude of oscillation, and f is the frequency of oscillation.

The acquisition of magnetic moment involves measuring the coefficient of the sinusoidal voltage response from the detection coil. Fig. 2.9 illustrates the pictorial view of PPMS with VSM option.

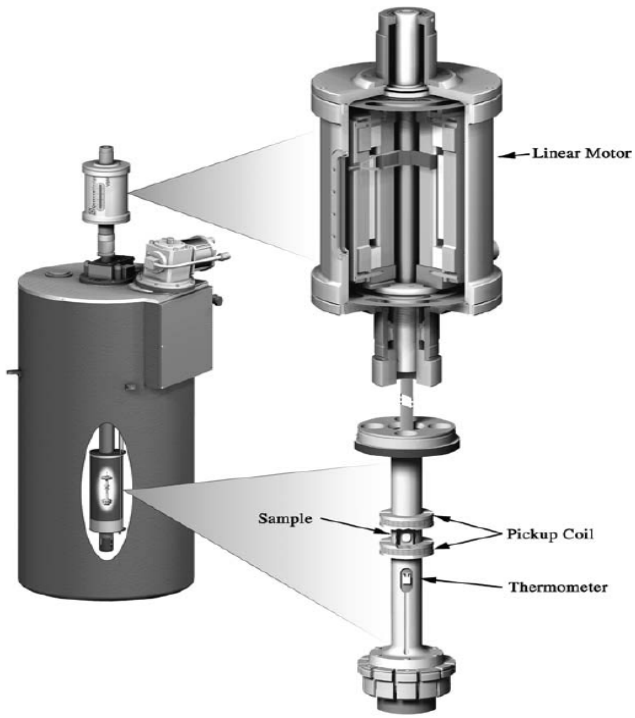

Fig. 2.9. Pictorial representation of VSM head and sample rod arrangement in PPMS-VSM module.

In the present work, sample of approximately 2 mm x 2 mm x 5 mm dimensions were used for PPMS-VSM measurements. The sample is attached to the end of a sample rod that is driven sinusoidally. The voltage induced in the pickup coil is amplified and lock-in detected. The in-phase component of the induced signal is determined and analyzed. The PPMS employed is capable of producing magnetic fields up to 9 T. In the present study, the temperature of the samples was swept in the range 5 K to 360 K.

2.5.3 Calculation of saturation magnetization and magnetic anisotropy constant in Polycrystalline samples

Magnetic anisotropy constant (K_1) as well as the saturation magnetization (M_{sat}) were determined from magnetic isotherms recorded at different temperatures employing 'approach to saturation method' for polycrystalline samples [11]. When magnetization is plotted as a function of $(1/H_i^2)$, a linear

part is active at high fields which can be extrapolated to infinite field $\{(1/H_i^2) \rightarrow 0\}$. This method enables us to determine the value of M_{sat} occurring at the intersection of the linear line with the vertical axis {i.e. value of M at $(1/H_i^2) = 0$}.

The anisotropy field, H_A is calculated as described below. H_x, defined as the intersecting point of the line $1/H_i^2$ of the extrapolated linear part of the curve with the horizontal axis. The relation between H_x and H_A for materials exhibiting uniaxial anisotropy [11] is given as

$$H_A = 3.87\ H_x\ (for\ K_1 > 0) \text{ ---------- (2.8)}$$

Using the eq. (2.8), the anisotropy field, H_A is determined. This value of H_A is used to compute the anisotropy constant K_1 as shown in eq. 2.9.

$$H_A = \frac{2\ K_1}{M_s}$$

$$K_1 = \frac{H_A * M_S}{2} \text{ ---------- (2.9)}$$

2.5.4 Magnetic entropy change

The magnetic entropy change (ΔS_M) through the transformation is calculated from the area under the M-H isotherms recorded at different temperatures [12] within 1-2 K interval in the vicinity of the transformation, employing the following Maxwell's relation

$$\Delta S_M = S\ (T, H) - S\ (T, 0) = \int_0^H \frac{\partial M\ (T,H)}{\partial T} dH \text{ ---------- (2.10)}$$

where ΔS_M is the magnetic entropy change, M is the magnetization at field H and temperature T. The area under the M-H curves, recorded in close temperature intervals, was determined through numerical integration of each curve from 0 to various H_{max} values. The area obtained for the M-H curve at a temperature 'T' is subtracted from that of the adjacent M-H curve corresponding to the next higher

temperature '$T+\Delta T$'. The remaining area is divided by ΔT to get the magnetic entropy change (ΔS_M) corresponding to the average temperature {$T + (1/2)\ \Delta T$}.

2.6 Microstructural characterization

Regardless of whether an application is structural, electronic or optical, the performance of a given material is intimately linked to its microstructure. In this thesis we have carried out the microstructural characterization to study various features present in the samples. Basically the microstructural studies were carried out by Optical microscopy and Field Emission Scanning Electron Microscopy (FESEM). The above mentioned techniques along with the corresponding specimen preparation are briefly discussed below.

For microstructural characterization, samples were sliced into thin sections using a diamond saw (Buehler make, Isomet 1000 model). The specimen preparation technique adopted in this study is as follows: The sections extracted from the samples were mounted using a hot setting Bakelite compound to a size 1" (2.54 cm) dia and 1.5 – 2 cm height. The mounted pieces were initially ground on a SiC paper (600, 800, 1000 and 1200 grits) to make flat surface and was further polished on a polishing cloth using a rotating wheel of the Buehler make polishing machine, using different grades (6, 3, 1 and 0.25 μm) of diamond paste as grinding media. Polishing at each stage was carried out for about 30 minutes with SiC paper and about 60 minutes with diamond paste for obtaining highly polished surfaces. Kerosene was used as the lubricant during polishing. The surface of the sample was cleaned at each stage of polishing using acetone. The polished samples are then ultrasonicated to remove any unwanted deposits from the sample surface that can occur during polishing. The polished samples were observed under an inverted metallurgical optical microscope (Zeiss make, Axiovert model). Twins, the surface relief patterns were observed in the micrographs recorded using optical microscope. In order to find the grain size, sample surfaces were etched using Ferric chloride for about 20-25 seconds. The etched surfaces were mildly re-

polished in the range 3 μm to 0.25 μm and were observed under FESEM. The FESEM micrographs thus obtained were characterized for various microstructural parameters.

2.6.1 Optical microscopy

A wide variety of features such as grain size, grain morphology, inclusions, pores, grain/domain boundaries, defects such as twins, stacking faults etc., define the microstructure of a solid. The observation of polished surface of the material using an optical microscope reveals large amount of information on the material on features such as grains, pores, phase distribution etc. up to a magnification of 1000x. As the optical microscope uses the visible or near visible portion of the electromagnetic spectrum, the white light resolution is limited to 0.2 μm, hence the features of order less than this cannot be studied under optical microscope.

Optical metallography is dependent on the contrast in the features, due to the inherent differences in the absorption characteristics of the phases present in the polished surface of the sample. By using a polarizer, different phases in the polished surface can be easily identified due to the incident light being plane polarized, thus giving a direct measurement of the phase change at the reflecting surface. Since the depth of the field in the light microscopy is practically nil, the specimen surface must be polished to a very high level of reflectivity. In the present study, we have used Zeiss make inverted metallurgical microscope for microstructural characterization.

2.6.2 Field Emission Scanning Electron Microscopy (FESEM)

As discussed in section 2.2, FESEM provides an insight to the microstructural understanding of the present samples. A schematic sketch describing the various detectors equipped to obtain the information from the samples is provided in Fig. 2.10

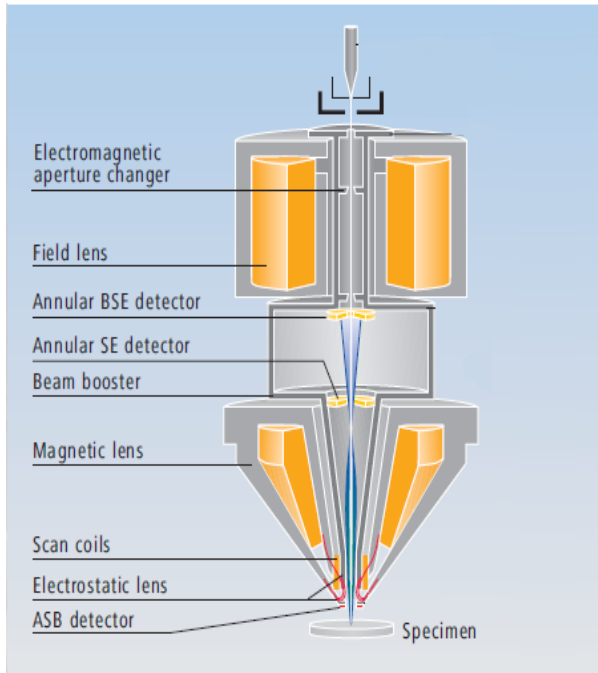

Fig. 2.10. Schematic view of Field Emission –SEM.

The secondary electron imaging can produce very high resolutions of a sample surface, revealing details even in the size range 10 – 100 nm. Due to the very narrow electron beam, SEM micrographs have a large depth of field yielding a characteristic three-dimensional appearance useful for understanding the surface structure of a sample. Back-scattered electrons (BSE) are beam electrons that are reflected from the sample by elastic scattering. BSE are often used along with the spectra derived from the characteristic X-rays. Since the intensity of the BSE signal is strongly related to the atomic number (Z) of the specimen, BSE images can provide information about the distribution of different elements of the sample. It also provides information about different phases present in the sample based on the variation in reflectivity content.

Electron beam of very high energies are employed in order to visualize the sub-surface structures while low energy BSE detection is quite useful for high resolution investigation of charging specimens. This is met through a new In-lens BSE detection system. Characteristic X-rays are emitted when the electron beam removes an inner shell electron from the sample, causing a higher electron to fill

the shell and release energy. The characteristic X-rays are used to identify the composition and measure the abundance of elements in the sample.

In the present work, a FESEM (Model ULTRA 55, Carl Zeiss make) was employed for obtaining the micrographs at low (500x) and high magnifications (5000x). The working distance for most of the cases was in the range 4 – 10 mm. The charging effect of the electron beam on the sample was bypassed by either creating a silver paint / strip channel from the holder to the sample.

2.7 Mechanical properties characterization

2.7.1 Microindentation (Vickers microindentation)

Hardness measurements quantify the resistance of a material to plastic deformation represents an arbitrary quantity used to characterize a material on a scale [13]. Microindentation tests typically employ forces less than 2 newton (N). The Vickers microhardness test is one of the most widely applicable hardness tests. It uses a pyramidal indenter mounted on a square diamond base. In microindentation hardness testing, a diamond indenter of specific geometry is impressed onto the surface of the test specimen using a known applied force in the range 1 to 1000 gram-force (gf). Due to their specificity, microhardness testing can be used to observe changes in hardness on the microscopic scale. A Vickers hardness tester (Leica Make, LV 700 AT model) is used in the present study in order to carry out the indentation tests. The schematic representation of Vickers microindentation is shown in Fig. 2.11.

In the Vickers test, the load is applied smoothly, without impact and is held on to the sample for about 10-15 seconds. The quality of the indenter and the accuracy of the applied load must be controlled to get the correct results. After the load is removed, the two diagonals (d_1 and d_2) of the impression are measured and then averaged (d).

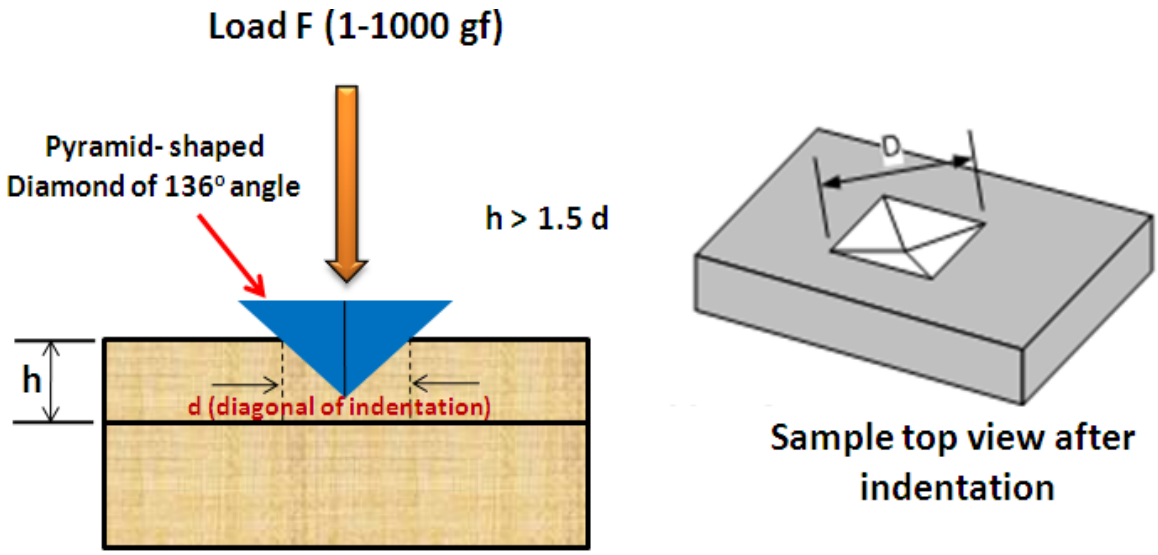

Fig. 2.11. Schematic view of Vickers microindentation measurement.

The Vickers hardness (HV) is calculated by using the following formula [13, 14]

$$HV = 1854.4\left(\frac{L}{d^2}\right) \text{---------- (2.11)}$$

where the load L is in gram-force and the average diagonal d is in μm. The hardness is expressed in the units of kg-f/mm^2. The constant value (1854.4) in Eqn. 2.11 depends on the experimental configuration used.

For any given load, the hardness increases rapidly at low diagonal lengths, with the effect becoming more pronounced as the load decreases. Thus at low loads, small measurement errors will produce large deviations in the hardness values. Thus, it is beneficial to employ the higher loads in the measurements. It is also required to gently polish the surface of the samples prior to indentation making sure that work-hardening has not affected the material.

2.7.2 Compressive stress-strain

In order to investigate the mechanical properties of the bulk materials under compression, stress-strain measurements were carried out on the samples using Instron 5500R test machine (Fig. 2.12). It contains load frames comprising of a base, two columns, a crosshead, and a top plate. This structure forms a rigid closed frame with high stiffness to reduce the deflection of the load frame under load [15]. A load cell is mounted on the crosshead to measure the applied load.

Fig. 2.12. Compression test setup (INSTRON make, 5500R model) used to record stress-strain curves.

A pair of grips or fixtures is then mounted on the load cell and the frame base. The grips or fixtures secure a specimen of material in place. When a test starts, the crosshead moves up or down applying a tensile or compressive load on the specimen. The load cell converts this load into an electrical signal that the controlling software can measure and display. The control may be based on crosshead position, load, or strain. The load from the load cell, the stress (in MPa) and the cross head position difference, the strain (in mm) are measured and plotted. Mechanical properties like martensitic reorientation stress (Yield stress), compression strength and fracture stress; and their corresponding strains can be obtained from the stress-strain curves.

In the present study, we have recorded stress- strain curves using a 1 kN load cell during both loading and unloading processes. In order to find out the shape memory strain in the samples, unloading curve was recorded and the sample was heat treated to a temperature of 150 ^{o}C (above martensitic temperature) and was then cooled to room temperature.

2.7.3. Shape memory properties

Shape memory characteristics were measured using compressive stress-strain curves at a constant temperature. At room temperature, say the length of the sample before application of load is represented by l_0. After loading to the compression strength and then unloading, the length of the sample changes to l_1 and then after heating the sample to 150 ^{o}C and cooling it back to RT, the length of the sample is say l_2.

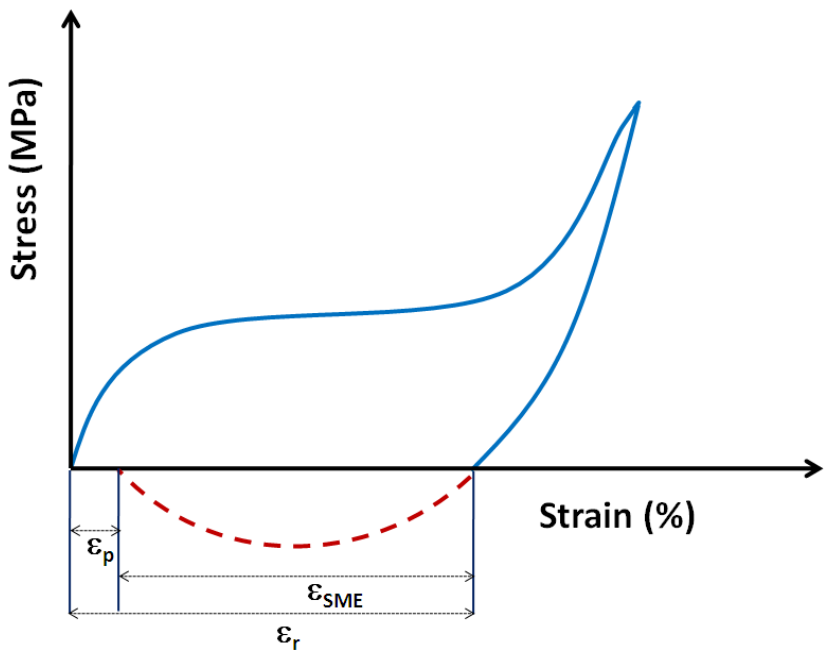

Fig. 2.13. Schematic representation of stress-strain curve during loading and unloading is shown. The dotted line indicates the recovery on heating the sample to austenite phase after unloading.

The residual strain (ε_r) is defined as the amount of strain remaining after unloading the sample which is determined as the ratio [($l_0 - l_1$) / l_0] x 100 [16]. Permanent strain (ε_p) is defined as the amount of unrecoverable strain after heating the sample to austenite phase and then cooling. It is defined as [($l_0 - l_2$) / l_0] x 100. A schematic representation of stress-strain curve is shown in Fig. 2.13.

Shape memory strain (ε_{SME}) is then obtained by subtracting the permanent strain (ε_p) from the residual strain (ε_r), (ε_r - ε_p) which can be defined as the ratio [($l_1 - l_2$) / l_0] x 100. The strain recovery ratio (R) is defined as

$$R = \left(\frac{\varepsilon_{SME}}{\varepsilon_{SME}+\varepsilon_P}\right) * 100 \quad \text{..... (2.16)}$$

In the present study, the values of l_0, l_1 and l_2 are determined for all the samples and the shape memory properties defined above are determined.

References

[1] http://en.wikipedia.org/wiki/Vacuum_induction_melting

[2] www.mcswiggen.com/pdf%20files/TechNote_WDS vsEDS.pdf

[3] M. Couach and A. F. Khoder, *Magnetic susceptibility of Superconductors and other Spin systems*, (Plenum, Newyork) (1992).

[4] S. D. Murphy, K. Renouard, R. Crittenden and S. M. Bhagat, *Solid State Commun.* **69** (1989) 367.

[5] http://en.wikipedia.org/wiki/Differential_scanning_calorimetry

[6] B. D. Cullity, *Elements of X-ray diffraction*, Addison-Wesley Publishing (1956).

[7] David B. Williams and C. Barry Carter, *Transmission Electron Microscopy*, p. 142 .

[8] L. Reimer and H. Kohl, *Transmission Electron Microscopy*, Fifth Ed. Springer Publications, p. 1-2.

[9] S. Foner, *Rev. Sci. Instr.* **30** (1959) 548.

[10] B. D. Cullity, *Introduction to Magnetic Materials*, Addison-Wesley Publishing (1972).

[11] H. Zijlstra, *Experimental Methods in Magnetism*, Vol. **2**, (1967) p.182-185.

[12] V.K. Pecharsky and K.A. Gschneidner, Jr., *Phys. Rev. Lett.* **78** (1997) 4494.

[13] F. George, Vander Voort and Gabriel Lucas of Buehler Ltd. September, 1998 edition of Advanced Materials and Processes.

[14] R.J.D. Tilley, *Understanding Solids*, John Wiley & Sons, England (2004).

[15] http://msc-technology.wikispaces.com/Structures

[16] Y. Suzuki, Y. Xu, S. Morito, K. Otsuka and K. Mitose, *Mater. Lett.* **36** (1998) 85.

Chapter 3

Investigations on $Ni_{53.5}Mn_{26.0}Ga_{20.5}$ alloy that exhibits both shape memory and magnetocaloric effects

3.1 Introduction

Ferromagnetic shape memory alloys of Ni-Mn-Ga system undergo a first order structural transformation from high symmetry austenite to low symmetry martensite phase on cooling. In order to tune the martensitic transformation temperatures of the Ni-Mn-Ga alloys, one can either vary its composition [1-3] or introduce other elements by substitution [4-9]. The structural transformation temperature (austenite to martensite) T_M and the magnetic transition (ferro- to paramagnetic) temperature T_C, of the off-stoichiometric compositions of Ni–Mn–Ga system are sensitive not only to composition but also to the atomic order [1–3, 10-12]. Alloys exhibiting $T_M < T_C$, $T_M > T_C$ or $T_M \sim T_C$ are suitable for applications in devices employing magnetic shape memory (MSM) effect, high-temperature shape memory effect (SME) and magnetocaloric effect [13–15], respectively. The alloys with superstructural ordering (or lattice modulation) are known to have low twinning energies and are found to exhibit a large MSM effect if they possess high magnetic anisotropy energy. Such properties are reported for many Mn-rich compositions [16]. Thus, compositions showing lattice modulation and having $T_C >> T_M >$ operating temperature (room temperature, RT) are potential candidates for MSM applications at RT. Coupled magneto-structural transitions (when $T_M \sim T_C$) have been reported for Ni-rich, Mn-poor alloys of $Ni_{2+x}Mn_{1-x}Ga$ (x = 0.18 - 0.28) system [17] which crystallize in a non-modulated tetragonal structure. In this system, T_M has been observed to increase from 202 K for x = 0 to 330 K for x = 0.18, following an increase in valence electron concentration, e/a. For these alloys, the structural transformation occurs below T_C. Alloys with x > 0.28 have $T_M > T_C$,

and show no lattice modulation. Substitution of excess Ni for Ga (rather than for Mn) can cause a larger change in e/a and thus a faster increase in T_M, and would not dilute the magnetic subsystem. Lanska *et al.* [2] have discussed the correlations between the average electron per atom (e/a) ratios and the 5M, 7M lattice modulations and non-modulated tetragonal structure. The general trend reveals that 5M and 7M modulations are observed [18, 19] for compositions with e/a below a critical value of 7.7. In this chapter, we present the results on a Ni-rich, Ga-poor $Ni_{53.5}Mn_{26.0}Ga_{20.5}$ alloy which crystallizes as a ferromagnetic modulated martensitic phase and exhibits both shape memory and magneto-caloric effects at RT.

3.2 Structural and magnetic transitions

3.2.1 Differential scanning calorimetry (DSC)

In order to determine the structural and magnetic transitions Differential Scanning Calorimetry (DSC) scans were recorded in the temperature range 200 – 500 K during heating and cooling cycles.

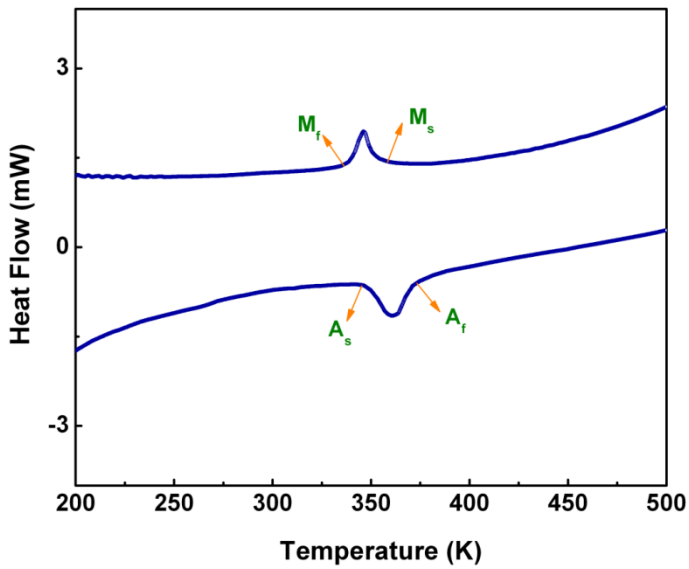

Fig. 3.1. DSC scan of $Ni_{53.5}Mn_{26.0}Ga_{20.5}$ alloy showing structural transformations. The characteristic transformation temperatures are indicated by arrows during heating and cooling cycle.

The characteristic temperatures of martensitic transformation, viz. martensitic start (M_s), finish (M_f) during cooling and austenite start (A_s) and finish (A_f) during heating, indicated in the DSC scan as shown in Fig. 3.1 are found to be 351.4 K, 339.8 K, 347 K and 352 K. The magnetic transition at T_C is not clearly seen. The T_M values are calculated as $(M_s+M_f+A_s+A_f)/4$.

3.2.2 ac susceptibility

Temperature dependence of low field ac susceptibility measurements was carried out at 33 Hz, H = 10 Oe using a home-made set up in a temperature range 300 – 400 K and is shown in Fig. 3.2. The figure shows that this alloy exhibits coupled magnetostructural transformations, from which T_M and T_C are determined to be 347 K and 351.4 K respectively. The structural transformation is very sharp, with a thermal hysteresis of ~4 K, typical of thermo-elastic shape memory alloys. The value of T_M measured from ac susceptibility is consistent with that from DSC measurements.

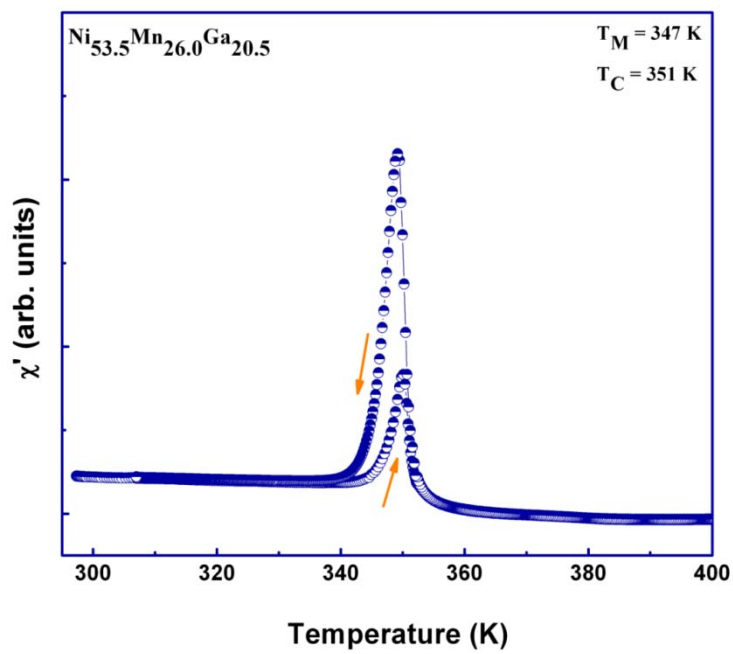

Fig. 3.2. Temperature dependence of ac susceptibility showing coupled magneto structural transformations in the range 347- 351 K in $Ni_{53.5}Mn_{26.0}Ga_{20.5}$ alloy.

In DSC, the enthalpy change at the second order transition from ferro- to paramagnetic state is usually rather small, compared to that across the first order structural transformation. T_M and T_C being in close proximity in this alloy could be the reason for not observing the step near magnetic transition in DSC.

3.3 Crystal structure studies

3.3.1 X-ray diffraction studies

In order to determine the crystal structure of the alloy, powder X-ray diffraction studies were carried out at RT. X-ray diffractogram was recorded with using Cu K_α radiation. As the scattering factors of Ni and Mn are very close by, one cannot determine the type of modulation from the X-ray diffraction studies alone accurately. Hence, Transmission electron microscopy (TEM) – Selected area electron diffraction (SAED) studies were carried out, to obtain precise information about the modulation present in the sample.

3.3.2 TEM-Selected Area Electron Diffraction (SAED)

Sample preparation for selected area electron diffraction (SAED) measurements using TEM was carried out as discussed in section 2.4.4 of Chapter 2. Fig. 3.3 (a) shows a bright-field image obtained using TEM and it reveals twinning on a fine scale. This image is typical of what could be observed across the sample and shows a single variant with occasional crossing twins. The selected area electron diffraction (SAED) pattern from the sample in the [0 1 0] zone axis is shown in Fig. 3.3(b). The pattern confirms the crystal structure to be monoclinic with b = 92.91(1)^o and exhibiting sevenfold modulation along the [0 0 1] direction.

The lattice parameters determined from SAED pattern were used to index the X-ray diffraction pattern. Fig. 3.4 shows the indexed X-ray diffraction pattern to monoclinic structure with seven layer modulation. The corresponding lattice parameters were determined to be a = 4.243(1) Å, b = 5.520(1) Å, c = 29.476(5) Å and β = 92.91(3)^o.

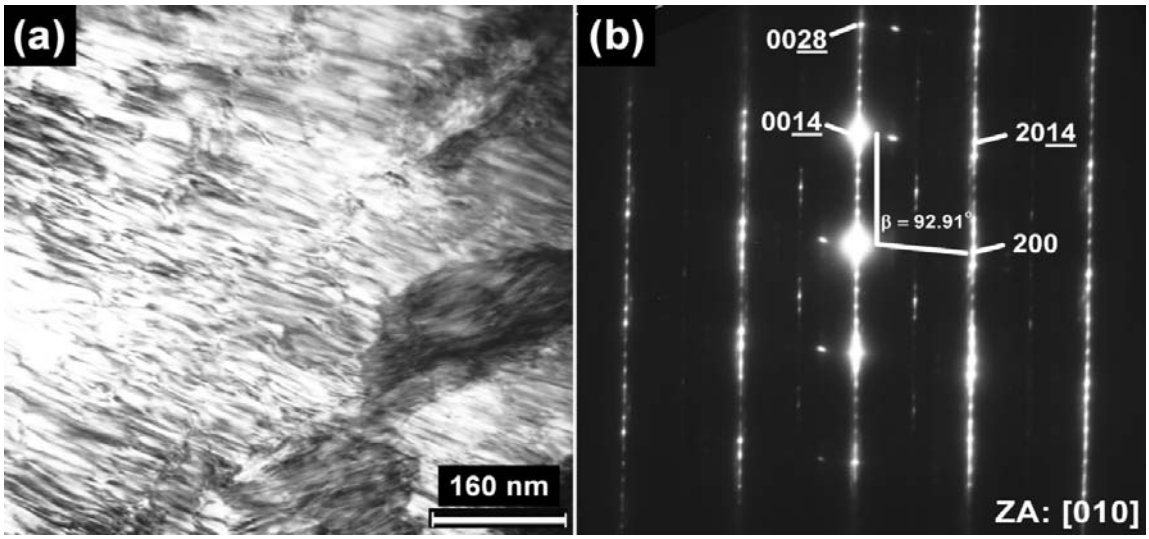

Fig. 3.3. (a) TEM-Bright field image of $Ni_{53.5}Mn_{26.0}Ga_{20.5}$ alloy at RT, (b) the corresponding selected area electron diffraction (SAED) pattern at RT along [010] zone axis.

To our knowledge, this is the first observation of a modulated crystal structure in a Ni-rich, Ga-poor Ni–Mn–Ga alloy. It should be noted that, although *e/a* of 7.785 for the present alloy is more than 7.7 reported as the maximum limit for lattice modulation, it exhibits 7M modulation in the martensitic state.

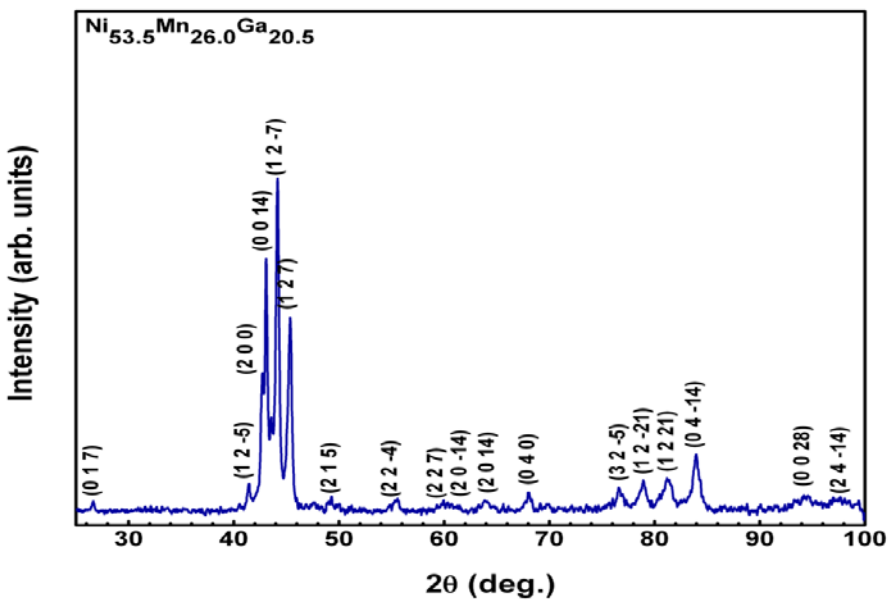

Fig. 3.4. Powder X-ray diffraction pattern of $Ni_{53.5}Mn_{26.0}Ga_{20.5}$ alloy, indexed to monoclinic 7M structure.

The present composition is close to the $Ni_{53.1}Mn_{26.6}Ga_{20.3}$ (e/a = 7.780) and $Ni_{54}Mn_{25}Ga_{21}$ (e/a = 7.781) compositions reported in literature, but these alloys crystallize in non-modulated tetragonal structure with no superstructural ordering [20, 21]. Observation of lattice modulation is known to depend not only on the composition but also on the heat-treatment schedule [22, 23]. We observe that induction melting followed by fast quenching is a crucial processing step of the present alloy, responsible for obtaining a modulated structure. We had aimed at increasing T_M of the stoichiometric Ni_2MnGa (which is at 202 K) through substitution of excess Ni for Ga. This approach enhanced the martensitic transformation to 347 K. The sample, being in a ferromagnetic state (T_C = 351 K), had enabled lattice modulation to be observed at RT. Thus the substitution of excess Ni for Ga has produced an alloy that shows a modulated crystal structure at an e/a of 7.785.

3.4 Microstructural characterization

The method adopted for mounting and polishing the samples for microstructural characterization were discussed in section 2.6 of Chapter 2.

3.4.1 Observation of multimode twinning

Fig. 3.5 shows the optical microstructures recorded at different locations of the sample at RT. Different types of twinning modes were observed, namely parallel bands, crossing twins, twins within twins etc. Observation of different types of twinning modes indicates the multimode twinning in the sample. The widths of the martensitic twin variants vary from 6 – 10 μm.

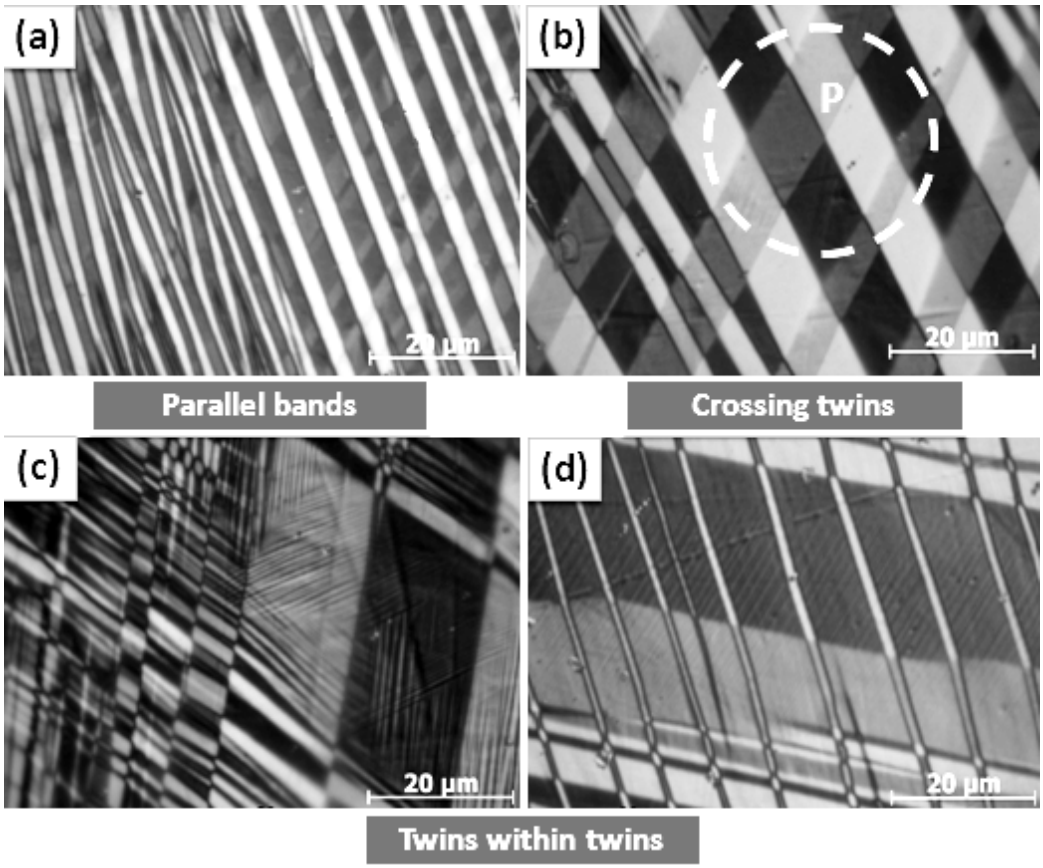

Fig. 3.5. Optical microstructure of the $Ni_{53.5}Mn_{26.0}Ga_{20.5}$ alloy recorded at RT showing multimode twinning including crossing twins, parallel bands and twins within twins as shown in (a), (c) and (d).One of the fourfold corners is enclosed by a circle with center at P in (b).

The microstructures exhibit self-accommodation of several twin variant modes, with a predominance of crossing twins similar to those observed in Cu–Al–Ni [24] and the R-phase of the Ni–Ti–Fe system, which crystallizes in monoclinic structure [25].

3.4.2 Multimode twinning: correlation to low stress concentration

Clear formation of fourfold corners due to the crossing twins can be seen in Fig 3.5 (b). Four interfaces separating four different variants appear to meet along a line which goes into the plane of the paper at each corner, as was observed for Cu–Al–Ni [24]. All the twin boundaries can be seen to be sharp and straight all the way to the corner. Crossing twins of different sizes with twin variant widths

mostly ranging from 6 to 10 μm are observed at different locations of the sample. The formation of a large variety of twin modes, like parallel bands, twins within twins and crossing twins, throughout the sample is indicative of low residual stresses in the martensitic phase. They form to minimize the accumulated elastic strain through structural transformation and are typical of transformation from cubic austenite to martensite of monoclinic symmetry [26, 27]. This morphology is distinct from those reported for several Ni–Mn–Ga alloys in which transformation from cubic to tetragonal/orthorhombic symmetry takes place. The observation of multi-mode twinning in the present composition may be a consequence of the multi-well nature of energy density with its origin in the long-range superstructural ordering of the low-symmetry monoclinic unit cells of the present composition.

3.5 Magnetic entropy change

The coupled magneto structural transformation observed in this alloy suggests that a considerable magnetic entropy change (ΔS_M) is likely to occur across the transformations. To estimate ΔS_M, magnetization (M-H) isotherms were recorded at different temperatures in the range 338-360 K, with an interval of 2 K and for fields up to 5 T, during heating.

Magnetic entropy change (ΔS_M) is calculated from the area under the isotherms by employing the following Maxwell's relation

$$\Delta S_M = S(T,H) - S(T,0) = \int_0^H \frac{\partial M(T,H)}{\partial T} dH \quad \text{---------- (3.1)}$$

Isotherms recorded in the vicinity of T_M while heating are shown in Fig. 3.6 (a). The corresponding ΔS_M plotted against the temperature is shown in Fig. 3.6 (b). Variation of ΔS_M is systematic with an increase in the field, as can be seen in Fig. 3.7. The maximum value of ΔS_M at 351 K is found out to be 13.9 J/kg-K. The values of ΔS_M reported for Ga-poor alloys in literature vary from 3 to 15.6 J/kg-K for a field of 5 T [28, 29]. In this context, the present value with ~14 J/kg-K is

considerable and is useful since devices employing Ga-poor alloys would be more economical.

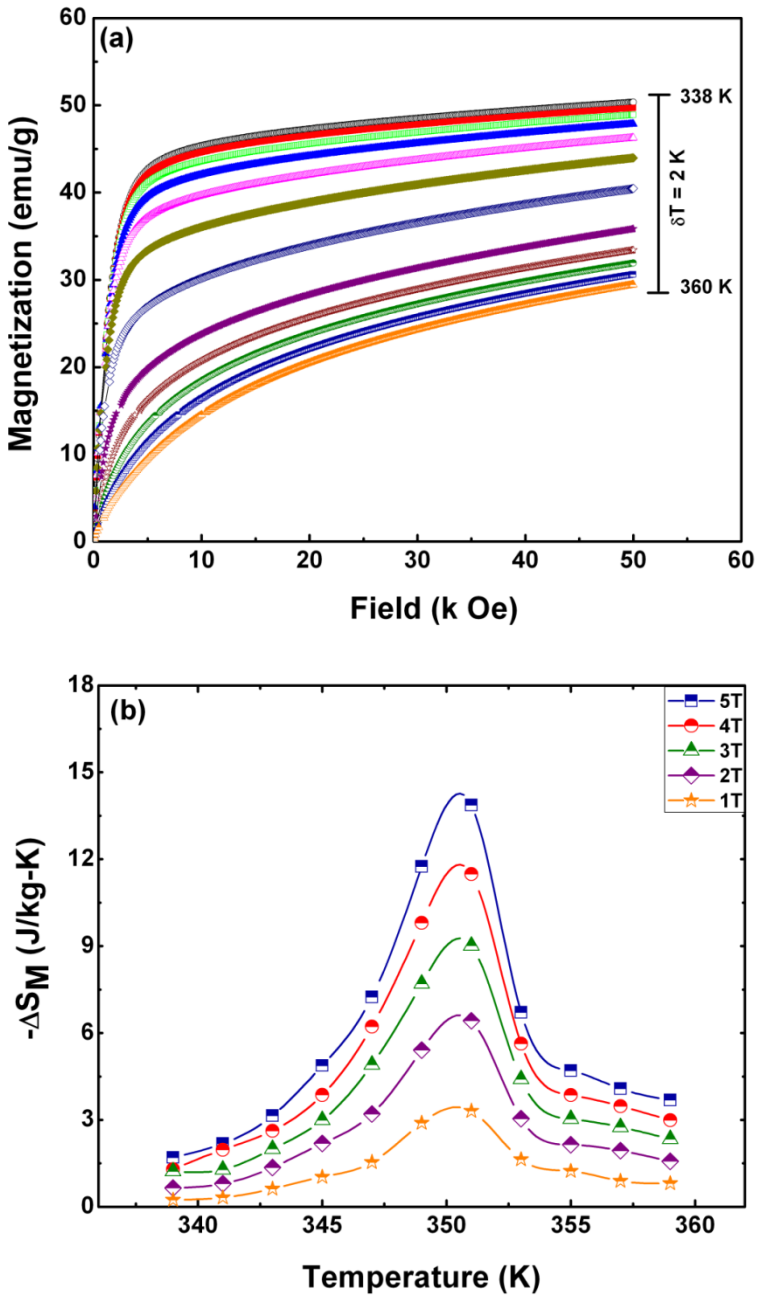

Fig. 3.6. (a) Magnetic isotherms recorded during heating in the temperature range 338 – 360 K with an interval of 2 K up to a field of 5 T. (b) Magnetic entropy change determined from the isotherms taken up to different fields, showing a peak at 351 K.

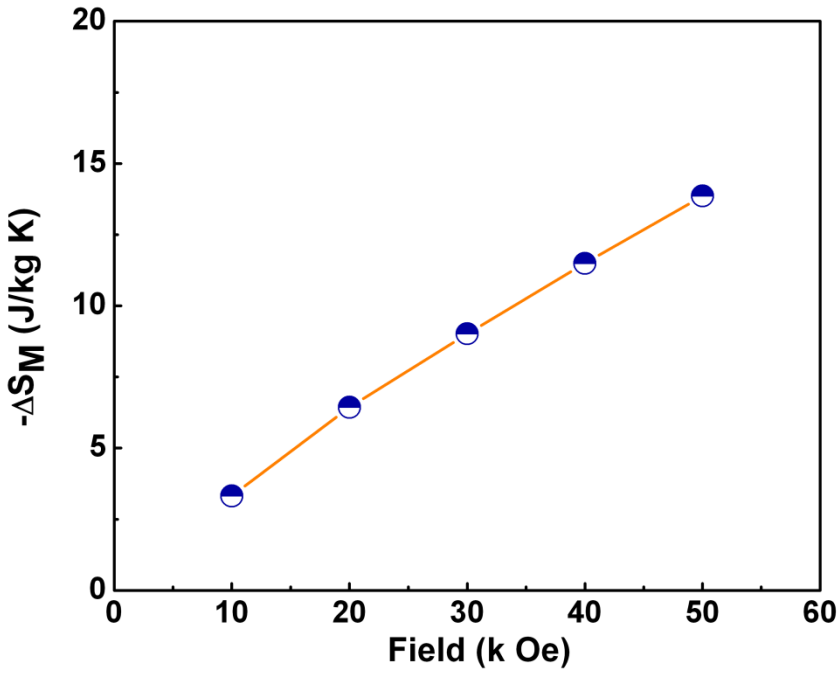

Fig. 3.7. Variation of magnetic entropy change with field showing a linear trend.

3.6 Mechanical properties

3.6.1 Compressive stress-strain curves: shape memory properties

To assess the effect of low residual stresses indicated by the microstructure on the mechanical behavior of the alloy, stress–strain curve under compression was obtained at RT using INSTRON 5500R materials testing machine. The stress-strain curve during loading and unloading for the present sample is shown in Fig. 3.8.

The initial linear part of the stress–strain curve, terminating at 12 MPa and a strain of 0.48%, corresponds to the martensitic reorientation stress (yield stress) and elastic strain, respectively, and the apparent compressive strength and compressive strain of the sample are 124 MPa and 5.2%. The sample shows a faster deformation rate beyond 5% strain. The residual strain (ε_r) after unloading from 124 MPa is 1.8% and the recoverable strain after heating the sample to 150 ^{o}C is 1.6%, leaving a residual irreversible strain (ε_p) of only 0.2%. Thus the maximum SME (ε_{SME}) obtained in the present polycrystalline alloy is 1.6% with a

strain recovery ratio of 89% (1.6% out of 1.8%). Much higher compressive strengths, in excess of 200 MPa at 5% strain, and yield strength of more than 100 MPa have been reported for $Ni_{54}Mn_{25}Ga_{21}$ alloy with a similar composition [21]. However, this composition crystallizes in a non-modulated tetragonal structure, has $T_M > T_C$ and is proposed for high-temperature shape memory application. Non-modulated structures are known to have larger twinning energy and hence higher yield stress [16].

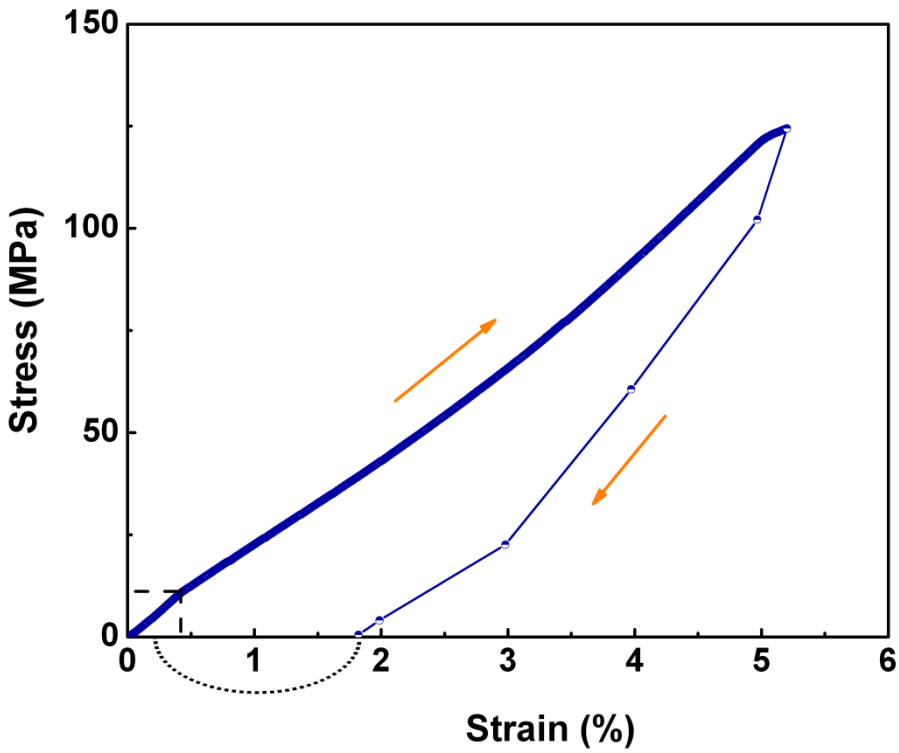

Fig. 3.8. Stress–strain curve, obtained when loaded under compression, of the polycrystalline $Ni_{53.5}Mn_{26.0}Ga_{20.5}$ alloy on loading (↑) and unloading (↓). The dotted line from a strain of 1.8 % to 0.2% indicates the strain recovery upon heating.

3.6.2 Correlation of shape memory effect to microstructural features

The fact that large SME and a high strain recovery ratio of 89% is obtained in the present Ni-rich $Ni_{53.5}Mn_{26.0}Ga_{20.5}$ alloy in polycrystalline form is very exciting and is attributed to the favorable crystal structure and microstructural

features. Stabilization of the martensitic transformation in the ferromagnetic state of the present Ni excess composition, might have a role to play in obtaining lattice modulation, unlike in similar compositions reported in literature. Relatively lower reorientation stress, low compressive strength, considerable strain and large recovery ratio, observed for the present sample in polycrystalline form, are indicative of low twinning energy. This is attributed to the lattice modulation and the low residual stresses in the martensitic phase caused by self-accommodation with multi-mode twinning These originate during the transformation from high symmetry cubic austenite to low symmetry monoclinic structure with multi-well nature of energy density.

3.7 Conclusions

Detailed structural, magnetic, microstructural and mechanical studies are carried out on $Ni_{53.5}Mn_{26.0}Ga_{20.5}$, which is an off-stoichiometric composition with excess Ni doped for Ga, in Ni_2MnGa.

This alloy exhibits magneto-structural transition close to 351 K. This composition crystallizes into a monoclinic structure with 7M superstructural ordering and has e/a = 7.785, greater than the proposed critical value (upper limit) of 7.7 for lattice modulation.

Distinct microstructural features with multi-mode twinning are observed which indicate low residual stresses in the polycrystalline alloy under study and are believed to originate from a low-symmetry monoclinic phase.

Considerable magnetic entropy change of 13.9 J/kg-K was observed for a magnetic field of 5 T during heating. Observation of considerable magnetic entropy change is attributed to the coupled magnetostructural transformations where T_M is observed close to T_C.

The low yield stress and large strain recovery observed are attributed to the low twinning energies in the martensitic phase, evidenced by lattice modulation and the self-accommodation through multi-mode twinning

throughout the polycrystalline sample. The present alloy can be very attractive for shape memory applications above RT in polycrystalline form.

References

[1] V. Sánchez-Alarcos, V. Recarte, J.I. Pérez-Landazábal and G.J. Cuello, *Acta Mater.* **55** (2007) 3883.

[2] N. Lanska, O. Söderberg, A. Sozinov, Y. Ge, K. Ullakko and V.K. Lindroos, *J. Appl. Phys.* **95** (2004) 8074-8078.

[3] K. Ullakko, Y. Ezer, A. Sozinov, G. Kimmel, P. Yakovenko and V.K. Lindroos, *Scripta Mater.* **44** (2001) 475.

[4] I. Glavatskyy, N. Glavatska, O. Söderberg, S-P. Hannula and J-H. Hoffmann, *Scripta Mater.* **54**(2006) 1891.

[5] D.Y. Cong, S. Wang, Y.D. Wang, Y. Ren, L. Zuo and C. Esling, *Mater. Sci. Eng. A* **473** (2008) 213.

[6] A. Satish Kumar, M. Ramudu and V. Seshubai, *J. Alloys Compd.* **509** (2011) 8215.

[7] D. Kikuchi, T. Kanomata, Y. Yamaguchi, H. Nishihara, K. Koyama and K. Watanabe, *J. Alloys Compd.* **383** (2004) 184.

[8] D. Kikuchi, T. Kanomata, Y. Yamaguchi and H. Nishihara, *J. Alloys Compd.* **426** (2006) 223.

[9] D.E. Soto-Parra, F. Alvarado-Hernandez, O. Ayala, R.A. Ochoa-Gamboa, H. Flores-Zúñiga and D. Rios-Jara, *J. Alloys Compd.* **464** (2008) 288.

[10] V.A. Chernenko, E. Cesari, V.V. Kokorin and I.N. Vitenko, *Scr. Metall. Mater.* **33** (1995) 1239.

[11] V.V. Khovailo, K. Oikawa, T. Abe and T. Takagi, *J. Appl. Phys.* **93** (2003) 8483.

[12] C. Jiang, Y. Muhammad, L. Deng, W. Wu and H. Xu, *Acta Mater.* **52** (2004) 2779.

[13] X. Zhou, W. Li, H.P. Kunkel and G. Williams, *J. Mag. Mag. Mater.* **293** (2005) 854.

[14] Y. Ma, C. Jiang, Y. Li, H. Xu, C. Wang and X. Liu, *Acta Mater.* **55** (2007) 1533.

[15] A. Planes, L. Manosa and M. Acet, *J. Phys.: Condens. Matter* **21** (2009) 233201.

[16] O. Söderberg, Y. Ge, A. Sozinov, S-P. Hannula and V.K. Lindroos, *Smart Mater. Struct.* **14** (2005) S223.

[17] V.V. Khovaylo, V.D. Buchelnikov, R. Kainuma, V.V. Koledov, M. Ohtsuka, V.G. Shavrov, T. Takagi, S.V. Taskaev and A.N. Vasiliev, *Phys. Rev. B* **72** (2005) 224408.

[18] K. Tsuchiya, H. Nakamura, D. Ohtoyo, H. Nakayama, H. Ohtsuka and M. Umemoto, in Proceedings of ISAEM 2000: 2nd International Symposium on Designing, Processing, and Properties of Advanced Engineering Materials, Guilin, China, 20–21 October 2000 Interscience Enterprises, Ltd., Switzerland, 2001, pp. 409.

[19] V.A. Chernenko, V. L'vov, E. Cesari, J. Pons, R. Portier and S. Zagorodnyuk, *Mater. Trans., JIM* **43** (2002) 856.

[20] V.A. Chernenko, V. L'vov, J. Pons and E. Cesari, *J. Appl. Phys.* **93** (2003) 2394.

[21] Y. Li, Y. Xin, C. Jiang and H. Xu, *Scripta Mater.* **51** (2004) 849.

[22] U. Gaitzsch, S. Roth, B. Rellinghaus and L. Schultz, *J. Magn. Magn. Mater.* **305** (2006) 275.

[23] U. Gaitzsch, M. Pötschke, S. Roth, N. Mattern, B. Rellinghaus and L. Schultz, *J. Alloys Compd.* **443** (2007) 99.

[24] C. Chu and R.D. James, *J. De Physique IV* **C8** (1995) 143.

[25] T. Fukuda, T. Saburi, K. Doi and S. Nenno, *Mater. Trans., JIM* **33** (1992) 271.

[26] M. Nishida, H. Ohgi, I. Itai, A. Chiba and K. Yamauchi, *Acta Metall. Mater.* **43** (1995) 1219.

[27] K. Bhattacharya, *Microstructure of Martensite*, (Oxford University Press, Oxford, 2003), p. 83.

[28] X. Zhou, W. Li, H.P. Kunkel and G. Williams, *J. Mag. Mag. Mater.* **293** (2005) 854.

[29] X. Zhou, H. Kunkel, G. Williams, S. Zhang and X. Desheng, *J. Mag. Mag. Mater.* **305** (2006) 372.

Chapter 4

Influence of boron addition on the structural and microstructural properties of $Ni_{53.5}Mn_{26.0}Ga_{20.5}$ alloy

4.1 Introduction

Though the shape memory alloys of Ni-Mn-Ga system have attracted wide attention of several research groups due to their multifunctional properties, there is a need to fine tune the relevant properties of these materials to suit the selected application. Practical application of Ni-Mn-Ga alloys as actuators is constrained by their extreme brittleness and low strength. In order to overcome these drawbacks one has to suitably modify the microstructures of these materials. It is well known from detailed investigations on Ni-Al [1, 2], Cu-Ni-Al [3, 4] and Ti-Pd-Ni [5-7] alloys, that modifications brought about in the microstructures of the martensitic phase of these materials have a strong bearing on the resultant mechanical properties.

This is done by either varying its composition [8-10] or by introducing other elements by substitution. Substitution of other transition metals for Ni or Mn, and of p- metals for Ga in Ni-Mn-Ga system [11-16] are known to alter the transition temperatures and physical properties of these materials significantly. Rare earth elements when introduced into Ni-Mn-Ga show low solubility and segregate at the grain boundaries [17]. One can also tune the martensitic transformation temperatures of the Ni-Mn-Ga system, by introducing non-magnetic boron with small atomic radius. Boron may occupy either the regular site in the crystal lattice or, an interstitial site due to its small size. Boron introduction into Ni_3Al [18] and Ti-Pd-Ni [7] compounds is known to cause

considerable changes in the microstructures which in turn alter their mechanical properties [7, 17-19].

Recently the effect of boron substituted for Mn and Ga on the structural and magnetic transformation temperatures were reported from a study of $Ni_2Mn_{1-x}B_xGa$ [20] and $Ni_2MnGa_{1-x}B_x$ [21] series. In the former system, both T_M and T_C were found to decrease by nearly 28% with B substitution by x = 0.12, and for x > 0.12 no martensitic phase was observed. Substitution of B for Ga in the latter system had caused a 37% increase in T_M and a marginal reduction in T_C. Similar trend in T_M and T_C was observed on substitution of B for Sb in $Ni_{50}Mn_{36.5}Sb_{13.5-x}B_x$ system [22]. The reduction in T_M discussed above on substitution of B for Mn in $Ni_2Mn_{1-x}B_xGa$ system follows the general trend reported in literature that T_M increases with an increase in electron concentration (e/a). However, increase in T_M observed in the other two systems where B is substituted for Ga or Sb could not be explained on similar lines.

The effect of boron addition up to 5 at.% as an interstitial was studied in $Ni_{46}Mn_{43}Sn_{11}$ system [23]. It was reported that the $L2_1$ crystal structure was retained on B addition, but a small increase in the lattice parameters was observed which was attributed to occupation of interstitial sites by B. Addition of 5 at.% B to $Ni_{46}Mn_{43}Sn_{11}$ alloy causes a large (39%) increase in T_M while T_C increases marginally. Addition of more than 3 at.% B was found to result in multi-phase compounds containing Mn_2B phase [23].

Introduction of boron is known to be very effective in improving room temperature ductility of $L1_2$-type ordered intermetallic alloy Ni_3Al, which is inherently brittle [1, 2]. This results from the segregation of boron containing phase at grain boundaries. However, higher concentrations of boron were found to result in large amount of precipitation of B-rich phase making Ni_3Al brittle. The optimum content of boron was reported to be 0.08 at.% for maximum ductilization of Ni_3Al [24]. Boron was also used to improve room temperature ductility of Cu-Al-Ni [3, 4], Cu-Zn-Al [25] and Ti-Pd-Ni [5-7] shape memory alloys. There are no reports in literature on the effect of boron on the microstructural

features of Ni-Mn-Ga alloys. Hence the correlation of transformation temperatures to microstructural alterations brought about by boron has not been explored. The effect of boron on the superstructural ordering in Ni-Mn-Ga alloys is also not investigated.

We have discussed, in the previous chapter, the properties of $Ni_{53.5}Mn_{26.0}Ga_{20.5}$ alloy that crystallizes with 7M lattice modulation of a monoclinic unit cell. It is found to exhibit a coupled magnetostructural transformation, above RT, at around 347 – 351 K. It also shows remarkable shape memory effect [26]. In the present chapter, we discuss the effect of addition of boron on the transformation temperatures, superstructural ordering and microstructural properties of the above alloy, through investigations on the $Ni_{53.5}Mn_{26.0}Ga_{20.5}B_x$ (x = 0, 0.5 and 1) alloys.

4.2 Phase transformations

Structural transformation temperatures during heating and the magnetic transition temperature were determined using home-built low field ac susceptibility setup operated at 33 Hz, in the temperature interval 200 – 400 K. Fig. 4.1 (a) shows the temperature dependence of low field ac magnetic susceptibility measured in the samples under study, recorded during heating and cooling.

The structural transformation temperatures, namely A_s, A_f, M_s and M_f obtained during heating and cooling cycles of ac susceptibility are listed in Table 4.1 for the three alloys, along with their magnetic transition temperatures. Compositions of the alloys were determined from EDS considering a large frame area of 1.2 x 1.0 sq. mm in different regions of the sample and their average is presented in Table 4.1.

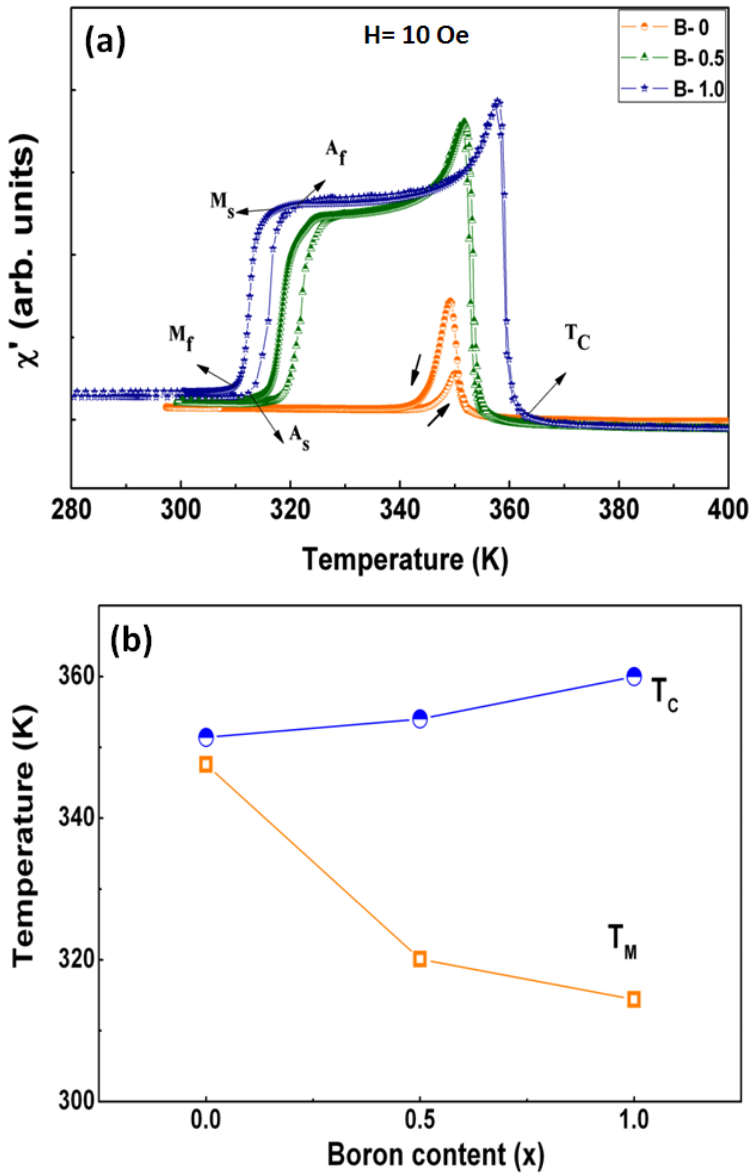

Fig. 4.1 (a) Temperature dependence of ac susceptibility during heating (↑) and cooling (↓) cycles, for the alloys with boron content, x = 0, x = 0.5 and x = 1.0 showing structural and magnetic transitions for B-0, B-0.5 and B-1.0 alloys, respectively. The characteristic temperatures of the martensitic transformation are indicated as M_s, M_f, A_s and A_f in the figure for B-1.0 alloy, as a typical example. (b) Variation of martensitic transformation temperature (T_M) and Curie temperature (T_C) with boron content.

Thermal hysteresis has been observed in the martensitic transformation in all the samples indicating the first order nature of the associated structural transformation. It is evident from the Fig. 4.1(a) that all the three alloys under

study are in martensitic state at RT. The martensitic transformation temperature $\{T_M = (M_s+M_f+A_s+A_f)/4\}$ reduced considerably with addition of boron from 347.6 to 320.1 K for B-0.5 and to 314.4 K for B-1.0 alloy. The observed decreasing trend of T_M in this system differs from that observed in Ni-Mn-Sn-B system [23] where T_M increases with interstitial boron content.

The Curie temperature T_C, was determined at the inflection point of the sharp change in susceptibility as indicated in the Fig. 4.1(a). T_C has shown marginal increase from 351 K to 354 K and 360 K for B-0, B-0.5 and B-1.0 alloys respectively. The variation of T_M and T_C with boron addition is shown in Fig. 4.1(b).

Table 4.1. Compositions determined from EDS along with structural and magnetic transition temperatures determined from ac susceptibility measurements.

Boron (at.%)	Sample code	Composition from EDS (at.%)			Transformation temperatures (K)					Curie Temp. T_C (K)
					M_s	M_f	T_M	A_s	A_s	
0	B-0	53.5	26.2	20.3	349	344.6	347.6	346.5	350.2	351.4
0.5	B-0.5	53.4	26.2	20.4	320.6	316.2	320.1	319.5	324.2	354
1.0	B-1.0	53.2	26.4	20.4	314	311	314.4	314.4	318	360

4.3 Crystal structure

4.3.1 X-ray diffraction studies

The powder X-ray diffraction (XRD) patterns of the $Ni_{53.5}Mn_{26.0}Ga_{20.5}B_x$ alloys recorded in the martensitic state at ambient temperature are shown in Fig. 4.2. The diffraction patterns are quite complex, due to the presence of additional peaks associated with structural modulation. The XRD patterns of alloys B-0 and B-0.5 are quite similar while that of B-1.0 alloy shows noticeable deviation. In order to ascertain the type of modulation present in the alloys, selected area electron diffraction (SAED) patterns were recorded for the B-0 and B-1.0 alloys.

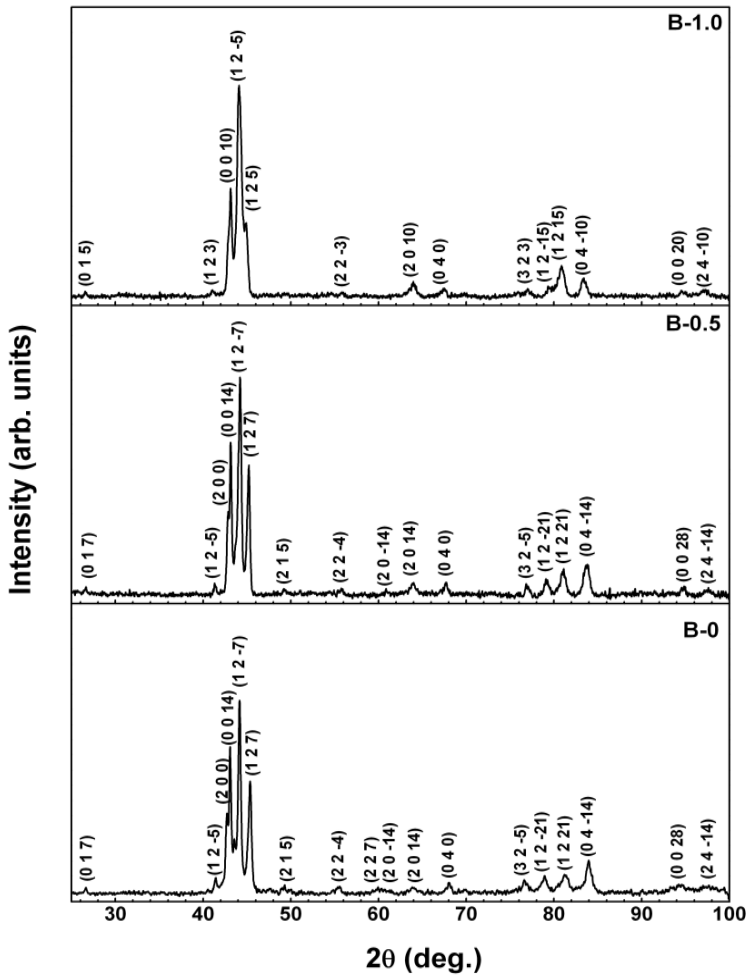

Fig. 4.2. Powder X-ray diffraction patterns recorded at ambient temperature. Based on the results from SAED patterns (shown in Fig. 4.3) XRD patterns are all indexed to monoclinic structure. Superstructural ordering of the B-0 and B-0.5 alloys is of 7M, while that of B-1.0 alloy is of 5M lattice modulation.

4.3.2 TEM investigations using SAED pattern

Fig. 4.3(a) shows the TEM-bright field image of B-0 sample at RT and Fig. 4.3(b) shows the corresponding SAED pattern recorded along the [010] zone axis. The monoclinic angle β is determined to be 92.91(3)^{o} with modulation along the *c*-axis. The six additional spots observed between the two bright spots are indicative of 7 layered lattice modulation.

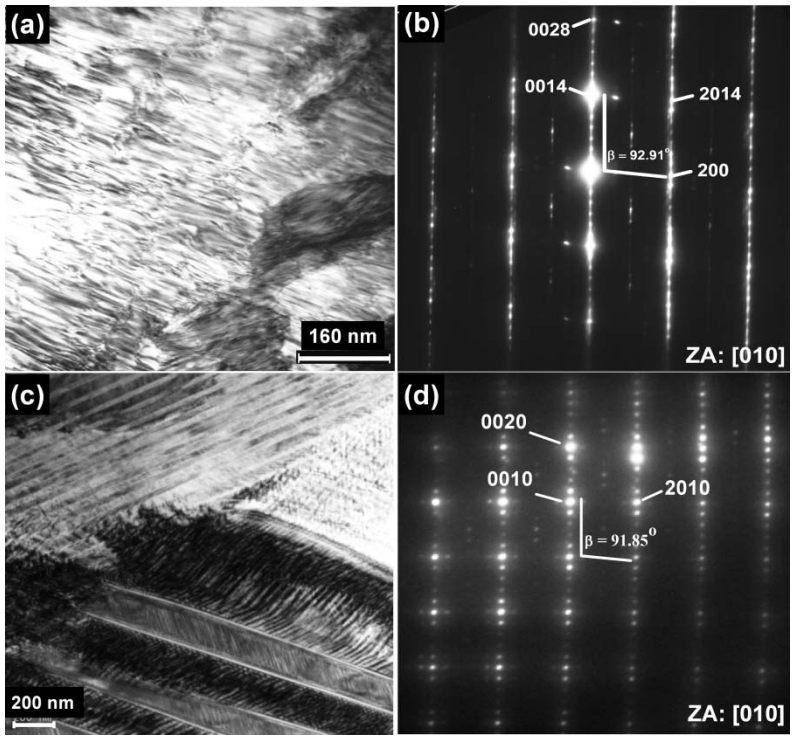

Fig. 4.3. Bright field image and the corresponding SAED patterns are shown in (a) and (b) for B-0 alloy and in (c) and (d) for B-1.0 alloy, respectively. It is evident that both the alloys exhibit monoclinic structure with β > 90°. The additional spots between the two bright spots confirm 7 layered lattice modulation for B-0 and 5 layered modulation for B-1.0 alloys.

Fig. 4.3(c) shows the bright field image in B-1.0 sample and (d) presents the corresponding SAED pattern recorded along the [010] zone axis at RT. 5 layered modulation along the *c*-axis and a monoclinic angle β of 91.85 (1)° are determined for B-1.0 alloy from Fig. 4.3(d). These observations show that the monoclinic structure is retained even on addition of 1 at.% boron but the type of modulation has changed from 7 M to 5 M.

Following the observations from SAED, XRD patterns are indexed as given in Fig. 4.2. The indexing confirms that the present alloys are formed of single phase. Superstructure lines arising from lattice modulation are evident in the figure. The lattice parameters and the monoclinic angle β computed for the alloys using X'pert software are listed in Table 4.2.

Table 4.2. Lattice parameters determined at RT from the SAED and XRD patterns recorded for $Ni_{53.5}Mn_{26.0}Ga_{20.5}B_x$ alloys.

Sample code	Lattice parameters			Monoclinic angle	Modulation
	a (Å)	b (Å)	c (Å)	β(°)	
B-0	4.243 (1)	5.520(1)	29.476 (5)	92.91 (3)	7M
B-0.5	4.238 (1)	5.538 (1)	29.389 (2)	92.58 (2)	7M
B-1.0	4.248 (1)	5.565 (5)	20.978 (1)	91.85 (1)	5M

4.4 Microstructural properties

We discuss below the modifications caused by boron addition to B-0 alloy, in the microstructures. Figs. 4.4 (a) – (c) show the optical microstructures recorded in all the three samples at RT. The microstructures reveal self accommodation of several twinning modes with predominance of crossing twins. Long range twin deformation is prominent in both B-0 and B-0.5 alloys which also exhibit parallel bands, twins within twins unlike in the B-1.0 alloy. Clear formation of fourfold corners due to the crossing twins can be seen (marked as P) in Fig. 4.4 (a). All the twin boundaries can be seen to be sharp and straight all the way to the corners. Formation of multimode twinning minimizes the accumulated elastic strain through structural transformation and is indicative of low residual stresses in the martensitic phase. These are known to form when transformation occurs from high symmetry cubic austenite to low symmetry monoclinic martensite [27, 28]. The widths of the martensitic twin variants are observed to decrease from an average value of 8 μm for B-0 to nearly 1 μm for B-1.0 alloy.

In Ni_3Al and Ni-Ti-Pd alloys [18, 7], it is reported that boron acts as a good grain refiner. In order to observe if boron promotes grain refinement in the present alloys, the samples were polished to quarter micron level and were etched, then were re-polished mildly to observe the grain boundaries, under FESEM.

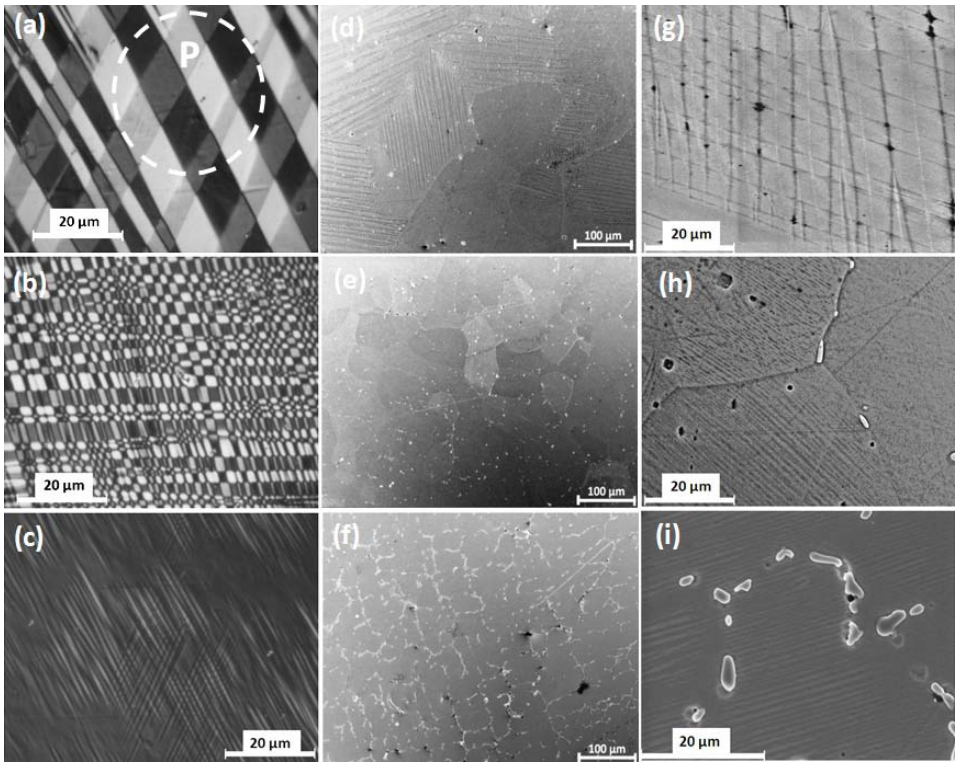

Fig. 4.4. (a) – (c) Optical microstructures recorded at RT for B-0, B-0.5 and B-1.0 alloys, showing that twin widths reduce from (a) 4-10 µm, (b) 2-4 µm and (c) 1-2 µm on boron addition. (d) – (f) FESEM micrographs at low (500x) magnification showing the grain refinement and segregation of second phase caused by boron. (g) –(i) FESEM micrographs at higher (5000x) magnification showing increased volume fraction of second phase segregation at grain boundaries with boron content.

Figs. 4.4 (d) – (f) show the FESEM micrographs recorded at low magnifications. From the figures it can be seen that the grains were refined from a size range of 100 – 200 µm for B-0 to 40-60 µm in B-0.5 and 10 – 30 µm in B-1.0. Additionally, boron has caused the segregation of a second phase at the grain boundaries, the amount of which increased with boron content as is evident from Figs. 4.4 (e) and (f).

Figs. 4.4 (g) – (i) show FESEM micrographs recorded at higher magnification in all the samples which clearly show the presence of the second phase at the grain boundaries. Detailed compositional analysis was carried out using the EDS facility on FESEM, both in the matrix as well as in the second phase.

The results reveal that the second phase regions in the boron containing samples in Figs. 4.4 (h) and (i) are richer in Ni and poorer in Ga compared to the bulk compositions of the alloys listed in Table 4.1. The composition of the matrix measured in several regions (of 10 x 10 sq. μm frame areas) shows a reduction in the Ni content on an average, compared to the bulk value. Similar compositional shifts in the matrix phase of Ni_3Al were reported due to segregation of boron at the grain boundaries, which was detected from ion probe studies [18]. Table 4.3 compares the compositions thus determined for the matrix and the second phase with the bulk compositions for all the alloys.

Table 4.3. Comparison of the bulk compositions (determined from EDS in large frame area) with compositions measured locally in the matrix and in the second phase regions (using EDS in small frame areas) in $Ni_{53.5}Mn_{26.0}Ga_{20.5}B_x$ alloys.

Sample code	Bulk composition	Composition of matrix (10 x 10 sq. μm frame) (at.%)			Composition of second phase (2 x 3 sq. μm frame) (at.%)			*e/a* of matrix phase
		Ni	Mn	Ga	Ni	Mn	Ga	
B-0	$Ni_{53.5}Mn_{26.2}Ga_{20.3}$	53.3	26.3	20.4	---	---	---	7.78
B-0.5	$Ni_{53.4}Mn_{26.2}Ga_{20.4}$	52.1	26.7	21.2	66.7	23.6	9.7	7.72
B-1.0	$Ni_{53.2}Mn_{26.4}Ga_{20.4}$	51.6	27.3	21.1	67.2	24.3	8.4	7.72

The above results provide evidence that some of the Ni atoms from the matrix are utilized to form the Ni-rich second phase (probably containing boron) at the grain boundaries, rendering the matrix Ni- deficient. Though the effect of boron is very obvious from the microstructures, boron could not be detected directly employing EDS, or even wavelength dispersive spectroscopy (WDS) with higher resolution, in the matrix or in the second phase. This could be because boron is a light element and only small amounts of boron are present in the samples. The observed reduction in T_M with B content can be attributed to the compositional shift of the matrix phase.

4.5 Conclusions

Studies on $Ni_{53.5}Mn_{26.0}Ga_{20.5}B_x$ (x = 0, 0.5 and 1.0) alloys reveal that boron addition has not altered the monoclinic crystal structure of the x = 0 composition with increasing boron content, but has altered the superstructural ordering from 7M to 5M when 1 at.% boron is added.

Boron addition to $Ni_{53.5}Mn_{26.0}Ga_{20.5}$ alloy is found to alter the microstructure of the parent alloy by decreasing the martensitic twin widths substantially. Multimode twinning is retained in B-0.5 alloy and is suppressed in B-1.0 alloy. Grain size is refined and the volume fraction of second phase is found to increase with boron content.

Addition of boron had caused a considerable reduction in the martensitic transformation temperature and a marginal increase in the Curie temperature. Reduction in T_M with boron content is attributed to the compositional shift of the matrix phase.

References

[1] K. Aoki and Izumi, *Nippon Kinzoku Gakkaishi* **43** (1979) 1190.

[2] C.T. Liu, C.L. White and J.A. Horton, *Acta Mater.* **33** (1985) 213.

[3] M.A. Morris, *Scripta Mett. Mater.* **25** (1991) 2541.

[4] M.A. Morris, *Acta Mater.* **39** (1991) 1573.

[5] S.M. Tuominen and R.J. Biermann, *J. Met.* **40** (2) (1988) 32.

[6] W.S. Yang and D.E. Mikkola, *Scripta. Mett. Mater.* **28** (1993) 161.

[7] Y. Suzuki, Ya Xu, S. Morito, K. Otsuka and K. Mitose, *Mater. Lett.* **36** (1998) 85.

[8] V.A. Chernenko, E. Cesari, V.V. Kokorin and I.N. Vitenko, *Scripta Metall. Mater.* **33** (1995) 1239.

[9] N. Lanska, O. Söderberg, A. Sozinov, Y. Ge, K. Ullakko and V.K. Lindroos, *J. Appl. Phys.* **95** (2004) 8074.

[10] V.V. Khovaylo, V.D. Buchelnikov, R. Kainuma, V.V. Koledov, M. Ohtsuka, V.G. Shavrov, T. Takagi, S.V. Taskaev and A.N. Vasiliev, *Phys. Rev. B* **72** (2005) 224408.

[11] I. Glavatskyy, N. Glavatska, O. Soderberg, S-P. Hannula and J-H. Hoffmann, *Scripta Mater.* **54** (2006) 1891.

[12] D.Y. Cong, S. Wang, Y. D. Wang, Y. Ren, L. Zuo and C. Esling, *Mater. Sci. Eng. A* **473** (2008) 213.

[13] A. Satish Kumar, M. Ramudu and V. Seshubai, *J. Alloys Compd.* **509** (2011) 8215.

[14] D. Kikuchi, T. Kanomata, Y. Yamaguchi, H. Nishihara, K. Koyama and K. Watanabe, *J. Alloys Compd.* **383** (2004) 184.

[15] D. Kikuchi, T. Kanomata, Y. Yamaguchi and H. Nishihara, *J. Alloys Compd.* **426** (2006) 223.

[16] D.E. Soto-Parra, F. Alvarado-Hernandez, O. Ayala, R.A. Ochoa-Gamboa, H. Flores-Zúñiga and D. Rios-Jara, *J. Alloys Compd.* **464** (2008) 288.

[17] K. Tsuchiya, A. Tsutsumi, H. Ohtsuka and M. Umemoto, *Mater. Sci. Eng. A* **378** (2004) 370.

[18] L. Hui, L. Xiang, G. Jianting and H.U. Zhuangqi, *Acta Metall. Sinica* **2** (1989) 256.

[19] I. Sen, S. Tamirisakandala, D.B. Miracle and U. Ramamurthy, *Acta Mater.* **55** (2007) 4983.

[20] B.R. Gautam, I. Dubenko, A.K. Pathak, S. Stadler and N. Ali, *J. Mag. Mag. Mater.* **321** (2009) 29.

[21] B.R. Gautam, I. Dubenko, A.K. Pathak, S. Stadler and N. Ali, *J. Phys.: Condens. Matter* **20** (2008) 465209.

[22] H. Luo, F. Meng, Q. Jiang, H. Liu, E. Liu, G. Wu and Y. Wang, *Scripta Mater.* **63** (2010) 569-572.

[23] H.C. Xuan, D.H. Wang, C.L. Chang, Z.D. Han, B.X. Gu and Y.W. Du, *Appl. Phys. Lett.* **92** (2008) 102503.

[24] T.K. Chaki, *Mater. Sci. Eng. A* **190** (1995) 109.

[25] Y.S. Han and Y.G. Kim, *Scripta Mater.* **21** (1987) 947.

[26] M. Ramudu, A. Satish Kumar, V. Seshubai, K. Muraleedharan, K.S. Prasad and T. Rajasekharan, *Scripta Mater.* **63** (2010) 1073.

[27] M. Nishida, H. Ohgi, I. Itai, A. Chiba and K. Yamauchi, *Acta Metall. Mater.* **43** (1995) 1219.

[28] K. Bhattacharya, *Microstructure of Martensite* (Oxford University Press, Oxford, 2003), p. 83.

Chapter 5

Effect of boron addition on the magnetic and mechanical properties of $Ni_{53.5}Mn_{26.0}Ga_{20.5}$ alloy

5.1 Introduction

Compositional changes not only alter the transformation temperatures of Ni-Mn-Ga alloys, but have a significant effect on the magnetic and mechanical properties of these materials through microstructural modifications. As discussed in Chapter 4, introduction of boron is known to be very effective in improving room temperature ductility of Ni_3Al [1, 2] through segregation of boron containing phase at grain boundaries. Boron was also used to improve room temperature ductility of Cu-Al-Ni [3, 4] shape memory alloys. Grain size refinement as well as grain boundary strengthening was reported in Cu-Zn-Al [5] on boron doping. The effect of boron addition on the microstructural and mechanical properties of Ti-Pd-Ni alloys has been reported by several groups [6-8]. Precipitates of TiB_2 were observed within the grains, rather than at grain boundaries. Grain refinement was attributed to be due to a reduction in the rate of grain growth due to boron during annealing. Boron was found to increase the tensile strength but the shape memory properties were not affected.

In the case of Ni-Mn-Ga alloys, there has been growing interest in investigating the effect of boron, as well as other elements like Co, Fe, Ti and rare earth elements like Sm, Dy, Y, Nd, Tb, and Gd, on the properties of the chosen parent alloy [9-18]. Co substitution in $Ni_{56}Mn_{25-y}Co_yGa_{19}$ (y = 4 and 8) and $Ni_{56-z/2}Mn_{25-z/2}Co_zGa_{19}$ (z = 4 and 6) [9] caused γ phase precipitation leading to significant improvement in ductility, but a suppression of shape memory effect. Fe in $Ni_{48.7}Mn_{30.1-x}Fe_xGa_{21.2}$ (x = 0-11) [19] has been reported to enhance fracture toughness and grain boundary strength due to second phase segregation at the

grain boundaries. Improved compression strength and ductility through substitution of Yttrium [20] and increase in bending strength by Gd substitution [21] in $Ni_{50}Mn_{29}Ga_{21}$ alloy have been reported. This improvement in mechanical properties is attributed to grain refinement, and grain boundary strengthening due to second phase segregation. However, shape memory properties have not been reported in these systems. Since boron has a tendency to cause second phase segregation, it is interesting to study the influence of boron on the mechanical behavior of Ni-Mn-Ga alloys, which has not been explored in literature.

Recent studies on the effect of boron substituted for Mn and Ga on the structural and magnetic properties of $Ni_2Mn_{1-x}B_xGa$ [22] and $Ni_2MnGa_{1-x}B_x$ [23] have been reported. In the former system, both T_M and the Curie temperature (T_C) are found to decrease with B content. Saturation magnetization has shown a reduction of 50% (for x = 0.3) at 5 K and is attributed to be a result of replacing magnetic Mn atom by non-magnetic boron atom. Substitution of B for Ga in the latter system is found to decrease the saturation magnetization by 20% at 5 K for the alloy with x = 0.25 and is attributed to a decrease in the lattice parameters causing a reduction in Mn-Mn distance. Increase in T_M and a marginal reduction in T_C is seen with B content. The alloys of the above systems are all in the austenitic phase at RT and hence are not suitable for applications at RT. In $Ni_{50}Mn_{36.5}Sb_{13.5-x}B_x$ system [24] it is observed that saturation magnetization decreases monotonously with boron content which is attributed to the smaller atomic radius of B atom compared to that of Sb, which shortens the distance between the Mn atoms and enhances the antiferromagnetic coupling between them. The reduction in T_M discussed above on substitution of B for Mn in $Ni_2Mn_{1-x}B_xGa$ system follows the general trend reported in literature that T_M increases with an increase in electron concentration (e/a). However, increase in T_M observed in the other two systems where B is substituted for Ga or Sb could not be explained on similar lines.

In this chapter, we present the results from the investigations on the mechanical and magnetic properties of $Ni_{53.5}Mn_{26.0}Ga_{20.5}B_x$ alloys, derived from B-

0 alloy, which was discussed in detail in Chapter 3. This alloy exhibits a large shape memory effect of 1.8%, which was correlated to the multi-mode twinning in the monoclinic martensitic phase, but the compressive strength was only about 120 MPa. Results from systematic investigations on the mechanical properties like Vickers microhardness, compressive stress-strain and shape memory behavior and also the magnetic properties of boron containing alloys derived from $Ni_{53.5}Mn_{26.0}Ga_{20.5}B_x$ are presented in this chapter. Various results are analyzed in correlation to the microstructural features of these alloys, discussed in Chapter 4. An attempt has been made to correlate the observed results to the microstructural modifications brought about by boron.

5.2 Magnetic properties

Magnetic isotherms were recorded using Physical Property Measurement System (PPMS), of Quatum Design make, in the temperature range 5 K to 370 K and for fields up to 3 T. The saturation magnetization (M_{sat}) as well as the magnetic anisotropy constant (K_1) were determined from each of the isotherms, employing the approach to saturation method [25].

5.2.1 Saturation magnetization

Fig. 5.1 shows typical isotherms obtained at 5 K for the three compositions studied. The temperature dependences of saturation magnetization (M_{sat}) for all the samples are shown in Fig. 5.2. The saturation magnetization M_{sat} at 5 K increases with boron content from nearly 66.5 emu/g for B-0 alloy to 79.1 emu/g for B-1.0 alloy which corresponds to a change from 2.86 to 3.40 in units of μ_B per formula unit (μ_B/f.u.), and is quite a significant rise. From Fig. 5.2, a systematic increase with addition of boron can be seen in M_{sat} in the temperature range 5 K to 250 K, beyond which T_M of the samples is approached.

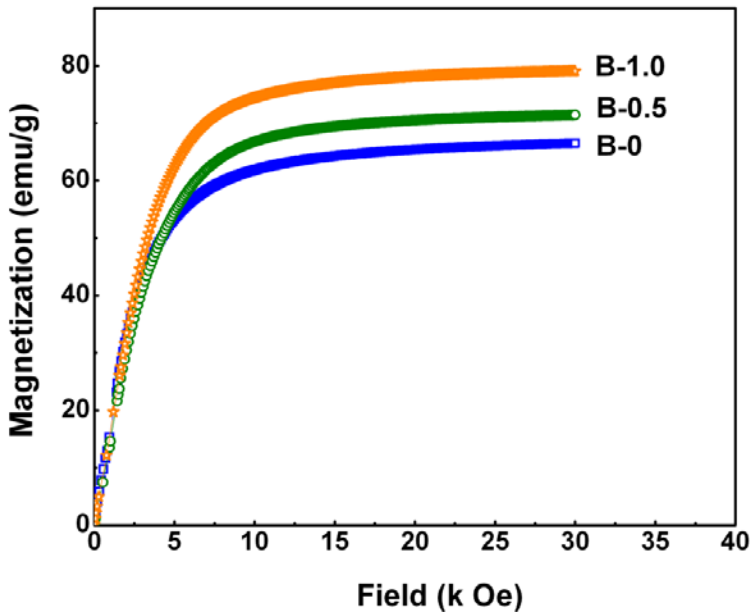

Fig. 5.1. Magnetic isotherms recorded at 5 K for $Ni_{53.5}Mn_{26.0}Ga_{20.5}B_x$ alloys up to a magnetic field of 3 T. A significant increase in M_{sat} can be observed on boron addition.

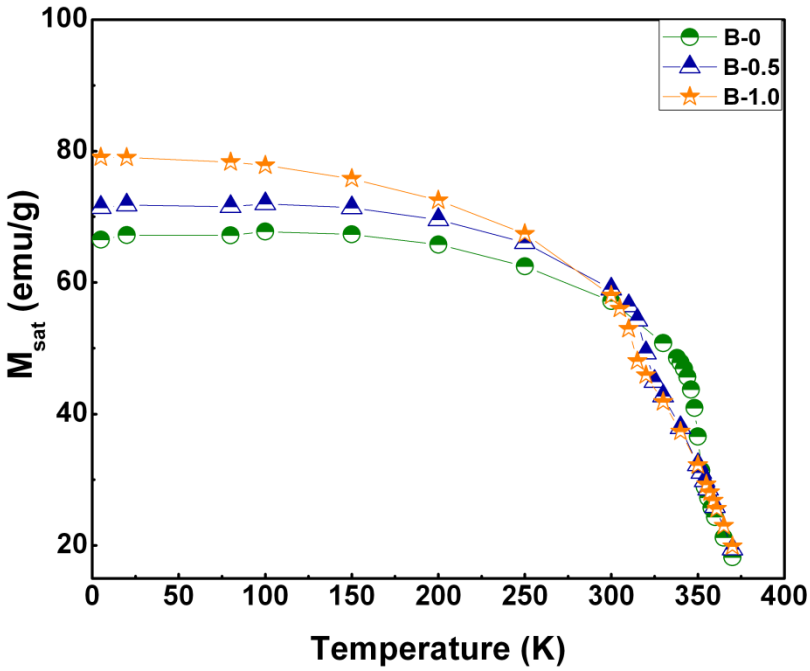

Fig. 5.2. Temperature dependence of saturation magnetization (M_{sat}) determined from isotherms recorded at various temperatures for the alloys B-0, B-0.5 and B-1.0. Increase in M_{sat} on boron addition is evident in the temperature range (nearly 5-250 K), below T_M.

5.2.2 Magnetic anisotropy constant

Fig. 5.3 shows the temperature dependence of K_1 with boron content. It can be seen that K_1 falls rapidly at T_M in the alloys B-0.5 and B-1.0 where the martensitic transformation occurs much below T_C, indicating that the magnetic anisotropy of the austenitic phase is much less compared to that of the martensitic phase.

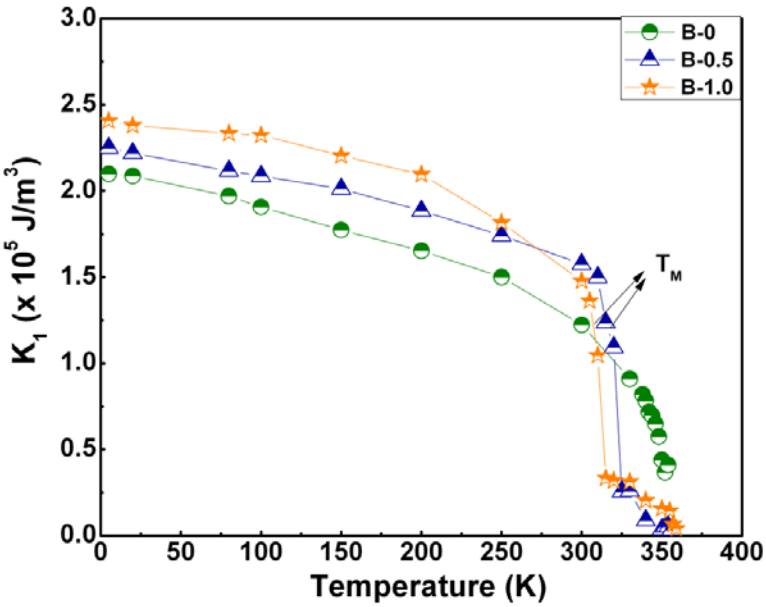

Fig. 5.3. Temperature dependence of magnetic anisotropy constant (K_1) for the alloys B-0, B-0.5 and B-1.0, which is calculated from the corresponding isotherms. It can be seen that K_1 exhibits a sharp reduction at T_M (while heating) due to the anisotropy difference between martensite and austenite phases.

Such a rapid fall in K_1 is not seen in B-0 alloy, which exhibits magneto-structural transformation. It is interesting to note that the addition of boron in Ni-Mn-Ga system has substantially influenced the magnetic properties at 5 K, though boron has no magnetic moment.

5.3 Effect of boron addition on the magnetic moments

We examine below the possible reasons for a considerable rise in M_{sat} on addition of boron. In ferromagnetic shape memory alloys of Ni_2MnX (X = Ga, Sn,

Sb), the major contribution to M_{sat} comes from the magnetic moments, localized on the Mn atoms, ranging from 2.84 to 4.2 μ_B while Ni atoms possess a small moment of 0.2 to 0.4 μ_B [26-31].

In the case of off-stoichiometric Ni- rich compositions of Ni-Mn-Ga, Richard *et al.* [32] have shown that for Ni concentration of 50 at.% or more, the excess Ni displaces the Mn atoms from their regular sites (in Mn sublattice) and couple ferromagnetically with Mn moments. The excess Mn and the displaced Mn atoms occupy vacant Ga sites and couple antiferromagnetically to the Mn at regular sites. Jie *et al.* [33], from Density Functional Theory (DFT) calculations supported this view based on the preference for the smaller lattice distortions and lower-energy electronic structure. The schematic representation of magnetic moments in stoichiometric as well as off-stoichiometric Ni-Mn-Ga is shown in Figs. 5.4 (a) and (b).

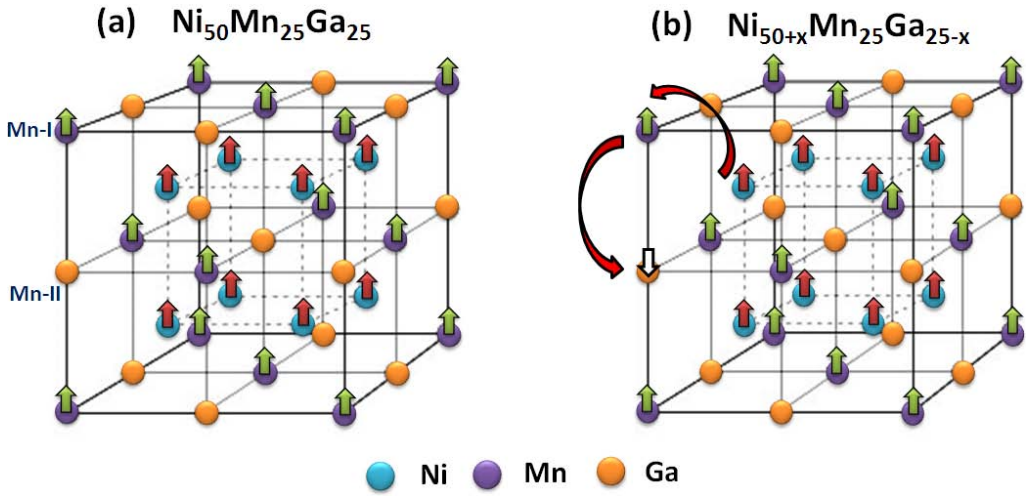

Fig. 5.4. Schematic representation of arrangement of magnetic order in the case of (a) stoichiometric $Ni_{50}Mn_{25}Ga_{25}$ and (b) off-stoichiometric Ni-excess $Ni_{50+x}Mn_{25}Ga_{25-x}$ alloys.

Following this approach, the experimentally observed magnetic moment of 2.86 μ_B/f.u. for the parent alloy (B-0), can be accounted for by considering that at 5 K, there exists a magnetic moment of 3.20 μ_B on Mn and 0.33 μ_B on Ni atoms respectively.

We present below the method adopted for the calculation of magnetic moment per formula unit, μ_{cal} in μ_B/f.u. typically for B-0 composition.

μ_{Cal} (μ_B/f.u.) = (4/100) [(at.% of Ni in Ni sublattice)$_{FM}$ *μ_{Ni} + (at.% of Mn in Mn sublattice)$_{FM}$*μ_{Mn} + (at.% of Ni in Mn sublattice)$_{FM}$* μ_{Ni} – (at.% of Mn in Ga sublattice)$_{AFM}$ *μ_{Mn}

= (4/100) [(50*0.33)$_{FM}$ + (21.5*3.20)$_{FM}$ + (3.5*0.33)$_{FM}$ – (4.7*3.20)$_{AFM}$

= **2.86** μ_B/f.u.

Here the subscripts FM and AFM on (at.% of X in Y sublattice) term refer to ferromagnetic and anti-ferromagnetic order assumed for the moments on element X (X = Ni, Mn) with respect to the moments in Ni and Mn sublattices.

The μ_{cal} values estimated using the above approach, for the alloys B-0.5 and B-1.0, based on the EDS compositions, work out to be 2.89 and 2.90 μ_B/f.u. which deviate considerably from the experimentally observed values of 3.07 and 3.40 μ_B/f.u. This is surprising because the compositions determined from EDS are nearly the same for all the three alloys but for the presence of boron, which has no magnetic moment. The enhancement in the measured values of magnetization, on addition of 1 at.% boron, from 2.86 to 3.40 μ_B/f.u. amounts to ~19 % rise per formula unit.

The observed large increase in the M_{sat} value on addition of boron can be explained if boron forms bonds with Ni or Mn atoms causing a compositional shift of the matrix phase. Ni-B bonds are known to form at the grain boundaries in Ni_3Al [34-37] thus modifying the mechanical properties. Formation of Mn-B bonds leading to observation of secondary Mn_2B phase is reported in Ni-Mn-Sn-B system at high B contents [38]. In order to ascertain the possibility of secondary phase segregation in the present samples, detailed microstructural studies were carried out using FESEM. These details were discussed in section 4.3 of Chapter 4. The

relevant results are reproduced below to facilitate a discussion. Figs. 5.5 (a), (c) and (e) show the micrographs recorded at low magnification in samples B-0, B-0.5 and B-1.0 and (b), (d) and (f) shows the images at higher magnification.

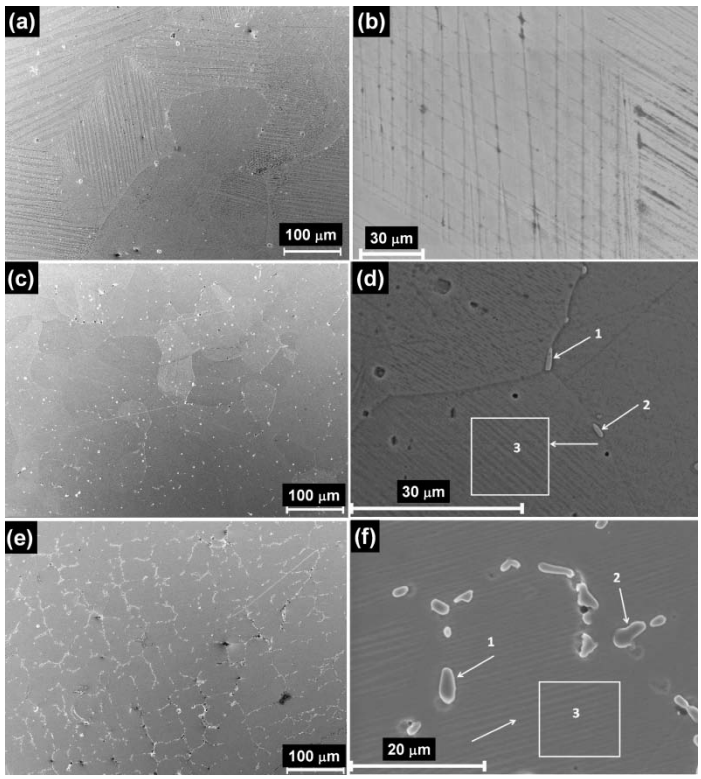

Fig. 5.5. The micrographs recorded using FESEM at lower and higher magnifications (shown in Fig. 4.4) for B-0, B-0.5 and B-1.0 alloys are reproduced here. A comparison of (e) & (f) with (c) & (d) reveals that considerable increase in grain boundary segregation occurs with boron content. No such segregation is seen in (a) and (b) for B-0 alloy. Typically, 1 and 2 indicate regions of second phase while 3 indicates a region in the matrix, chosen for compositional analysis.

The figure shows that the second phase, whose amount increases with boron content, segregates at the grain boundaries. The compositional analysis carried out, using EDS facility on FESEM, in the secondary phase regions identified it to be a Ni-Mn phase, richer in Ni compared to the average composition of the alloys determined from EDS and listed in Table 4.3 of Chapter 4. Accordingly, the composition of the matrix shows a reduction in the Ni content compared to the bulk composition. These results provide evidence that boron promotes formation

of a Ni-rich phase at grain boundaries rendering the matrix deficient in Ni. Similar compositional shifts were observed in Ti-Pd-Ni alloys due to boron addition [8].

The volume fraction of the secondary phase is estimated from the micrographs to be 0.4% and 3.1% respectively for B-0.5 and B-1.0 alloys. Presence of only relatively small amounts of the secondary phase explains the absence of corresponding Bragg peaks in XRD patterns of boron containing alloys.

We now examine the relevance of the compositional shift of the majority matrix phase on the magnetic properties of the alloys under study. A reduction in the Ni content from 53.3 at.% in the matrix of the B-0 alloy to 52.1 in the B-0.5 and 51.6 in B-1.0 alloys is expected to modify the net magnetic moments per unit cell. The excess Ni atoms (when > 50 at.% is present) are known to displace Mn atoms at regular Mn sites to Ga sites [32]. The Mn moments at Ga site assume antiferromagnetic order with respect to those of Mn at regular sites. Hence a reduction in the excess Ni content in the matrix would imply a decrease in the number of Mn atoms displaced to Ga site with antiferromagnetic order. This would result in an effective increase in magnetization per unit cell and thus explain qualitatively the rise in M_{sat} value observed experimentally on boron addition.

5.4 Mechanical properties

5.4.1 Loading curves: Compressive stress-strain

Fig. 5.6 (a) - (c) show the stress-strain curves recorded under compression in all the alloys at RT. In order to investigate the effect of boron on shape memory effect at RT, the loading and unloading curves were recorded on all the samples. Maximum compression strengths of 124 MPa, 198 MPa and 111 MPa and corresponding compression strains of 5.2 %, 4.3 % and 5.5 % respectively have been recorded for B-0, B-0.5 and B-1.0 alloys. The stress-strain curve shows a linear elastic region followed by near-plateau region. The linear elastic region terminating at 12 MPa (indicated by a slope change) in B-0 alloy corresponds to the critical stress beyond which martensitic re-orientation occurs. The near-

plateau region with continuous increase of strain with stress indicates that the re-orientation of multivariant martensites occurs over a broad range of stresses in the polycrystalline samples (having many grain boundaries), unlike in single crystals. Expansion of the variants, oriented favorably with respect to the applied stress, occurs during this detwinning process.

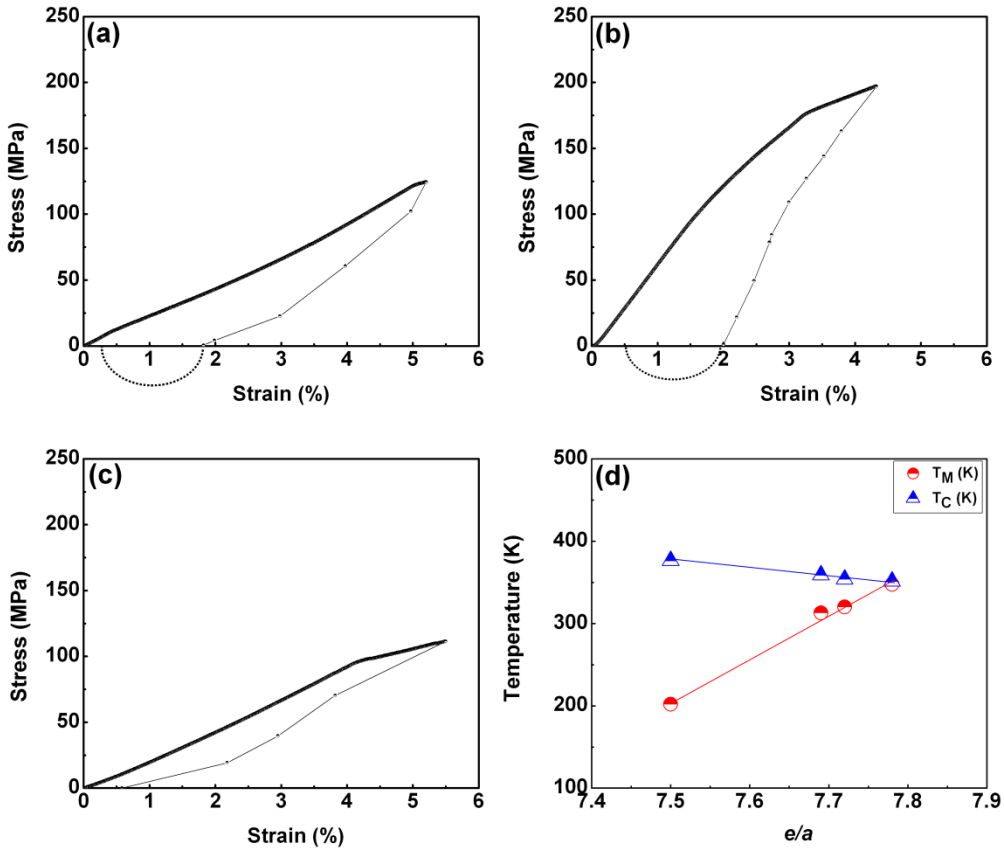

Fig. 5.6. (a)-(c) Compressive stress-strain curves recorded at RT in B-0, B-0.5 and B-1.0 alloys, respectively. The strain recovery on heating the samples to 150 °C after unloading is indicated as dashed line. (d) shows that the general trend of variation in T_M and T_C on e/a is followed, when e/a is computed using composition of the matrix phase. T_M and T_C of Ni_2MnGa are also included in the plot.

From EBSD studies reported in polycrystalline Ni-Mn-Ga alloys under compression, Chulist *et al.* [39] have confirmed that most of the compressive strain is due to motion of twin boundaries within the grains and that the grain boundaries indeed impede twin boundary motion preventing a complete

reorientation close to the grain boundaries. In other words, grain boundaries acts as a barrier for twin boundary motion and hence more stress is required to extend the detwinned region closer to the grain boundaries. This has been reflected in the case of B-0.5 alloy in which the number of grain boundaries has increased causing higher compression stress to be required for a given strain, compared to B-0 alloy. In the case of B-1.0 alloy, the grain size has decreased further to 10-30 μm of the martensitic twins have become finer. However, it can be noticed that substantial deformation occurs in B-1.0 even at low stresses, in spite of reduced grain size. In other words, the range of critical stress required for re-orientation is lowered in B-1.0 alloy, compared to B-0.5, giving rise to easy deformation to higher compressive strain at lower stresses. These observations suggest that hindrance to detwinning due to grain boundaries is not effective in B-1.0 alloy. In this context, one needs to consider the role of second phase segregation at the grain boundaries. Similar enhancement in compressive ductility was observed in Fe- and rare-earth doped $Ni_{50}Mn_{30}Ga_{20}$ alloy which was attributed to large amount of precipitation of second phase at the grain boundaries [40]. Also in the case of Ni_3Al, boron segregation is found to improve ductility [41].

5.4.2 Unloading curves and Shape memory effect

After subjecting the samples to high compression strength, the loading was slowly withdrawn. Substantial residual strains (ε_{res}) of 1.8% and 2.0% for B-0 and B-0.5 alloys were observed after unloading. For B-1.0 alloy ε_{res} was only 0.4%. The samples are then heated to 150 ^{o}C (much above the martensitic temperatures) and are cooled to RT to assess the shape memory effect. The residual irreversible strains (ε_P) after heating the samples are given in Table 5.1. The shape memory strain (ε_{SME}), is calculated as

$$\varepsilon_{SME} = \left(\varepsilon_{res} - \varepsilon_P\right)$$

The strain recovery ratios (R) are calculated using the formula

$$R = \left(\frac{\varepsilon_{res} - \varepsilon_P}{\varepsilon_{res}} \right) X 100$$

and all these parameters are presented in Table 5.1.

Table 5.1 Shape memory strain and shape recovery ratios for $Ni_{53.5}Mn_{26.0}Ga_{20.5}$ B_x (x = 0, 0.5 and 1) alloys, as determined from the compressive stress-strain measurements.

Sample code	Residual Strain (ε_{res}) (%)	Permanent strain (ε_P) (%)	Shape memory strain (ε_{SME}) (%)	Shape recovery ratio (R) (%)	Volume fraction of second phase (%)
B-0	1.8	0.2	1.6	89	0
B-0.5	2.0	0.5	1.5	75	0.4
B-1.0	0.4	0	0.4	---	3.1

Considerable shape memory effect is observed in both B-0 and B-0.5 alloys which showed long range twin deformation (Figs. 5.6 (a) and (b)). SME of close to 1.5% observed in B-0 alloy was retained even after an addition of 0.5 at.% boron. This was not affected by small amounts of second phase segregation at grain boundaries. In the case of B-1.0 alloy, though the deformation during detwinning was larger and occurred at lower stresses compared to B-0.5, the SME was reduced to 0.4%. This probably has an origin in the lower T_M of the matrix phase in B-1.0 alloy, which is caused by compositional shift due to considerable second phase segregation. The Ni content decreases from 53.3 at.% in B-0 alloy to 51.6 at.% for B-1.0 alloy, as shown in Table 4.3 of Chapter 4, causing a corresponding reduction in e/a and T_M. Proximity of the T_M of B-1.0 alloy to RT at which SME is measured, may have a role to play in enhanced reversibility of detwinning / martensitic variant re-orientation. Fig. 5.6 (d) depicts the variation of T_M and T_C with e/a. The composition of the matrix phase which is responsible for changes in T_M was taken into account to compute e/a of the matrix. The dependence of T_M and T_C follows the general trend with e/a, expected in Ni-Mn-Ga system. T_M and T_C of stoichiometric Ni_2MnGa [26] are also shown in the plot.

5.5 Microhardness properties

Systematic investigations on the microhardness properties of $Ni_{53.5}Mn_{26.0}Ga_{20.5}B_x$ alloys have been carried out by measuring the hardness at different loads at RT. Figs. 5.7 (a) – (f) illustrate the optical micrographs recorded at ambient temperature under 500 gf and 1000 gf loads (L) respectively on all the samples. At each load, measurements have been done at 8 locations on each sample and an average of the indentation (d) has been determined. The Vickers hardness (HV) has been calculated using the following relation

$$HV = 1854.4 * \frac{L}{d^2} \qquad \text{..... (5.1)}$$

where load (L) is in gram force and the mean of the diagonals (d) is in micrometers. The constant of proportionality depends on the experimental configuration.

Figs. 5.7 (a) and (b) show relief patterns observed around the indentation of the diamond tip on application of 500 gf load. The relief pattern has become more prominent under 1000 gf load. Similar kind of relief patterns have been observed for B-0.5 alloy, with finer twins (Figs. 5.7 (c) and (d)) compared to those in B-0. The widths of these relief patterns appeared to be correlated to the twin widths observed in Figs. 5.7 (a) and (b). No relief pattern appeared for B-1.0 alloy even at higher loads (Figs. 5.7 (e) and (f)). Hardness has been found to increase with boron content. It is well known that hardness, which is associated with dislocation motion, increases with grain refinement [42] and second phase segregation at the grain boundaries [43]. The measured Vickers hardness and the volume fraction of second phase (estimated from EDS and listed in Table 5.1) show similar variation with boron content, as can be seen from Fig. 5.7 (g).

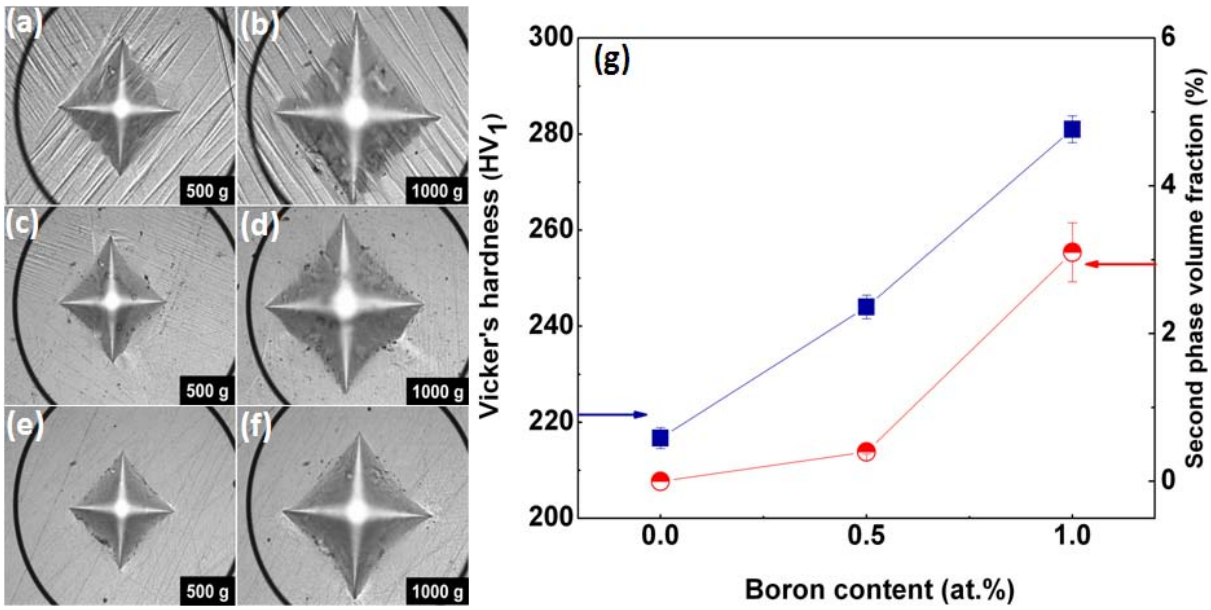

Fig. 5.7. Optical micrographs of the samples after indentation at 500 gf and 1000 gf loads in B-0, B-0.5 and B-1.0 alloys. (a) and (b) show the relief patterns around the indentation in B-0 alloy, (c) and (d) show the relief patterns with finer twins around the indentation in B-0.5 alloy and (e) and (f) show no relief patterns even after application of 1000 gf load in B-1.0 alloy. (g) shows the variation of Vickers microhardness determined on application of 1000 gf load and that of volume fraction of second phase segregation, with boron content.

The hardness value increased from 290 kgf/mm^2 for B-0 alloy to 309 kgf/mm^2 for B-1.0 alloy for 1000 gf load. These hardness values are much higher compared to the values reported for Ni-Mn-Ga alloys in the martensitic phase [44]. From various results presented above, we conclude that B-0.5 alloy with larger compression strength, substantial shape memory effect and higher hardness has a potential for practical applications at room temperature.

5.6 Conclusions

Saturation magnetization measured at low temperatures increased substantially on boron addition. This is explained in terms of the compositional shift in the matrix phase detected from FESEM studies. Ni-rich secondary phase segregation is observed at the grain boundaries rendering the matrix phase deficient in Ni. The starting composition $Ni_{53.5}Mn_{26.0}Ga_{20.5}$ which was rich in Ni in

comparison with Ni_2MnGa has the excess Ni atoms occupying Mn sites. The Mn moments displaced by Ni from its regular site occupies the Ga site antiferromagnetically. When the Ni content in the matrix is lowered due to the formation of Ni-rich second phases, the amount of antiferromagnetically ordered Mn atoms in the Ga site decreases increasing the magnetic moment of the alloy.

Shape memory effect was retained in B-0.5 alloy and was suppressed in B-1.0 alloy. Higher compression stress observed in B-0.5 alloy is attributed to grain refinement. Larger amounts of second phase segregation have led to easy deformation at lower stresses in B-1.0 alloy. Suppression of SME and the enhanced reversibility of detwinning process observed at RT in B-1.0 alloy are attributed to the proximity of T_M to RT. Increase in microhardness with boron content is correlated to the amount of second phase segregation.

References

[1] K. Aoki, Izumi, *Nippon Kinzoku Gakkaishi* **43** (1979) 1190.

[2] C.T. Liu, C.L. White and J.A. Horton, *Acta Mater.* **33** (1985) 213.

[3] M.A. Morris, *Scripta. Mett. Mater.* **25** (1991) 2541.

[4] M.A. Morris, *Acta Mater.* **39** (1991) 1573.

[5] Y.S. Han and Y.G. Kim, *Scripta Mater.* **21** (1987) 947.

[6] S.M. Tuominen and R.J. Biermann, *J. Met.* **40** (2) (1988) 32.

[7] W.S. Yang and D.E. Mikkola, *Scripta. Mett. Mater.* **28** (1993) 161.

[8] Y. Suzuki, Ya Xu, S. Morito, K. Otsuka and K. Mitose, *Mater. Lett.* **36** (1998) 85.

[9] Y. Ma, S. Yang, Y. Liu and X. Liu, *Acta Mater.* **57** (2009) 3232.

[10] A. Satish Kumar, M. Ramudu and V. Seshubai, *J. Alloys Compd.* **509** (2011) 8215.

[11] A.A. Cherechukin, I.E. Dikshtein, D.I. Ermakov, A.V. Glebov, V.V. Koledov, D.A. Kosolapov, V.G. Shavrov, A.A. Tulaikova, E.P. Krasnoperov and T. Takagi, *Phys. Lett. A* **291** (2001) 175.

[12] Y. Q. Ma, L. H. Xu, Y. Li, C. B. Jiang, H. B. Xu and Y. K. Lee, *Z. Metallkd.* **96** (2005) 843.

[13] Y. Xin, Y. Li, L. Chai and H. B. Xu, *Scripta Mater.* **57** (2007) 599.

[14] G. F. Dong, W. Cai, Z. Y. Gao and J. H. Sui. *Scripta Mater.* **58** (2008) 647.

[15] K. Tsuchiya, A. Tsutsumi, H. Ohtsuka and M. Umemoto, *Mater. Sci. Eng. A* **378** (2004) 370.

[16] W. Cai, L. Gao, A. L. Liu, J. H. Sui and Z. Y. Gao, *Scripta Mater.* **57** (2007) 659.

[17] L. Gao, Z. Y. Gao, W. Cai and L. C. Zhao, *Mater. Sci. Eng. A* **438-440** (2006) 1077.

[18] L. Gao, W. Cai, A. L. Liu and L. C. Zhao, *J. Alloys Compd.* **425** (2006) 314.

[19] H. B. Wang, F. Chen, Z. Y. Gao, W. Cai and L. C. Zhao, *Mater. Sci. Eng. A* **438-440** (2006) 990.

[20] J. Sui, X. Zhang, L. Gao and W. Cai, *J. Alloys Compd.* **509** (2011) 8692.

[21] L. Gao, W. Cai, A. L. Liu and L. C. Zhao, *J. Alloys Compd.* **425** (2006) 314.

[22] B.R. Gautam, I. Dubenko, A.K. Pathak, S. Stadler and N. Ali N, *J. Mag. Mag. Mater.* **321**(2009) 29.

[23] B.R. Gautam, I. Dubenko, A. K. Pathak, S. Stadler and N. Ali, *J Phys: Condens Matter* **20** (2008) 465209.

[24] H. Luo, F. Meng, Q. Jiang, H. Liu, E. Liu, G. Wu and Y. Wang, *Scripta Mater*. **63** (2010) 569.

[25] H. Zijlstra, *Experimental Methods in Magnetism* Vol. 2, (1967) p.182-185.

[26] P.J. Webster, K.R.A. Ziebeck, S.L. Town and M.S. Peak, *Phil. Mag. B* **49** (1984) 295.

[27] P.J. Brown, A.Y. Bargawi, J. Crangle, K-U. Neumann and K.R.A. Ziebeck, *J. Phys.: Condens. Matter* **11** (1999) 4715.

[28] P.J. Brown, J. Crangle, T. Kanomata, M. Matsumoto, K-U. Neumann, B. Ouladdiaf and K.R.A. Ziebeck, *J. Phys.: Condens. Matter* **14** (2002) 10159.

[29] V.V. Khovailo, V. Novosad, T. Takagi, D.A. Filippov, R.Z. Levitin and A.N. Vasil'ev, *Phys. Rev. B* **70** (2004) 174413.

[30] C. Jiang, Y. Muhammad, L. Deng, W. Wu and H. Xu, *Acta Mater.* **52** (2004) 2779.

[31] I. Dubenko, M. Khan, A.K. Pathak, B.R. Gautam, S. Stadler and N. Ali, *J. Mag. Mag. Mater.* **321** (2009) 754.

[32] M.L. Richard, J. Feuchtwanger, S.M. Allen, R.C. O'Handley, P. Lázpita, J.M. Barandiaran, J. Gutierrez, B. Ouladdiaf, C. Mondelli, T. Lograsso and D. Schlagel, *Phil. Mag.* **87** (2007) 3437.

[33] C. Jie, L.I. Yan, S. Jia-Xiang and X.U. Hui-Bin, *Chin. Phys. Lett.* **26** (2009) 047101.

[34] L. Hui, L. Xiang, G. Jianting and H.U. Zhuangqi, *Acta Metall. Sinica* **2** (1989) 256.

[35] S . Ghosh Chowdhury, *Phil. Mag. Lett.* **74** (1996) 327.

[36] E.M. Schulson, T.E. Weihs, I. Baker, H.J. Frost and J.A. Horton, *Acta Metall.* **34** (1986) 1395.

[37] T.P. Weihs, V. Zinoviev, D.V. Viens and E.M. Schulson, *Acta Metall.* **35 (**1987) 1109.

[38] H.C. Xuan, D.H. Wang, C.L. Chang, Z.D. Han, B.X. Gu and Y.W. Du, *Appl. Phys. Lett.* **92** (2008) 102503.

[39] R. Chulist, M. Pötschke, T. Lippmann, C-G. Oertel and W. Skrotzki, *J. Phys.: Conference Series* **240** (2010) 012024.

[40] R. K. Singh, M. Manivel Raja, R. P. Mathur and M. Shamsuddin, *J. Alloys Compd.* **506** (2010) 73.

[41] L. I. Hui, L. I. U. Xiang, G. U. O. Jianting and H. U. Zhuangqi, *Acta Mett. Sinica* **2** (1989) 256.

[42] William F. Hosford, *Mechanical Behavior of Materials*, Cambridge University Press (2010).

[43] E. Dogan, I. Karaman, Y.I. Chumlyakov and Z.P. Luo, *Acta Mater.* **59** (2011) 1168.

[44] X. W. Liu, O. Soderberg, K. Koho, N. Lanska, Y. Ge, A. Sozinov and V. K. Lindroos, *Wear* **258** (2005) 1364.

Chapter 6

Correlation of martensitic transformation temperatures of Ni-Mn-Ga/Al-X alloys to non-bonding electron concentration

6.1 Introduction

The study of magnetic shape memory alloys has, of recent, gained momentum due to their potential for applications as sensors and actuators operable at room temperature [1]. Also, their application in magnetic refrigeration is much sought after due to the benefits that could ensue to the environment [2]. Off-stoichiometric compositions derived from ferromagnetic Ni_2MnGa Heusler alloy, which undergo transformation from austenitic phase at high temperatures to martensitic phase at lower temperatures [3], are widely studied in this context. Various elements have been substituted to fine tune the martensitic transformation temperature T_M and the modifications caused to the microstructures and physical properties, is investigated [4-10]. There are several reports on systematic dependence of T_M on the electron per atom ratio e/a, in these alloys, and also in alloys of the Ni-Mn-Al. However, iron substituted Ni-Mn-Ga alloys have been observed to be anomalous in their behavior; and their deviation from the normal trend has been discussed in several publications [10-12]. Also in the case of isoelctronic substitutions like In- substituted for Ga, where e/a remains unaltered, prediction of T_M fails.

In the above, valence electron concentration, e/a is computed as an average of the number of electrons beyond the rare gas shell of the atoms involved, considering the alloy composition. We consider here an alternative scheme of computing effective value of valence electron concentration N_e/a and examine the trend of variation in T_M for a number of shape memory alloy systems.

Recent papers on metallic bonding [13] make numerically correct predictions of several properties like volume changes on alloying and lattice parameters, which are related to cohesion in metallic alloys. In this approach, Pauling's idea of transfer of charge [14] on an atom-pair bond to maintain electroneutrality in metallic alloys is adopted. In this model [15-17], Miedema's parameters ϕ and N_{ws} were considered to represent the electronegativity and valence of metallic elements respectively. Miedema's equation for the heat of formation of binary alloys is given below:

$$\Delta H = \left[-\Delta\phi^2 + \frac{Q}{P}\left(\Delta \mathrm{N_{ws}}^{1/3}\right)^2 - \frac{R}{P}\right] \ldots\ldots\ldots\ldots\ldots\ldots (6.1).$$

Where ϕ and $\mathrm{N_{ws}}$ are the work function and the 'electron density at the boundary of the Wigner-Seitz cells' of the elements. The term *R/P* was introduced to correctly reproduce the empirically observed data on the signs of *ΔH* of transition metal -*p*-metal combinations. Its value increases with the valence of the p-metals and is zero for other combinations. Miedema *et al.* [18] suggested that *R/P* has its origin in '*d–p* hybridisation'. Miedema had obtained the numerical values of ϕ and N_{ws} from Pauling's electronegativity and the experimental bulk modulus of the elements respectively, and adjusted them to second decimal accuracy, in order to predict the signs of ΔH of 500 binary systems to an accuracy of 100% [18].

Following the extended Pauling's model, it was also shown that concomitant and mutually exclusive crystal structure types in metallic binary systems can be predicted accurately [16]. The versatility of the above approach suggests that Pauling's scheme of filling electrons in orbitals of metallic atoms could be of interest in the context of predicting the magnetic and electrical properties of metallic alloys.

6.2 Pauling's Scheme of filling electrons in orbitals of metal atoms

Pauling's model has been very controversial in the case of metallic systems [19]. However, it is worth noting that recent *ab*-initio application of

Pauling's Resonating Valence Bond (RVB) theory to simpler systems like Li atom clusters brings out the covalent character of the metal-metal bond and the importance of the metallic orbital [20].

Pauling's approach provided a qualitative explanation of many properties of the transition metals (including those of the palladium and platinum groups), such as interatomic distance, characteristic temperature, hardness, compressibility, and coefficient of thermal expansion, and it accounts satisfactorily for the observed values of the atomic saturation magnetic moments of the ferromagnetic elements iron, cobalt, and nickel and their alloys. Pauling's model on electron filling is discussed below.

Pauling had proposed [21] that in metals, d-orbitals alone are not especially well suited to use in bond formation, but hybridization of d, s, and p orbitals leads to the best bond orbitals known. There are available a total of nine relatively stable orbitals: five $3d$, one $4s$, and three $4p$ for the iron group elements, and corresponding sets for other series. According to him, as per the empirical evidence, about 2.44 d orbitals on an average show only weak interatomic interactions, and the remaining 2.56 d orbitals combine with the s orbital and p orbitals to form hybrid bond orbitals. If N_p is the Pauling's valence of an element, N_p electrons would fill up unpaired in the bond orbitals and would be available for the formation of N_p electron-pair bonds with other atoms. Melting and boiling points of elements would therefore be proportional to N_p.

Let O be the total number of orbitals of an atom; Pauling had argued that O = 9, consisting of five $3d$, one $4s$, and three $4p$ orbitals for the iron group elements, and corresponding sets for other series [21]. Let E be the total number of electrons beyond the inert gas shell of an atom. In the case of atoms with less than 5 electrons beyond the inert gas shell, O = 5, i.e. there is no admixture of the s and p orbitals with the d orbitals. Let N_p be the valence of a metal; Pauling had proposed that N_p orbitals would be filled by an equal number of unpaired electrons which would form resonating covalent bonds with the neighboring

atoms. The number of electrons not involved in bonding would be $E - N_p$. Such electrons were referred to as paired non-bonding electrons by Pauling.

In the modified Pauling's scheme, we have used Miedema's corrected electron density parameter N_{ws} as the valence of metals. Then, N_{ws} electrons per atom would occupy N_{ws} orbitals, i. e. one electron per orbital, and form covalent bonds with the neighboring atoms. The residual electrons fill the remaining $9 - N_{ws}$ orbitals in pairs. These electrons are nonbonding electrons and they contribute to magnetism, electrical properties etc. In the case of ferromagnetic elements such as Fe, Co and Ni, a certain number of the nonbonding electrons would remain unpaired, contributing to the magnetic moments of the atoms. The number of non-bonding electrons is calculated as $(E - N_{ws})$, where E is the number of electrons beyond the rare gas shell of the atom. The plot of $E - N_{ws}$ versus E, given in Fig. 6.1 for all the elements shows that they are not related through a simple linear dependence.

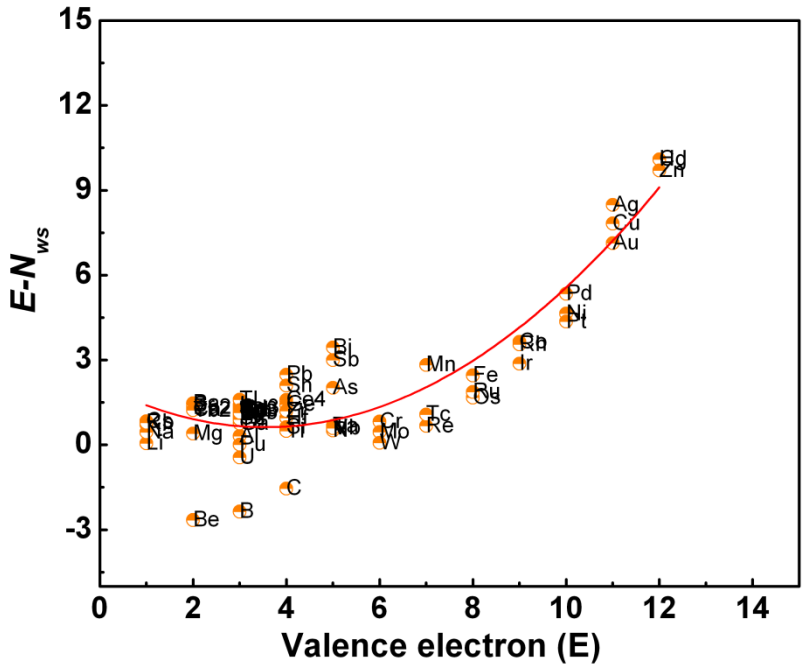

Fig. 6.1. Variation of $(E - N_{ws})$ with E showing a non-linear relation between them. The curve drawn is a fit to a polynomial.

In the following, the 'non-bonding electrons per atom' of a compound ($N_e\ /a$) is calculated from a knowledge of the paired non-bonding electrons e_n contributed by each atom. For this purpose, we redefine e_n as $E - N_{ws}$, where N_{ws} are Miedema's 'electron density parameter'. The choice of Miedema's electron density parameter N_{ws} as the valence of metallic elements (instead of N_p) is discussed in detail elsewhere [15]. The values of N_{ws} for the elements Ni, Mn, Ga, Co, Fe, Al, and In are 5.36, 4.17, 2.25, 5.36, 5.55, 2.69, and 1.6, respectively [18]. As a typical example demonstrating how $N_e\ /a$ for an alloy is calculated, we consider the calculation $Ni_{50}Mn_{26}Ga_{24}$. (E, N_{ws} and e_n) for Ni, Mn and Ga are (10, 5.36 and 4.74), (7, 4.17 and 2.83) and (3, 2.25 and 0.75), respectively. $N_e\ /a$ for the compound is $\{50 \times (10 - 5.36) + 26 \times (7 - 4.17) + 24 \times (3 - 2.25)\}/100$ = 3.24.

6.3 Systematics in the dependence of T_M on electron concentration

The martensitic transformation temperatures T_M of 171 off-stoichiometric alloys in the Ni-Mn-Ga system, 84 quasi-ternary alloys with Co substitution, 76 alloys with Fe substitution, and 7 alloys with indium substitution in Ni-Mn-Ga system, were collected from compilations [1, 2] and individual reports in the literature [4-11, 22-48]. Data were also gathered on T_M of 12 alloys of off-stoichiometric Ni-Mn-Al system [49, 50]. The e/a values of the compounds were computed taking the valences of Ni, Mn, Ga, Co, Fe, Al and In to be 10, 7, 3, 9, 8, 3 and 3 respectively; the individual electron contributions of all atoms are added up in the formula unit and divided by the total number of atoms [51] (as discussed in section 1.8.4 of Chapter 1). The variations in the martensitic transformation temperatures of alloys derived from Ni_2MnGa and Ni_2MnAl with e/a are given in Figs. 6.2 (a), 6.3 (a), 6.4 (a), 6.5 (a), and 6.6 (a).

Figure 6.2 (a) for off-stoichiometric Ni_2MnGa, shows three regions. 141 alloys out of a total of 171 alloys with $e/a \leq 7.72$ show a linear variation of T_M

with e/a. The compounds with $e/a > 7.72$ are the Ni-rich ones having $T_M > T_C$, with potential for high temperature shape memory applications.

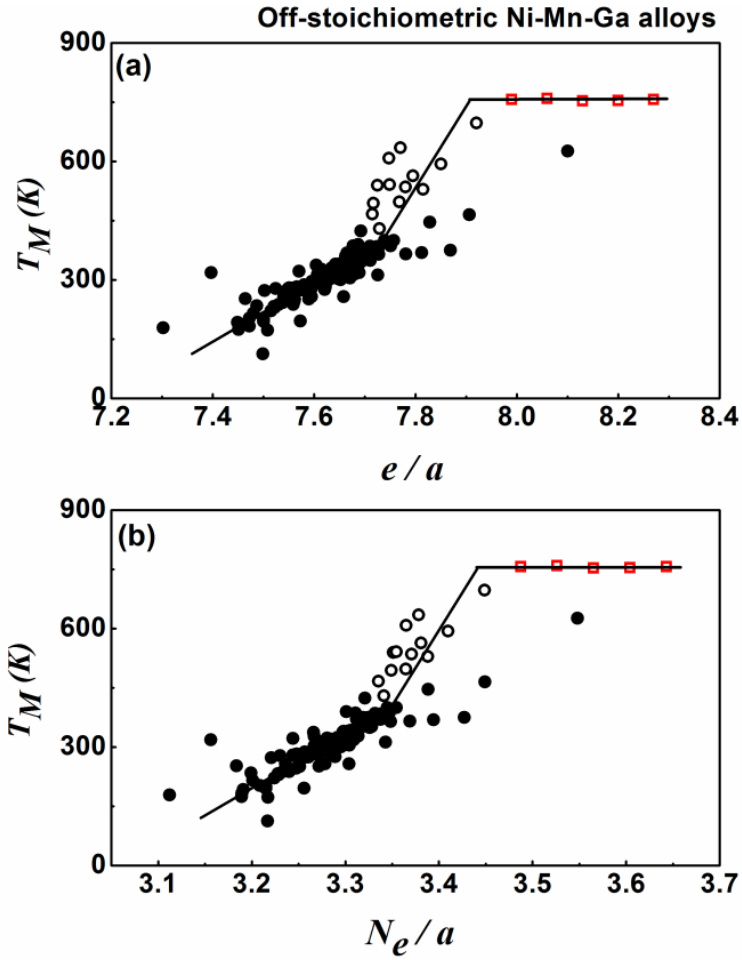

Fig. 6.2. (a) The variation of martensitic transformation temperature T_M in off stoichiometric Ni-Mn-Ga alloys with e/a. 141 alloys with $e/a \leq 7.72$ shows a linear dependence (filled circles). Open circles represent Ni-excess compositions with $T_M > T_C$. $Ni_{50+x}Mn_{25}Ga_{25-x}$ (x = 2-11) compositions with ≥ 57 at. % Ni, represented by open squares (red online) reveal γ- phase precipitation in their microstructure, and hence T_M remains constant with e/a. (b) T_M vs. N_e /a plot for the above alloys shows a dependence similar to that observed in (a). The solid lines shown in the figure, in the three regions, are guide to the eye.

Most of these compounds, which have non-modulated tetragonal structure, show a faster increase in T_M with e/a. This has been attributed to a decrease in their unit cell volumes due to smaller Ni atoms replacing the larger Ga atoms in

the crystal lattice. A combination of increase in e/a and a decrease in cell volumes causes a faster increase in effective electron concentration and hence in the T_M of those alloys [32]. At Ni contents in excess of 57 at.%, γ-phase precipitates out and the concentration of the alloy remains a constant, leading to a constant T_M for e/a values greater than 8.0 (see figure). The e/a values were computed from the nominal composition of the alloys.

In Figs. 6.3 (a) and 6.4 (a), we show T_M versus e/a plots for Co-doped Ni-Mn-Ga and off-stoichiometric Ni-Mn-Al alloys, respectively. We note that the plots are linear.

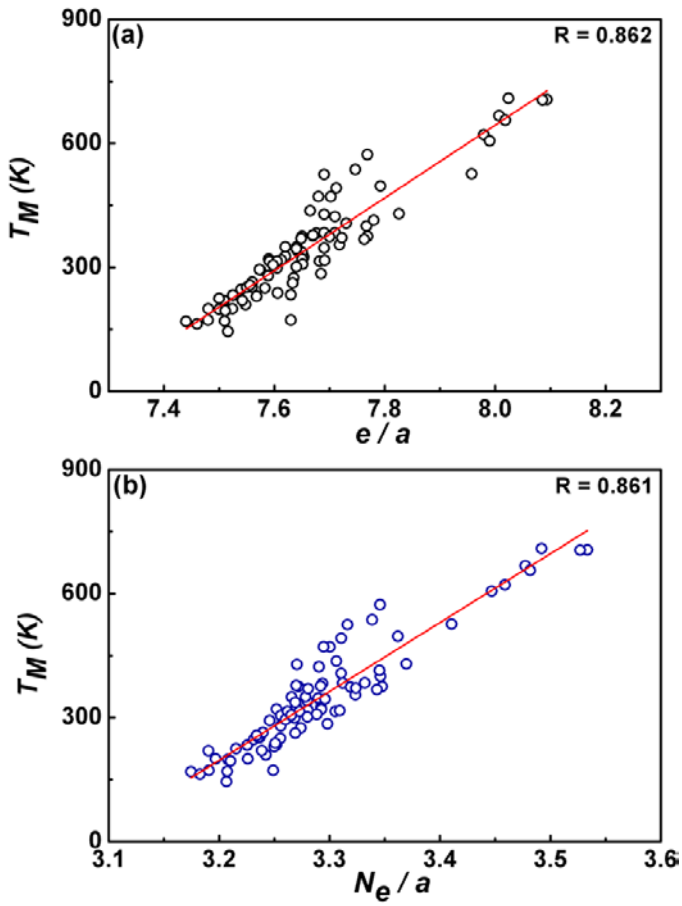

Fig. 6.3. (a) The variation of martensitic transformation temperature T_M plotted for 84 quasi-ternary Co-doped Ni-Mn-Ga alloys showing a linear dependence with e/a, (b) T_M vs N_e $/a$ for the above compounds showing a similar linear dependence as observed in (a).

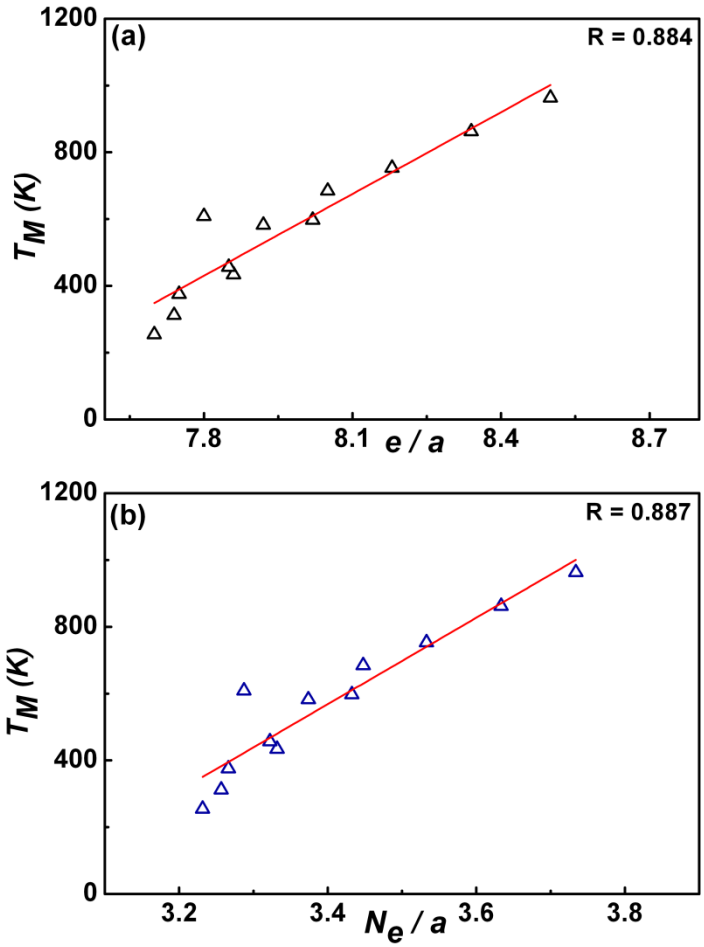

Fig. 6.4. (a) The variation of martensitic transformation temperature T_M plotted for 12 off-stoichiometric Ni-Mn-Al alloys with e/a exhibiting a linear dependence, (b) T_M vs N_e $/a$ plot also shows a similar linear dependence as observed in (a).

In Fig. 6.5 (a), we show the variation of T_M with e/a for compounds with Fe substituted in Ni-Mn-Ga alloys. We have considered 76 compounds which are listed in Table 6.1. It can be observed that the distribution of points in the plot is rather random. The anomalous behavior of iron-containing alloys has been discussed by several authors [10-12]. It has been attributed to factors other than e/a also contributing to the stability of those phases, like the site occupied in ordered structure [43], volume effects associated with atomic sizes [12, 47], magnetic contributions [10] etc.

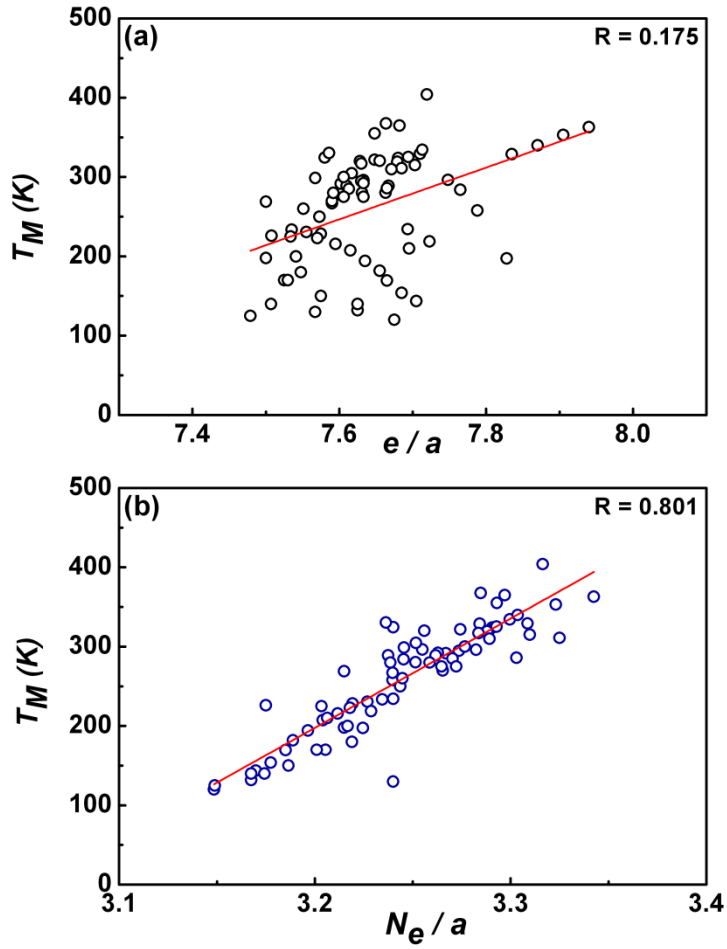

Fig. 6.5. (a) Martensitic transformation temperature T_M is plotted against e/a for 76 quasi-ternary Fe-doped Ni-Mn-Ga compounds. No systematic dependence is observed, (b) T_M vs. N_e/a plot for the same compounds shows a linear dependence with high regression factor, unlike the plot in (a).

We now examine the variation of T_M with the modified electron concentration, viz. non-bonding electrons per atom, N_e/a. The variation of the martensitic transformation temperature of alloys derived from Ni_2MnGa and Ni_2MnAl with N_e/a are given in Figs. 6.2 (b), 6.3 (b), 6.4 (b), 6.5 (b) and 6.6 (b). Figure 6.2(b) for off-stoichiometric Ni_2MnGa compounds also shows three regions as in Fig. 6.2 (a). The T_M of the 141 alloys which show a good linear dependence on e/a (see Fig. 6.2(a)) show an equally good linearity with N_e/a, as can be seen

from Fig. 6.2 (b). The faster increase in T_M for Ni-rich phases, and also the effect of γ-phase precipitation at higher Ni content are reproduced with $N_e\ /a$.

We also note a systematic linear dependence of T_M on $N_e\ /a$ for Co-doped Ni-Mn-Ga and off-stoichiometric Ni-Mn-Al alloys in Figs. 6.3 (b) and 6.4 (b), respectively.

In Fig. 6.5 (b), we show a plot of T_M versus $N_e\ /a$ for the iron-substituted alloys derived from Ni_2MnGa and listed in Table 6.1. From the regression factors (R) indicated in the figures, one can see a remarkable improvement (R = 0.801) in the correlation shown in Fig. 6.5 (b), in comparison with the plot in Fig. 6.5 (a), with R = 0.175. Hence the correlation of T_M with $N_e\ /a$ can be used to predict T_M of new compositions in the Ni-Mn-Ga-Fe system. The anomalous behavior seen in Fe-containing compounds when using the earlier electron counting scheme is thus resolved.

We consider below the case of isoelectronic substitutions like $Ni_2MnGa_{1-x}In_x$ alloys. In Fig. 6.6 (a) we observe that the T_M versus e/a plot for $Ni_2MnGa_{1-x}In_x$ alloys does not exhibit any useful trend since the valences assumed conventionally are the same for the isoelectronic-elements like Ga and In, viz. 3. The variation in T_M with composition of In-doped alloys has been attributed to volume effects associated with atomic sizes [52] because e/a of the alloy series remains a constant. In Fig. 6.6 (b) we show the dependence of T_M on the non-bonding electrons per atom ($N_e\ /a$).

Table 6.1 The chemical composition, martensitic transformation temperature (T_M), electron per atom ratio (e/a) for different Fe-doped Ni-Mn-Ga compounds from literature and the non-bonding electron per atom ratio ($N_e\ /a$) computed in the present work.

S. No	Composition (at.%)	T_M (K)	e/a	$N_e\ /a$	Ref.	S. No	Composition (at.%)	T_M (K)	e/a	$N_e\ /a$	Ref.
1	$Ni_{47.3}Mn_{25.9}Ga_{20.4}Fe_{6.4}$	289	7.67	3.24	[4]	**39**	$Ni_{47.3}Mn_{30.3}Ga_{20.3}Fe_{2.1}$	320	7.63	3.26	[42]
2	$Ni_{49.4}Mn_{27.5}Ga_{21.3}Fe_{1.8}$	321.7	7.65	3.27	[4]	**40**	$Ni_{48.9}Mn_{29.0}Ga_{19.5}Fe_{2.6}$	334.5	7.71	3.30	[42]
3	$Ni_{50.9}Mn_{20.2}Ga_{23.7}Fe_{5.2}$	280	7.63	3.24	[4]	**41**	$Ni_{48.8}Mn_{29.2}Ga_{20.1}Fe_{1.9}$	319.3	7.68	3.29	[42]
4	$Ni_{51.8}Mn_{24.3}Ga_{23.2}Fe_{0.7}$	296	7.63	3.28	[4]	**42**	$Ni_{48.6}Mn_{27.5}Ga_{21.6}Fe_{2.3}$	304.7	7.62	3.25	[42]
5	$Ni_{50.5}Mn_{25.0}Ga_{24.5}Fe_{0}$	233.6	7.54	3.23	[10]	**43**	$Ni_{48.9}Mn_{26.2}Ga_{22.6}Fe_{2.3}$	330.5	7.59	3.24	[42]
6	$Ni_{50.5}Mn_{23.0}Ga_{24.5}Fe_{2.0}$	230.6	7.56	3.23	[10]	**44**	$Ni_{49.4}Mn_{27.9}Ga_{20.3}Fe_{2.4}$	325.3	7.69	3.29	[42]
7	$Ni_{50.5}Mn_{21.0}Ga_{24.5}Fe_{4.0}$	228.4	7.58	3.22	[10]	**45**	$Ni_{51.1}Mn_{23.0}Ga_{24.5}Fe_{1.4}$	130	7.57	3.24	[43]
8	$Ni_{50.5}Mn_{19.0}Ga_{24.5}Fe_{6.0}$	215.6	7.60	3.21	[10]	**46**	$Ni_{50.14}Mn_{23.0}Ga_{24.5}Fe_{2.36}$	180	7.55	3.22	[43]
9	$Ni_{50.5}Mn_{17.0}Ga_{24.5}Fe_{8.0}$	207.5	7.62	3.20	[10]	**47**	$Ni_{49.43}Mn_{23.0}Ga_{24.5}Fe_{3.07}$	225	7.53	3.20	[43]
10	$Ni_{50.5}Mn_{15.0}Ga_{24.5}Fe_{10.0}$	194.2	7.64	3.20	[10]	**48**	$Ni_{48.13}Mn_{23.0}Ga_{24.5}Fe_{4.37}$	226	7.51	3.17	[43]
11	$Ni_{50.5}Mn_{13.0}Ga_{24.5}Fe_{12.0}$	181.9	7.66	3.19	[10]	**49**	$Ni_{47.27}Mn_{23.0}Ga_{24.5}Fe_{5.23}$	227	7.49	3.16	[43]
12	$Ni_{50.5}Mn_{12.0}Ga_{24.5}Fe_{13.0}$	169.6	7.67	3.19	[10]	**50**	$Ni_{50.0}Mn_{12.5}Ga_{25.0}Fe_{12.5}$	132	7.63	3.17	[44]
13	$Ni_{50.5}Mn_{10.0}Ga_{24.5}Fe_{15.0}$	153.9	7.69	3.18	[10]	**51**	$Ni_{51.0}Mn_{12.5}Ga_{24.0}Fe_{12.5}$	210	7.70	3.21	[44]
14	$Ni_{50.5}Mn_{8.0}Ga_{24.5}Fe_{17.0}$	143.7	7.71	3.17	[10]	**52**	$Ni_{52.0}Mn_{12.5}Ga_{23.0}Fe_{12.5}$	284	7.77	3.25	[44]
15	$Ni_{50.4}Mn_{28.0}Ga_{21.6}Fe_{0}$	355.1	7.65	3.29	[10]	**53**	$Ni_{53.0}Mn_{12.5}Ga_{22.0}Fe_{12.5}$	329	7.84	3.28	[44]
16	$Ni_{50.4}Mn_{18.0}Ga_{21.6}Fe_{10.0}$	296.4	7.75	3.25	[10]	**54**	$Ni_{53.5}Mn_{12.5}Ga_{21.5}Fe_{12.5}$	340	7.87	3.30	[44]
17	$Ni_{50.4}Mn_{14.0}Ga_{21.6}Fe_{14.0}$	257.9	7.79	3.24	[10]	**55**	$Ni_{54.0}Mn_{12.5}Ga_{21.0}Fe_{12.5}$	353	7.91	3.32	[44]
18	$Ni_{50.4}Mn_{10.0}Ga_{21.6}Fe_{18.0}$	197.4	7.83	3.22	[10]	**56**	$Ni_{54.5}Mn_{12.5}Ga_{20.5}Fe_{12.5}$	363	7.94	3.34	[44]
19	$Ni_{50.0}Mn_{25.0}Ga_{25.0}Fe_{0}$	198	7.50	3.22	[11]	**57**	$Ni_{47.64}Mn_{31.91}Ga_{19.4}Fe_{1.05}$	367.7	7.66	3.28	[45]
20	$Ni_{50.0}Mn_{22.5}Ga_{25.0}Fe_{2.5}$	170	7.53	3.21	[11]	**58**	$Ni_{48.56}Mn_{30.94}Ga_{19.6}Fe_{0.99}$	365	7.68	3.30	[45]
21	$Ni_{50.0}Mn_{17.5}Ga_{25.0}Fe_{7.5}$	150	7.58	3.19	[11]	**59**	$Ni_{48.5}Mn_{31.87}Ga_{18.64}Fe_{0.99}$	404	7.72	3.32	[45]
22	$Ni_{50.0}Mn_{12.5}Ga_{25.0}Fe_{12.5}$	140	7.63	3.17	[11]	**60**	$Ni_{55.5}Mn_{20.0}Ga_{24.5}Fe_{0}$	311	7.69	3.32	[46]
23	$Ni_{50.0}Mn_{7.5}Ga_{25.0}Fe_{17.5}$	120	7.68	3.15	[11]	**61**	$Ni_{54.5}Mn_{20.0}Ga_{24.5}Fe_{1.0}$	286	7.67	3.30	[46]
24	$Ni_{48.7}Mn_{30.1}Ga_{22.2}Fe_{0}$	298.8	7.57	3.25	[12]	**62**	$Ni_{52.6}Mn_{23.1}Ga_{24.3}Fe_{0}$	300	7.61	3.28	[47]
25	$Ni_{48.7}Mn_{28.1}Ga_{21.2}Fe_{2.0}$	292.1	7.63	3.26	[12]	**63**	$Ni_{51.3}Mn_{22.8}Ga_{24.5}Fe_{1.4}$	250	7.57	3.24	[47]
26	$Ni_{48.7}Mn_{25.1}Ga_{21.2}Fe_{5.0}$	280.4	7.66	3.25	[12]	**64**	$Ni_{50.1}Mn_{23.1}Ga_{24.6}Fe_{2.2}$	200	7.54	3.22	[47]
27	$Ni_{48.7}Mn_{22.1}Ga_{21.2}Fe_{8.0}$	234.2	7.69	3.24	[12]	**65**	$Ni_{49.3}Mn_{23.1}Ga_{24.5}Fe_{3.1}$	170	7.53	3.20	[47]
28	$Ni_{48.7}Mn_{19.1}Ga_{21.2}Fe_{11.0}$	218.7	7.72	3.23	[12]	**66**	$Ni_{48.1}Mn_{23.0}Ga_{24.5}Fe_{4.4}$	140	7.51	3.17	[47]
29	$Ni_{50.0}Mn_{27.0}Ga_{22.0}Fe_{1.0}$	294.7	7.63	3.27	[22]	**67**	$Ni_{47.0}Mn_{23.1}Ga_{24.6}Fe_{5.3}$	125	7.48	3.15	[47]
30	$Ni_{50.0}Mn_{27.0}Ga_{21.0}Fe_{2.0}$	324	7.68	3.29	[22]	**68**	$Ni_{51.4}Mn_{24.8}Ga_{23.8}Fe_{0}$	270	7.59	3.27	[47]
31	$Ni_{47.0}Mn_{31.0}Ga_{21.0}Fe_{1.0}$	324.5	7.58	3.24	[22]	**69**	$Ni_{51.5}Mn_{24.2}Ga_{23.5}Fe_{0.8}$	285	7.61	3.27	[47]
32	$Ni_{54.0}Mn_{20.0}Ga_{25.0}Fe_{1.0}$	317	7.63	3.28	[40]	**70**	$Ni_{51.1}Mn_{24.6}Ga_{23.4}Fe_{0.9}$	275	7.61	3.26	[47]
33	$Ni_{53.0}Mn_{20.0}Ga_{25.0}Fe_{2.0}$	289	7.61	3.26	[40]	**71**	$Ni_{51.7}Mn_{23.1}Ga_{23.4}Fe_{1.8}$	275	7.63	3.27	[47]
34	$Ni_{52.0}Mn_{20.0}Ga_{25.0}Fe_{3.0}$	267	7.59	3.24	[40]	**72**	$Ni_{51.3}Mn_{24.0}Ga_{24.7}Fe_{0}$	260	7.55	3.24	[47]
35	$Ni_{51.0}Mn_{20.0}Ga_{25.0}Fe_{4.0}$	223	7.57	3.22	[40]	**73**	$Ni_{51.2}Mn_{24.2}Ga_{23.8}Fe_{0.8}$	280	7.59	3.26	[47]
36	$Ni_{52.1}Mn_{23.0}Ga_{24.2}Fe_{0.7}$	291.7	7.60	3.27	[42]	**74**	$Ni_{51.8}Mn_{24.8}Ga_{21.7}Fe_{1.7}$	315	7.70	3.31	[47]
37	$Ni_{51.7}Mn_{24.4}Ga_{22.7}Fe_{1.2}$	320.5	7.66	3.29	[42]	**75**	$Ni_{51.3}Mn_{24.5}Ga_{22.2}Fe_{2.0}$	310	7.67	3.29	[47]
38	$Ni_{49.9}Mn_{28.3}Ga_{20.1}Fe_{1.7}$	329.3	7.71	3.31	[42]	**76**	$Ni_{50.0}Mn_{25.0}Ga_{25.0}Fe_{0}$	269	7.50	3.22	[48]

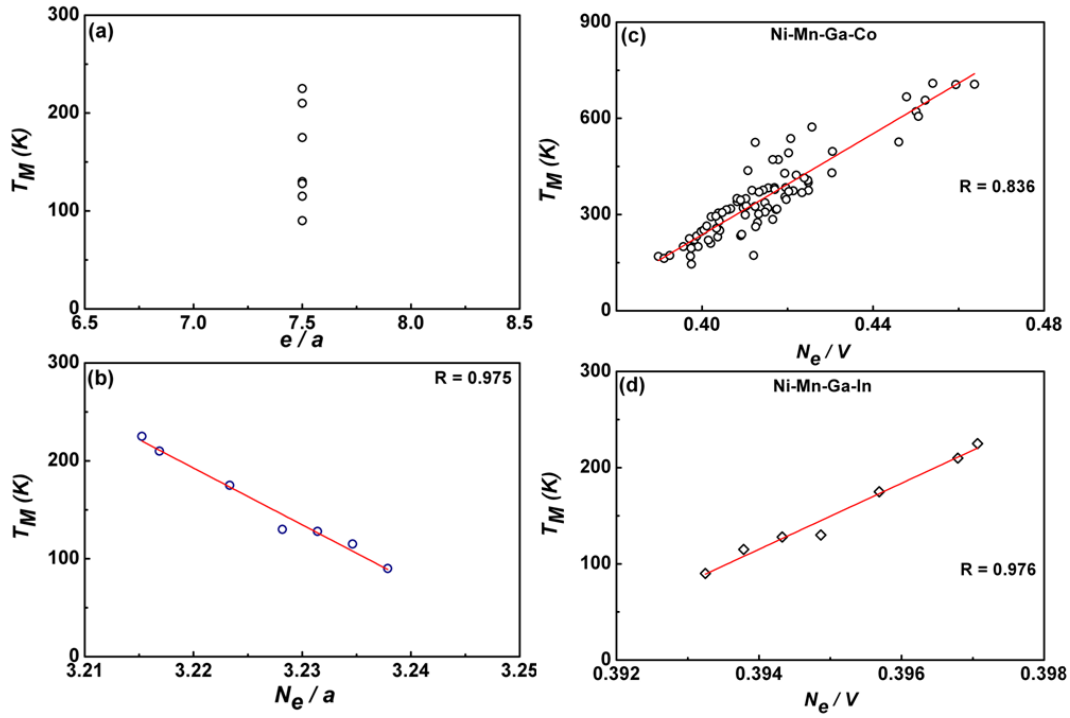

Fig. 6.6. (a) Variation of martensitic transformation temperature T_M plotted for quasi-ternary $Ni_2MnGa_{1-x}In_x$ compounds, with e/a. No useful conclusion can be drawn from the figure since the valences for both Ga and In are the same, thus leading to a constant e/a for all the compounds, (b) T_M vs. N_e/a plot for the compounds is linear and the graph can be used to predict the T_M of new compounds belonging to the same system. Variation of T_M with electron concentration per unit volume N_e/V for (c) quasi-ternary Ni-Mn-Ga-Co alloys and (d) for $Ni_2MnGa_{1-x}In_x$ alloys, respectively. The change in trend of (b) and (d) confirm the role of volume effects.

The systematic dependence in the figure suggests that useful predictions can be made on the T_M of a new composition in the system. However, T_M shows a decreasing trend with N_e/a, which is at variance with observations in all other systems shown earlier. In order to examine the role of volume effects associated with atomic sizes, we computed N_e/V that defines the electron concentration per unit volume. Here, V is calculated as the average (atomic) volume per atom. We show the variation of T_M with N_e/V for the alloys of quasi-ternary Ni-Mn-Ga-Co and $Ni_2MnGa_{1-x}In_x$ in Figs. 6.6 (c) and (d) respectively. The trend of variation in T_M with N_e/a and N_e/V are the same (Figs. 6.3 and 6.6 (c)) for Ni-Mn-Ga-Co

alloys while the trend reverses (Figs. 6.6 (b) and (d)) for $Ni_2MnGa_{1-x}In_x$ alloys confirming the role of volume effects. The general trend of increase in T_M with electron concentration can be seen in Ni-Mn-Ga-Co system as well as in Ni-Mn-Ga-In system.

The various results discussed above suggest that alternate ways of computing effective electron concentration are worth exploring to understand the mechanisms determining the martensitic transformation temperatures in shape memory alloys, in addition to considering factors like volume effects and magnetic interactions as suggested in literature.

6.4 Conclusions

This work presents a scheme of computing electron concentration of ferromagnetic shape memory alloys derived from Ni_2MnGa, based on Pauling's ideas on the electronic structure of metallic elements. For this, Miedema's electron density parameters N_{ws} are taken as accurate valences of metallic elements and are considered to be the number of bonding electrons, which contribute only to cohesion. Only the non-bonding electrons, $e_n = E - N_{ws}$ are considered relevant in computing the modified electron per atom ratio (N_e/a) of the compounds, instead of e/a which is calculated from E, the total number of electrons outside the rare gas shell. We show systematic variations of T_M with N_e/a for a large number of compounds consisting of the off-stoichiometric alloys of Ni-Mn-Ga and Ni-Mn-Al, and quasi-ternary alloys of Ni-Mn-Ga with Co, Fe, and In substitutions. The anomaly observed for Fe containing alloys with e/a has disappeared, and a systematic dependence is observed when T_M is plotted against N_e/a. It is also shown that T_M can be predicted for alloys with isoelectronic substitutions like in Ni-Mn-Ga-In system. The present results suggest that the non-bonding electron concentration can be used to successfully predict T_M of shape memory alloys of Ni-Mn-Ga system.

References

[1] A.N. Vasil'ev, V.D. Buchel'nikov, T. Takagi, V.V. Khovailo and E.I. Estrin, *Physics – Uspekhi.* **46** (2003) 559.

[2] A. Planes, L. Manosa and M. Acet, *J. Phys.: Condens. Matter.* **21** (2009) 233201.

[3] P.J. Webster, K.R.A. Ziebeck, S.L. Town and M.S. Peak, *Phil. Mag. B* **49** (1984) 295.

[4] Glavatskyy, N. Glavatska, O. Söderberg, S. –P. Hannula and J. –U. Hoffmann, *Scripta Mater.* **54** (2006) 1891.

[5] X.Q. Chen, F.J. Yang, X. Lu and Z.X. Qin, *Phys. Stat. Sol. (b)* **244** (2007) 1047.

[6] D.E. Soto-Parra, X. Moya, L. Mañosa, A. Planes, H. Flores-Zúñiga, F. Alvarado-Hernández, R.A. Ochoa-Gamboa, J.A. Matutes-Aquino and D. Ríos-Jara, *Phil. Mag.* **90** (2010) 2771.

[7] V. Sánchez-Alarcos, J.I. Pérez-Landazábal, V. Recarte, C. Gómez-Polo and J.A. Rodríguez-Velamazán, *Acta Mater.* **56** (2008) 5370.

[8] X.Q. Chen, X.Lu, D.Y. Wang and Z.X. Qin, *Smart Mater. Struct.* **17** (2008) 065030.

[9] D.Y. Cong, S. Wang, Y.D. Wang, Y. Ren, L. Zuo and C. Esling, *Mater. Sci. Eng. A* **473** (2008) 213.

[10] Z.H. Liu, M. Zhang, W.Q. Wang, W.H. Wang, J.L. Chen, G.H. Wu, F.B. Meng, H.Y. Liu, B.D. Liu, J.P. Qu and Y.X. Li, *J. Appl. Phys.* **92** (2002) 5006.

[11] D. Kikuchi, T. Kanomata, Y. Yamaguchi, H. Nishihara, K. Koyama and K. Watanabe, *J. Alloys Compd.* **383** (2004) 184.

[12] F. Chen, H. B. Wang, Y.F. Zheng, W. Cai and L.C. Zhao, *J. Mater. Sci.* **40** (2005) 219.

[13] T. Rajasekharan and V. Seshubai, *Acta Crystl.* (2011) (In press)

[14] L. Pauling, *Proc. Natl Acad. Sci.* USA, **36** (1950) 533.

[15] T. Rajasekharan and V. Seshubai, *J. Mater. Res.* **26** (2011) 1539.

[16] V.L. Kameswari, V. Seshubai and T. Rajasekharan, *J. Alloys Compd.* **508** (2010) 55.

[17] T. Rajasekharan and V. Seshubai, *Intermetallics* **18** (2010) 666.

[18] A.R. Miedema, P.F. De Chatel and F.R. De Boer, *Physica* **100B** (1980) 1.

[19] P. Anderson, *Phys. Today* **61** (2008) 8.

[20] J.R. Mohallem, R.O. Vianna, A.D. Quintao, A.C. Pavao and R. McWeeny, *Z. Phys. D* **42** (1997) 135.

[21] L. Pauling, *Phys. Rev.* **54** (1938) 899.

[22] S. Guo, Y. Zhang, B. Quan, J. Li, Y. Qi and X. Wang, *Smart Mater. Struct.* **14** (2005) S236.

[23] V.A. Chernenko, E. Cesari, V.V. Kokorin and I.N. Vitenko, *Scripta Metall. Mater.* **33** (1995) 1239.

[24] C.J. O'Connor, V.O. Golub, A. Ya. Vovk, V.V. Kotov, P. Yakovenko and K. Ullakko, *IEEE Trans. Mag.* **38** (2002) 2844.

[25] V.V. Khovailo, K. Oikawa, T. Abe and T. Takagi, *J. Appl. Phys.* **93** (2003) 8483.

[26] L. Pareti, M. Solzi, F. Albertini and A. Paouluzi, *Eur. Phys. J. B* **32** (2003) 303.

[27] X. Zhou, W. Li, H.P. Kunkel and G. Williams, *J. Phys.: Condens. Matter* **16** (2004) L39.

[28] N. Lanska, O. Söderberg, A. Sozinov, Y. Ge, K. Ullakko and V.K. Lindroos, *J. Appl. Phys.* **95** (2004) 8074.

[29] C. Jiang, Y. Muhammad, L. Deng, W. Wu and H. Xu, *Acta Mater.* **52** (2004) 2779.

[30] V.V. Khovaylo, V.D. Buchelnikov, R. Kainuma, V.V. Koledov, M. Ohtsuka, V.G. Shavrov, T. Takagi, S.V. Taskaev and A.N. Vasiliev, *Phys. Rev. B* **72** (2005) 224408.

[31] M. Richard, J. Feuchtwanger, D. Schlagel, T. Lograsso, S. M. Allen and R.C. O'Handley, *Scripta Mater.* **54** (2006) 1797.

[32] Y. Ma, C. Jiang, Y. Li, H. Xu, C. Wang and X. Liu, *Acta Mater.* **55** (2007) 1533.

[33] X. Zhou, H. Kunkel, G. Williams, S. Zhang and X. Desheng, *J. Magn. Magn. Mater.* **305** (2006) 372.

[34] B. Ingale, R. Gopalan, M. Manivel Raja, V. Chandrasekharan and S. Ram, *J. Appl. Phys.* **102** (2007) 013906.

[35] M.L. Richard, J. Feuchtwanger, S.M. Allen, R.C. O'Handley, P. Lazpita, J.M. Barandiaran, J. Gutierrez, B. Ouladdiaf, C. Mondelli, T. Lograsso and D. Schlagel, *Phil. Mag.* **87** (2007) 3437.

[36] J. Pons, V.A. Chernenko, R. Santamarta and E. Cesari, *Acta Mater.* **48** (2000) 3027.

[37] M. Khan, I. Dubenko, S. Stadler and N. Ali, *J. Appl. Phys.* **97** (2005) 10M304.

[38] Y. Ma, S. Yang, Y. Liu, and X. Liu *Acta Mater.* **57** (2009) 3232.

[39] S. Fabbrici, J. Kamarad, Z. Arnold, F. Casoli, A. Paoluzi, F. Bolzoni, R. Cabassi, M. Solzi, G. Porcari, C. Pernechele and F. Albertini, *Acta Mater.* **59** (2011) 412.

[40] V.V. Khovailo, T. Abe, V.V. Koledov, M. Matsumoto, H. Nakamura, R. Note, M. Ohtsuka, V.G. Shavrov and T. Takagi, *Mater. Trans.* **44** (2003) 2509.

[41] A. Satish Kumar, M. Ramudu and V. Seshubai, *J. Alloys Compd.* **509** (2011) 8215.

[42] K. Koho, O. Söderberg, N. Lanska, Y. Ge, X. Liu, L. Straka, J. Vimpari, O. Heczko and V.K. Lindroos, *Mater. Sci. and Eng. A* **378** (2004) 384.

[43] D.E. Soto-Parra, F. Alvarado-Hernandez, O. Ayala, R.A. Ochoa-Gamboa, H. Flores-Zúñiga and D. Rios-Jara, *J. Alloys Compd.* **464** (2008) 288.

[44] D. Kikuchi, T. Kanomata, Y. Yamaguchi and H. Nishihara, *J. Alloys Compd.* **426** (2006) 223.

[45] R.K. Singh, M. Manivel Raja, R.P. Mathur and M. Samsuddin, *J. Magn. Magn. Mater.* **323** (2011) 574.

[46] J. Duan, P. Huang, H. Zhang, Y. Long, G. Wu, R. Ye, Y. Chang and F. Wan, *J. Magn. Magn. Mater.* **309** (2007) 96.

[47] D. Soto, F.A. Hernandez, H.F. Zuniga, X. Moya, L. Manosa, A. Planes, S. Aksoy, M. Acet and T. Krenke, *Phys. Rev. B* **77** (2008) 184103.

[48] H. Luo, F. Meng, Z. Feng, Y. Li, W. Zhu, G. Wu, X. Zhu, C. Jiang and H. Xu, *J. Appl. Phys.* **107** (2010) 013905.

[49] R. Kainuma, H. Nakano and K. Ishida, *Metall. Mater. Trans.* **27A** (1996) 4153.

[50] R. Kainuma, W. Ito, R.Y. Umetsu, K. Oikawa and K. Ishida, *Appl. Phys. Lett.* **93** (2008) 091906.

[51] V. A. Chernenko, *Scripta Mater.* **40**, 523 (1999).

[52] M. Khan, I. Dubenko, S. Stadler and N. Ali, *J. Phys.: Condens. Matter.* **16** (2004) 5259.

Chapter 7

Summary and Conclusions

Among the ferromagnetic Heusler alloys, those derived from Ni-Mn-Ga system have been widely studied owing to exciting phenomena like large magnetic field induced strain, magnetocaloric effect, magnetoresistance or high temperature shape memory effect that have been observed in them [1-5] at different compositions. These alloys undergo a first order structural (martensitic) transformation from cubic austenite to low symmetry martensite phase on cooling. Stoichiometric Ni_2MnGa undergoes martensitic transformation at T_M = 202 K and a magnetic transition at Curie temperature, T_C of 376 K. Several kinds of lattice modulation viz. five-layered (5M), seven-layered (7M) and non-modulated (NM) structural ordering were observed in the martensitic state of Ni-Mn-Ga alloys [6, 7] depending on the composition and processing conditions. The alloys with superstructural ordering (or lattice modulation) are known to have low twinning energies and are found to exhibit a large MSM effect if they possess high magnetic anisotropy energy, as reported for many Mn-rich compositions [8]. There are several reports on off-stoichiometric alloys of Ni-Mn-Ga, aimed at enhancing the T_M to above room temperature to suit applications. It was observed that T_M follows a general trend of increase with increase in electron concentration e/a. Large rise in T_M was observed in Ni-rich alloys of $Ni_{2+x}Mn_{1-x}Ga$ system, in which coupled magnetostructural transformations (with $T_M \sim T_C$) have been reported for x = 0.18-0.28, above room temperature [9]. These alloys exhibit considerable magnetocaloric effect near T_M. The alloys of this system with x > 0.18 crystallize in tetragonal structure with no lattice modulation. They possess $T_M > T_C$ and hence find application as high temperature shape memory alloys. However, non-modulated phases require much larger applied stresses or fields to cause strain, when compared to alloys with lattice modulation. In general, the structural

and magnetic parameters that determine their potential for applications are transformation temperatures T_M and T_C, crystal structure, superstructural ordering/modulation, the saturation magnetization, and magnetocrystalline anisotropy in martensitic phase of Ni-Mn-Ga alloys.

The structural and magnetic properties of these alloys are very sensitive to the composition and atomic order of the alloys. In order to tune the properties of the Ni-Mn-Ga alloys, one can either vary its composition or introduce other elements by substitution [9-11]. There is also a need to optimize the processing conditions. Substitution of other transition metals like Fe, Co for Ni or Mn, and of p- metals for Ga in Ni-Mn-Ga system [12-17] are known to alter the transition temperatures and physical properties of these materials significantly. Rare earth elements when introduced into Ni-Mn-Ga show low solubility and segregate at the grain boundaries [18]. Light element like boron, when added may occupy either the regular site in the crystal lattice or, an interstitial site due to its small size, but would affect the transformation temperatures and magnetic properties significantly [19-21].

Though there are numerous reports [10-21] on the properties of off-stoichiometric ternary alloys and quasi-ternary alloys of Ni-Mn-Ga, in literature, practical application of Ni-Mn-Ga alloys as actuators is constrained by their extreme brittleness and low strength. In order to overcome these drawbacks one has to suitably modify the microstructures of these materials. Investigations on Ni-Al [22, 23], Cu-Ni-Al [24, 25] and Ti-Pd-Ni [26-28] alloys, reported in literature, reveal that modifications brought about in the microstructures of the martensitic phase of these materials by boron addition have a strong bearing on the resultant mechanical properties.

The effect of boron substituted for Mn and Ga on the structural and magnetic transformation temperatures were reported from a study of $Ni_2Mn_{1-x}B_xGa$ [19] and $Ni_2MnGa_{1-x}B_x$ [20] series. In $Ni_{50}Mn_{36.5}Sb_{13.5-x}B_x$ system [21] it is observed that saturation magnetization decreases monotonously with boron content which is attributed to the smaller atomic radius of B atom compared to

that of Sb, which shortens the distance between the Mn atoms and enhances the antiferromagnetic coupling between them. Fe in $Ni_{48.7}Mn_{30.1-x}Fe_xGa_{21.2}$ (x = 0-11) [29] has been reported to enhance fracture toughness and grain boundary strength due to second phase segregation at the grain boundaries. Improved compression strength and ductility through substitution of Yttrium [30] and an increase in bending strength by Gd substitution [31] in $Ni_{50}Mn_{29}Ga_{21}$ alloy have been reported. This improvement in mechanical properties is attributed to grain refinement, and grain boundary strengthening due to second phase segregation. However, shape memory properties have not been reported in these systems.

Since boron has a tendency to cause second phase segregation, it is interesting to study the influence of boron on the microstructural features of Ni-Mn-Ga alloys. Correlation of transformation temperatures and magnetic properties to microstructural alterations brought about by boron is worth being studied. The effect of boron on the superstructural ordering and mechanical behavior of Ni-Mn-Ga alloys have also not been explored so far in literature.

In this thesis, we present the results from the investigations on the mechanical and magnetic properties of $Ni_{53.5}Mn_{26.0}Ga_{20.5}B_x$ alloys, derived from the parent composition with x = 0. The modifications caused by boron to the structural and microstructural properties are also studied in detail. Attempts are made to bring out correlations between results from various measurements.

To start with, a Ni-rich composition $Ni_{53.5}Mn_{26.0}Ga_{20.5}$ was synthesized in single phase. Detailed structural, microstructural and mechanical properties of this alloy were carried out. This is an off-stoichiometric composition with excess Ni doped for Ga, in Ni_2MnGa. This alloy exhibits magneto-structural transition near 351 K, where T_M is observed close to T_C. This composition crystallizes into a monoclinic structure with 7M superstructural ordering as determined from XRD and confirmed from TEM-SAED studies. It is interesting that the electron concentration of this alloy e/a = 7.785, which is greater than the proposed critical value (upper limit) of 7.7 for lattice modulation. This is attributed to the modified process conditions, as discussed in Chapter 3. Considerable magnetic entropy

change of 13.9 J/kg-K was observed for a magnetic field of 5 T during heating. Observation of magnetic entropy change is attributed to the occurrence of coupled magneto-structural transformation in this alloy.

Detailed microstructural studies reveal distinct features with multi-mode twinning indicative of low residual stresses in the polycrystalline alloy. Such low stresses are believed to originate from a martensitic transformation from cubic austenite to low-symmetry monoclinic structure of the martensitic phase [32, 33]. Different types of twinning modes like crossing twins, parallel bands and twins within twins were present in this alloy as shown in Fig. 7.1.

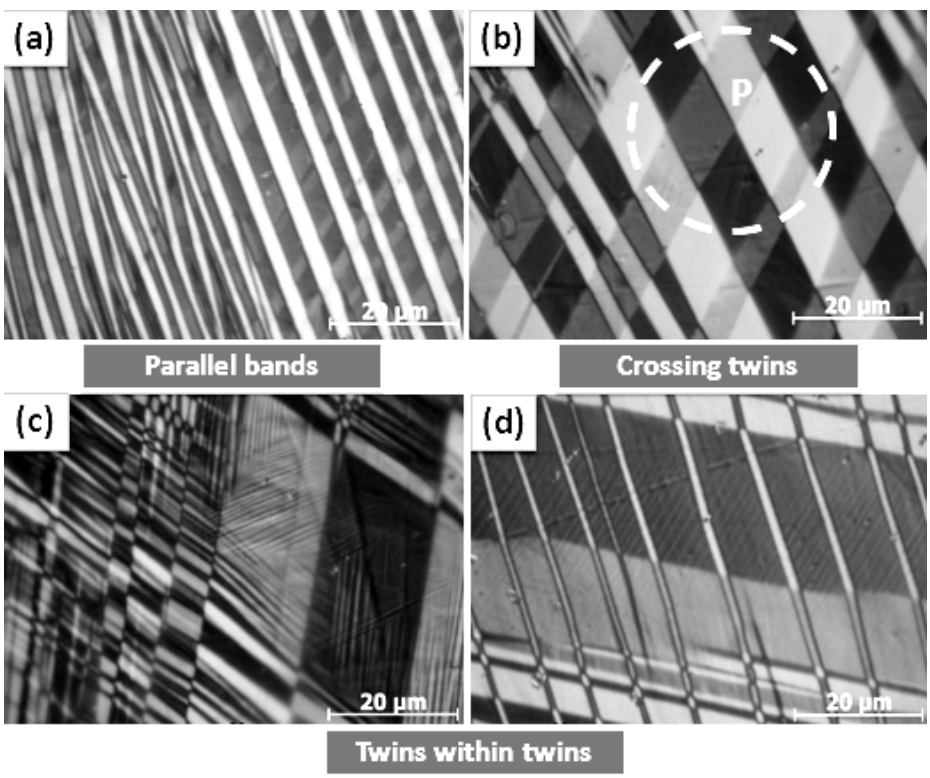

Fig. 7.1. Optical microstructure of the $Ni_{53.5}Mn_{26.0}Ga_{20.5}$ alloy recorded at RT showing multimode twinning including crossing twins, parallel bands and twins within twins as shown in (a), (c) and (d).

The stress-strain curve during loading and unloading for the present sample demonstrate a SME of 1.6 % in the polycrystalline form at RT, as discussed in Chapter 3. The low yield stress of 12 MPa and large strain recovery of 89% observed are attributed to the low twinning energies in the martensitic phase, and

are attributed to the observed lattice modulation and the self-accommodation through multi-mode twinning throughout the sample. The present alloy can be attractive for shape memory applications above RT in polycrystalline form.

Following this study, the effect of introducing boron into this alloy is investigated with regard to the structural, magnetic and compressive stress-strain properties. Studies on $Ni_{53.5}Mn_{26.0}Ga_{20.5}B_x$ (x = 0, 0.5 and 1) (referred as B-0, B-0.5 and B-1.0) alloys reveal that boron addition has not altered the monoclinic crystal structure of the B-0 alloy with increasing boron content (Fig. 7.2), but has altered the superstructural ordering from 7M to 5M when 1 at.% boron is added, as evidenced from TEM-SAED studies.

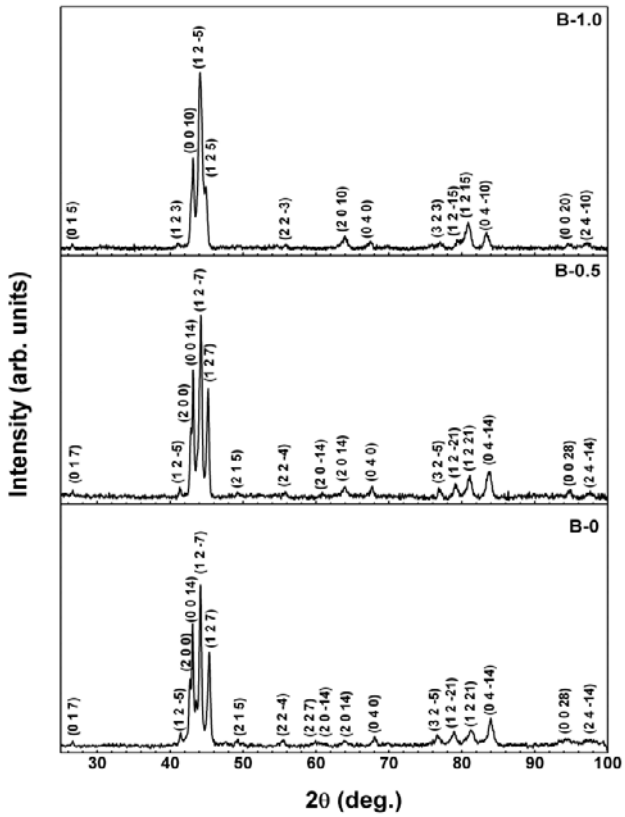

Fig. 7.2. Powder X-ray diffraction patterns recorded at ambient temperature. Based on the results from SAED patterns, XRD patterns are indexed to monoclinic structure with 7M superstructural ordering for the B-0, B-0.5 and 5M superstructural ordering for B-1.0 alloys.

Boron addition to $Ni_{53.5}Mn_{26.0}Ga_{20.5}$ alloy is found to alter the microstructure of the parent alloy by decreasing the martensitic twin widths substantially. Multimode twinning is retained and segregation of a second phase is caused at the grain boundaries on boron addition, as shown in Fig. 7.3 for B-0.5 alloy. Refinement of grain size and the volume fraction of second phase are found to increase with boron content.

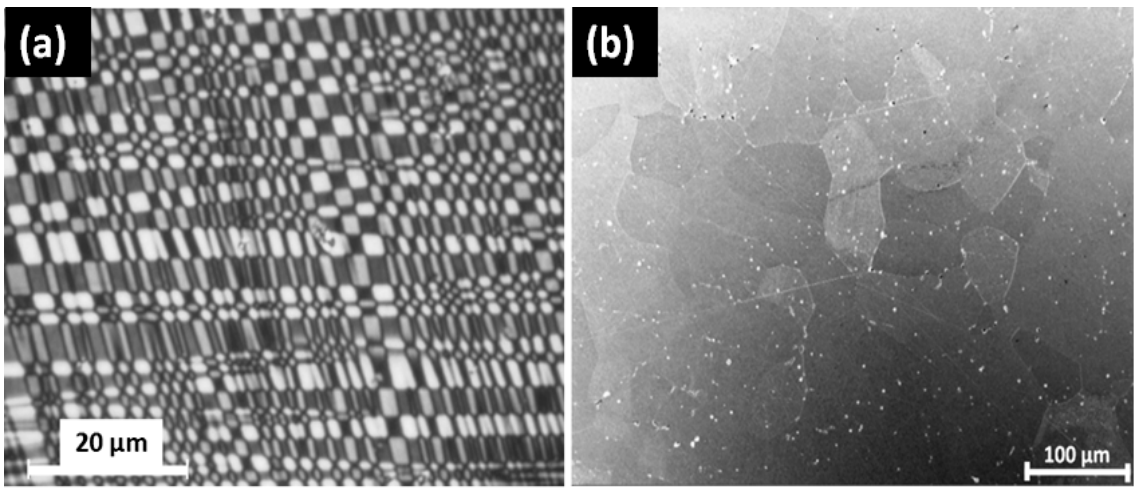

Fig. 7.3. (a) Optical microstructure at RT in B-0.5 alloy showing multimode twinning. (b) shows the FESEM micrograph of B-0.5 alloy showing grain refinement and small amount of second phase segregation on boron addition.

Multimode twinning is suppressed in B-1.0 alloy. Microstructures in Fig. 7.4 show substantial second phase segregation at the grain boundaries in this alloy. Detailed compositional analysis was carried out in the matrix as well as the second phase, using EDS facility on FESEM. The results reveal that the second phase regions in the boron containing samples are richer in Ni and poorer in Ga compared to the bulk compositions of the alloys.

Addition of boron had caused a considerable reduction in the martensitic transformation temperature and a marginal increase in the Curie temperature. These variations with boron content are attributed to the observed compositional shift that has rendered the matrix phase deficient in Ni content.

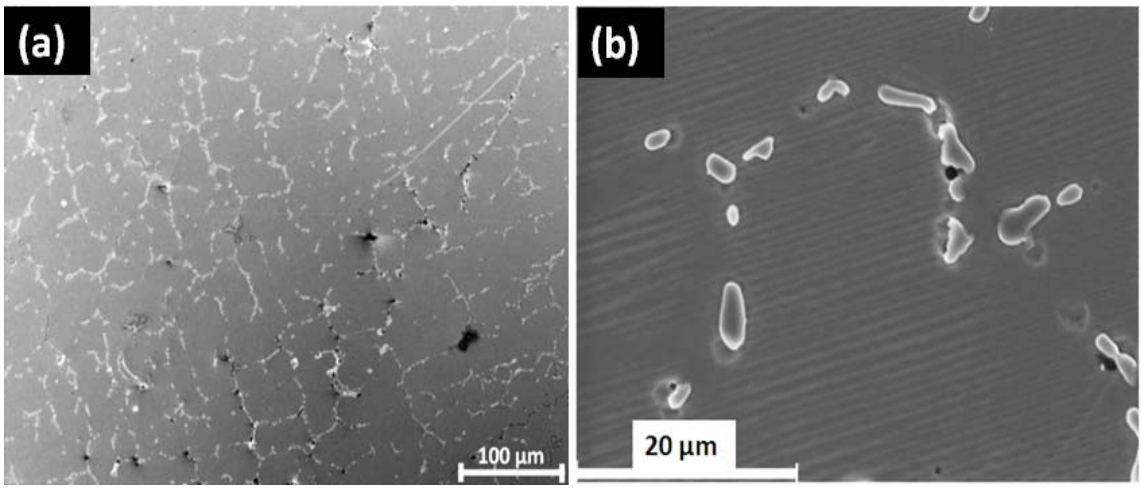

Fig. 7.4. FESEM micrographs recorded at (a) low and (b) high magnifications in B-1.0 alloy. Grain refinement and enhanced second phase segregation at the grain boundaries are evident from the figure, with boron content.

Results from systematic investigations on the magnetic properties and the mechanical properties like Vickers microhardness, compressive stress-strain and shape memory behavior of boron containing alloys derived from $Ni_{53.5}Mn_{26.0}Ga_{20.5}B_x$ are presented in Chapter 5. The M-H isotherms recorded at 5 K with boron content are shown in Fig. 7.5. (a) for the alloys of $Ni_{53.5}Mn_{26.0}Ga_{20.5}B_x$.

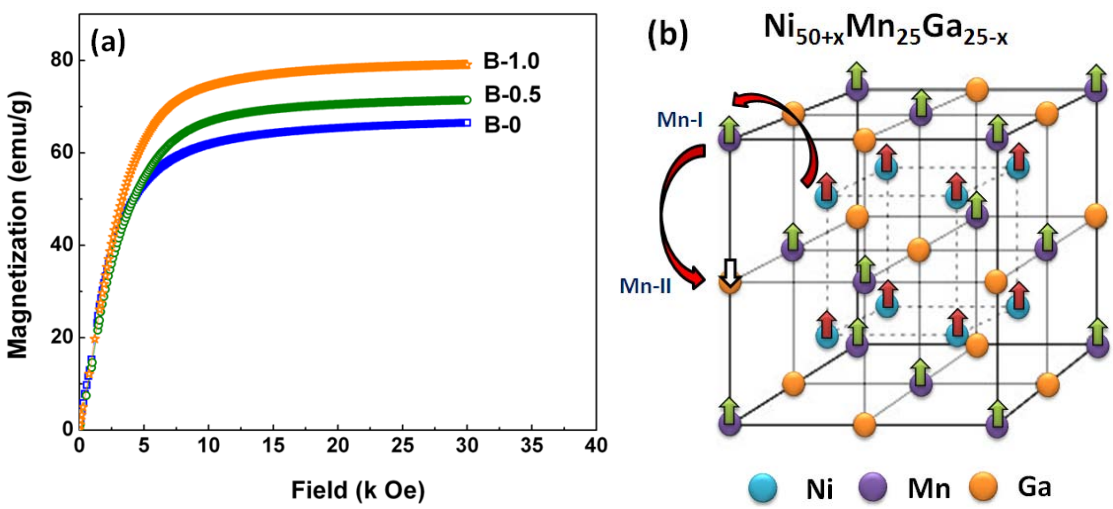

Fig. 7.5. (a) Magnetic isotherms recorded at 5 K for $Ni_{53.5}Mn_{26.0}Ga_{20.5}B_x$ alloys up to a magnetic field of 3 T. A significant increase in M_{sat} can be observed on boron addition. (b) Schematic representation of arrangement of magnetic moments

and their order in the case of off-stoichiometric Ni-excess alloys of $Ni_{50+x}Mn_{25}Ga_{25-x}$.

The saturation magnetization M_{sat} at 5 K increases with boron content from nearly 66.5 emu/g for B-0 alloy to 79.1 emu/g for B-1.0 alloy which corresponds to a change from 2.86 to 3.40 in units of μ_B per formula unit (μ_B /f.u.), and is quite a significant rise. In the case of off-stoichiometric Ni- rich compositions of Ni-Mn-Ga, Richard *et al.* [34] have shown that for Ni concentration of 50 at.% or more, the excess Ni displaces the Mn atoms from their regular sites (in Mn sublattice) and couple ferromagnetically with Mn moments. The excess Mn and the displaced Mn atoms occupy vacant Ga sites and couple antiferromagnetically to the Mn at regular sites. This picture is illustrated in Fig. 7.5 (b) which shows the arrangement of magnetic moments and their order in $Ni_{50+x}Mn_{25}Ga_{25-x}$ system.

A reduction in the Ni content from 53.3 at.% in the matrix of the B-0 alloy to 52.1 at.% in the B-0.5 and 51.6 at.% in B-1.0 alloys is expected to modify the net Mn atoms at Ga sites, compared to those in B-0 alloy. In other words, a reduction in the excess Ni content in the matrix would imply a decrease in the number of Mn atoms displaced to Ga site with antiferromagnetic order. This would result in an effective increase in magnetization per unit cell on boron addition.

Boron addition to $Ni_{53.5}Mn_{26.0}Ga_{20.5}$ alloy is found to modify the microstructure and mechanical properties substantially. Multimode twinning and shape memory effect were retained in B-0.5 alloy and were suppressed in B-1.0 alloy. Higher compression stress observed in B-0.5 alloy is attributed to grain refinement. Larger amounts of second phase segregation have led to easy deformation at lower stresses in B-1.0 alloy.

Maximum compression strengths of 124 MPa, 198 MPa and 111 MPa and corresponding compression strains of 5.2 %, 4.3 % and 5.5 % respectively have been recorded for B-0, B-0.5 and B-1.0 alloys as can be seen in Fig. 7.6.

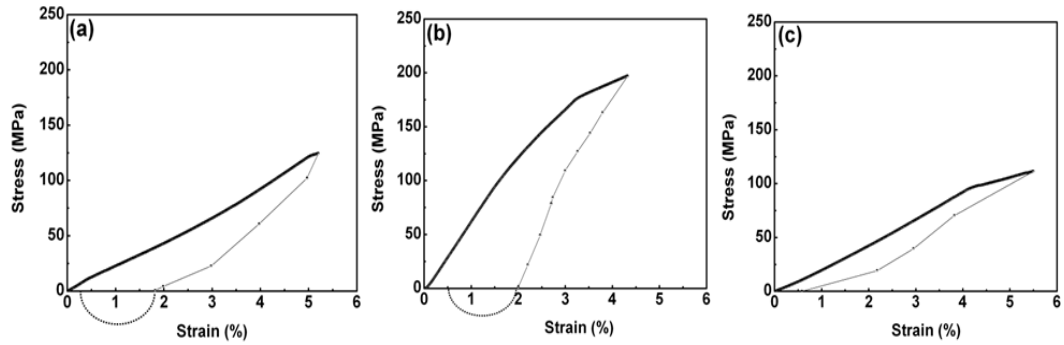

Fig. 7.6. (a)-(c) Compressive stress-strain curves recorded at RT in B-0, B-0.5 and B-1.0 alloys, respectively. The strain recovery on heating the samples to 150 ^{o}C after unloading, is indicated as dashed line.

EBSD studies reported in polycrystalline Ni-Mn-Ga alloys under compression [35], have confirmed that most of the compressive strain is due to motion of twin boundaries within the grains and that the grain boundaries impede twin boundary motion preventing a complete reorientation close to the grain boundaries (gbs); i.e. grain boundaries acts as a barrier for twin boundary motion and hence more stress is required to extend the detwinned region closer to the gbs. The higher compression stress observed for B-0.5 alloy, compared to B-0 is attributed to grain refinement. In the case of B-1.0 alloy substantial deformation occurs in B-1.0 even at low stresses, in spite of reduced grain size. The easy deformation observed to higher compressive strain, at relatively lower stresses compared to B-0.5, is believed to have its origin in the second phase segregation at the grain boundaries. Similar enhancement in compressive ductility was observed in Fe- and rare-earth doped $Ni_{50}Mn_{30}Ga_{20}$ alloy which was attributed to large amount of precipitation of second phase at the grain boundaries [36].

Considerable shape memory effect was observed in both B-0 and B-0.5 alloys which showed long range twin deformation. SME of close to 1.5% observed in B-0 alloy was retained even after an addition of 0.5 at.% boron. This was not affected by small amounts of second phase segregation at grain boundaries. In the case of B-1.0 alloy, though the deformation during detwinning was larger and occurred at lower stresses compared to B-0.5, the SME was reduced to 0.4%. This

is believed to be due to the proximity of T_M of the matrix phase in B-1.0 alloy to RT at which SME properties are measured.

The widths of the relief patterns that appeared in B-0 and B-0.5 alloys during microhardness measurements are found to be correlated to the twin widths observed in their optical micrographs. The measured Vickers hardness and the volume fraction of second phase seem to have similar variation with boron content. The hardness values of the compositions studied are in the range 290 - 309 kg-f/mm^2 for 1000 gf load, and are much higher compared to the values reported for Ni-Mn-Ga alloys in the martensitic phase [37]. From various results presented above we conclude that B-0.5 alloy with larger compression strength, substantial shape memory effect and higher hardness has a potential for shape memory applications at room temperature.

Chapter 6 presents a modified scheme to compute electron concentration, which can predict the martensitic transformations of Ni-Mn-Ga-Co and Ni-Mn-Al alloys effectively. Many reports in literature on off-stoichiometric Ni-Mn-Ga alloys show that T_M can be correlated to the e/a ratio. The T_M with e/a shows a linear dependence in off-stoichiometric Ni-Mn-Z (Z = Ga, Sb, Sn and In) alloys [3, 9, 11, 38, 39] and Ni-Mn-Al [40, 41] alloys. This can be used as a guide to predict the variations in T_M, on substitution of another element in Ni-Mn-Ga alloys. However, several groups reported an anomaly in the correlation of T_M with e/a in the case of quasi-ternary Ni-Mn-Ga-Fe [15, 42, 43] system. The usual trend of T_M with e/a is ineffective in the case of isoelectronic compounds like Ni-Mn-Ga-In [44].

We propose in this work, a new scheme of counting modified electron concentration to resolve the anomaly, based on Pauling's ideas on the electronic structure of metallic elements. For this, Miedema's electron density parameters N_{ws} are taken as accurate valences of metallic elements and are considered to be the number of bonding electrons, which contribute only to cohesion. Only the non-bonding electrons, $e_n = E - N_{ws}$ are considered relevant in computing the modified electron per atom ratio (N_e/a) of the compounds,

instead of e/a which is calculated from E, the total number of electrons outside the rare gas shell.

In off-stoichiometric Ni-Mn-Ga, Ni-Mn-Al and Co substituted Ni-Mn-Ga systems, T_M followed the expected linear trend with e/a, whereas for Fe doped Ni-Mn-Ga alloys, anomalous deviation from this trend is demonstrated as discussed in literature. We show systematic variations of T_M with N_e/a for a large number of compounds consisting of the off-stoichiometric alloys of Ni-Mn-Ga and Ni-Mn-Al, and quasi-ternary alloys of Ni-Mn-Ga with Co, Fe, and In substitutions. The anomaly observed for Fe containing alloys with e/a disappears, and a systematic dependence is observed when T_M is plotted against N_e/a with improved regression factor as shown in Fig. 7.7.

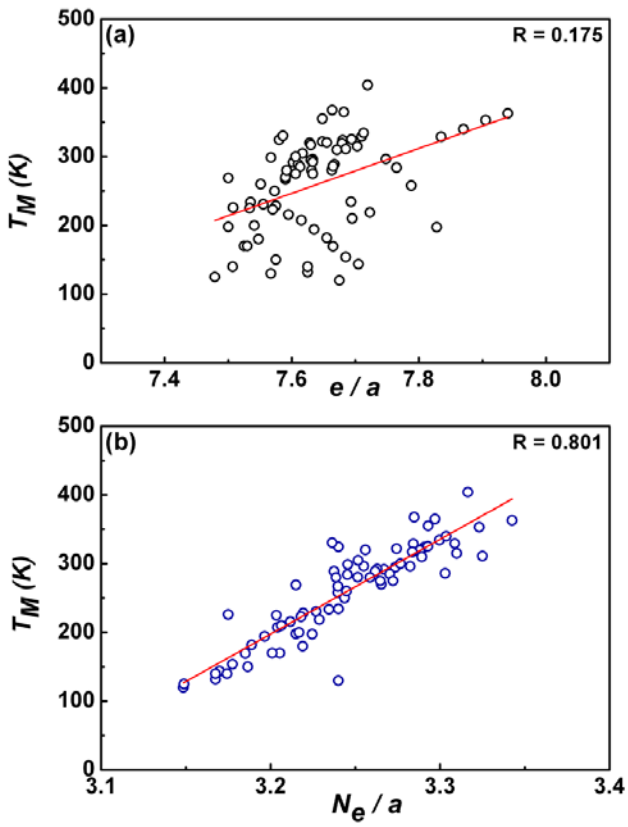

Fig. 7.7. (a) Martensitic transformation temperature T_M is plotted against e/a for 76 quasi-ternary Fe-doped Ni-Mn-Ga compounds. No systematic dependence is observed, (b) T_M vs. N_e/a plot for the same compounds shows a linear dependence with high regression factor, unlike the plot in (a).

It is also shown that T_M can be predicted for alloys with isoelectronic substitutions like in Ni-Mn-Ga-In system. The present results suggest that the non-bonding electron concentration can be used to successfully predict T_M of shape memory alloys of Ni-Mn-Ga system.

References

[1] K. Ullakko, J.K. Huang, C. Kantner, R.C. O' Handley and V.V. Kokorin, *Appl. Phys. Lett.* **69** (1996) 1966.

[2] S.J. Murray, M. Marioni, S.M. Allen, R.C. O' Handley and T.A. Lograsso, *Appl. Phys. Lett.* **77** (2000) 886.

[3] A. Planes, L. Manosa and M. Acet, *J. Phys.: Condens. Matter* **21** (2009) 233201.

[4] M. Zeng, S. Wing Or, Z. Zhu and S.L. Ho, *J. Appl. Phys.* **108** (2010) 053716.

[5] Y. Ma, C. Jiang, Y. Li, H. Xu, C. Wang and X. Liu, *Acta Mater.* **55** (2007) 1533.

[6] J. Pons, V.A. Chernenko, R. Santamarta and E. Cesari, *Acta Mater.* **48** (2000) 3027.

[7] A. Sozinov, A.A. Likhachev, N. Lanska and K. Ullakko, *Appl. Phys. Lett.* **80** (2002) 1746.

[8] O. Söderberg, Y. Ge, A. Sozinov, S-P. Hannula and V. K. Lindroos, *Smart Mater. Struct.* **14** (2005) S223.

[9] V.V. Khovaylo, V.D. Buchelnikov, R. Kainuma, V.V. Koledov, M. Ohtsuka, V.G. Shavrov, T. Takagi, S.V. Taskaev and A.N. Vasiliev, *Phys. Rev. B* **72** (2005) 224408.

[10] V.A. Chernenko, E. Cesari, V.V. Kokorin, I.N. Vitenko, *Scripta Metall. Mater.* **33** (1995)1239.

[11] N. Lanska, O. Söderberg, A. Sozinov, Y. Ge, K. Ullakko and V.K. Lindroos, *J. Appl. Phys.* **95** (2004) 8074.

[12] I. Glavatskyy, N. Glavatska, O. Söderberg, S-P. Hannula and J-H. Hoffmann, *Scripta Mater*. **54** (2006) 1891.

[13] D.Y. Cong, S. Wang, Y.D. Wang, Y. Ren, L. Zuo and C. Esling, *Mater. Sci. Eng. A* **473** (2008) 213.

[14] A. Satish Kumar, M. Ramudu and V. Seshubai, *J. Alloys Compd.* **509** (2011) 8215.

[15] D. Kikuchi, T. Kanomata, Y. Yamaguchi, H. Nishihara, K. Koyama and K. Watanabe, *J. Alloys Compd.* **383** (2004) 184.

[16] D. Kikuchi, T. Kanomata, Y. Yamaguchi and H. Nishihara, *J. Alloys Compd.* **426** (2006) 223.

[17] D.E. Soto-Parra, F. Alvarado-Hernandez, O. Ayala, R.A. Ochoa-Gamboa, H. Flores-Zúñiga and D. Rios-Jara, *J. Alloys Compd.* **464** (2008) 288.

[18] K. Tsuchiya, A. Tsutsumi, H. Ohtsuka and M. Umemoto, *Mater. Sci. Eng. A* **378** (2004) 370.

[19] B.R. Gautam, I. Dubenko, A.K. Pathak, S. Stadler and N. Ali, *J. Mag. Mag. Mater.* **321** (2009) 29.

[20] B.R. Gautam, I. Dubenko, A.K. Pathak, S. Stadler and N. Ali, *J. Phys: Condens. Matter* **20** (2008) 465209.

[21] H. Luo, F. Meng, Q. Jiang, H. Liu, E. Liu, G. Wu and Y. Wang, *Scripta Mater.* **63** (2010) 569.

[22] K. Aoki and Izumi, *Nippon Kinzoku Gakkaishi* **43** (1979) 1190.

[23] C.T. Liu, C.L. White and J.A. Horton, *Acta Mater.* **33** (1985) 213.

[24] M.A. Morris, *Scripta Mett. Mater.* **25** (1991) 2541.

[25] M.A. Morris, *Acta Mater.* **39** (1991) 1573.

[26] S.M. Tuominen and R.J. Biermann, *J. Met.* **40** (2) (1988) 32.

[27] W.S. Yang and D.E. Mikkola, *Scripta. Mett. Mater.* **28** (1993) 161.

[28] Y. Suzuki, Ya Xu, S. Morito, K. Otsuka and K. Mitose, *Mater. Lett.* **36** (1998) 85.

[29] H. B. Wang, F. Chen, Z. Y. Gao, W. Cai and L. C. Zhao, *Mater. Sci. Eng. A* **438-440** (2006) 990.

[30] J. Sui, X. Zhang, L. Gao and W. Cai, *J. Alloys Compd.* **509** (2011) 8692.

[31] L. Gao, W. Cai, A. L. Liu and L. C. Zhao, *J. Alloys Compd.* **425** (2006) 314.

[32] M. Nishida, H. Ohgi, I. Itai, A. Chiba and K. Yamauchi, *Acta Metall. Mater.* **43** (1995) 1219.

[33] K. Bhattacharya, *Microstructure of Martensite*, (Oxford University Press, Oxford, 2003), p. 83.

[34] M.L. Richard, J. Feuchtwanger, S.M. Allen, R.C. O'Handley, P. Lázpita, J.M. Barandiaran, J. Gutierrez, B. Ouladdiaf, C. Mondelli, T. Lograsso and D. Schlagel, *Phil. Mag.* **87** (2007) 3437.

[35] R. Chulist, M. Pötschke, T. Lippmann, C-G..Oertel and W. Skrotzki, *J. Phys.: Conference Series* **240** (2010) 012024.

[36] R. K. Singh, M. Manivel Raja, R. P. Mathur and M. Shamsuddin, *J. Alloys Compd.* **506** (2010) 73.

[37] X. W. Liu, O. Söderberg, K. Koho, N. Lanska, Y. Ge, A. Sozinov and V. K. Lindroos, *Wear* **258** (2005) 1364.

[38] V. A. Chernenko, *Scripta Mater.* **40** (1999) 523.

[39] X.Q. Chen, F.J. Yang, X. Lu and Z.X. Qin, *Phys. Stat. Sol. (b)* **244** (2007) 1047.

[40] R. Kainuma, H. Nakano and K. Ishida, *Metall. Mater. Trans.* **27A** (1996) 4153.

[41] R. Kainuma, W. Ito, R.Y. Umetsu, K. Oikawa and K. Ishida, *Appl. Phys. Lett.* **93** (2008) 091906.

[42] D.E. Soto-Parra, X. Moya, L. Mañosa, A. Planes, H. Flores-Zúñiga, F. Alvarado Hernández, R.A. Ochoa-Gamboa, J.A. Matutes-Aquino and D. Ríos-Jara, *Phil. Mag.* **90** (2010) 2771.

[43] Z.H. Liu, M. Zhang, W.Q. Wang, W.H. Wang, J.L. Chen, G.H. Wu, F.B. Meng, H.Y. Liu, B.D. Liu, J.P. Qu and Y.X. Li, *J. Appl. Phys.* **92** (2002) 5006.

[44] M. Khan, I. Dubenko, S. Stadler and N. Ali, *J. Phys.: Condens. Matter.* **16** (2004) 5259.

Fig. No.	Figure Caption

Chapter – 1

Chapter – 2

Chapter – 3

Chapter – 4

Chapter – 5

Fig. 5.5 The micrographs recorded using FESEM at lower and higher magnifications (shown in Fig. 4.4) for B-0, B-0.5 and B-1.0 alloys are reproduced here. A comparison of (e) & (f) with (c) & (d) reveals that considerable increase in grain boundary segregation occurs with boron content. No such segregation is seen in (a) and (b) for B-0 alloy. Typically, 1 and 2 indicate regions of second phase while 3 indicates a region in the matrix, chosen for compositional analysis.

Fig. 5.6 (a)-(c) Compressive stress-strain curves recorded at RT in B-0, B-0.5 and B-1.0 alloys, respectively. The strain recovery on heating the samples to 150 ^{o}C after unloading is indicated as dashed line. (d) shows that the general trend of variation in T_M and T_C on e/a is followed, when e/a is computed using composition of the matrix phase. T_M and T_C of Ni_2MnGa are also included in the plot.

Fig. 5.7 Optical micrographs of the samples after indentation at 500 gf and 1000 gf loads in B-0, B-0.5 and B-1.0 alloys. (a) and (b) show the relief patterns around the indentation in B-0 alloy, (c) and (d) show the relief patterns with finer twins around the indentation in B-0.5 alloy and (e) and (f) show no relief patterns even after application of 1000 gf load in B-1.0 alloy. (g) shows the variation of Vickers microhardness determined on application of 1000 gf load and that of volume fraction of second phase segregation, with boron content.

Chapter – 6

Fig. 6.1 Variation of $(E - N_{ws})$ with E showing a non-linear relation between them. The curve drawn is a fit to a polynomial.

Fig. 6.2 (a) The variation of martensitic transformation temperature T_M in off-stoichiometric Ni-Mn-Ga alloys with e/a. 141 alloys with $e/a \leq 7.72$ shows a linear dependence (filled circles). Open circles represent Ni-excess compositions with $T_M > T_C$. $Ni_{50+x}Mn_{25}Ga_{25-x}$ (x = 2-11) compositions with ≥ 57 at. % Ni, represented by open squares (red online) reveal γ- phase precipitation in their microstructure, and hence T_M remains constant with e/a. (b) T_M vs. N_e/a plot for the above alloys shows a dependence similar to that observed in (a). The solid lines shown in the figure, in the three regions, are guide to the eye.

Fig. 6.3 (a) The variation of martensitic transformation temperature T_M plotted for 84 quasi-ternary Co-doped Ni-Mn-Ga alloys showing a linear dependence with e/a, (b) T_M vs N_e/a for the above compounds showing a similar linear dependence as observed in (a).

Fig. 6.4 (a) The variation of martensitic transformation temperature T_M plotted for 12 off-stoichiometric Ni-Mn-Al alloys with e/a exhibiting a linear dependence, (b) T_M vs N_e/a plot also shows a similar linear dependence as observed in (a).

Fig. 6.5 (a) Martensitic transformation temperature T_M is plotted against e/a for 76 quasi-ternary Fe-doped Ni-Mn-Ga compounds. No systematic dependence is observed, (b) T_M vs. N_e/a plot for the same compounds shows a linear

dependence with high regression factor, unlike the plot in (a).

Fig. 6.6 (a) Variation of martensitic transformation temperature T_M plotted for quasi-ternary $Ni_2MnGa_{1-x}In_x$ compounds, with e/a. No useful conclusion can be drawn from the figure since the valences for both Ga and In are the same, thus leading to a constant e/a for all the compounds, (b) T_M vs. N_e/a plot for the compounds is linear and the graph can be used to predict the T_M of new compounds belonging to the same system. Variation of T_M with electron concentration per unit volume N_e/V for (c) quasi-ternary Ni-Mn-Ga-Co alloys and (d) for $Ni_2MnGa_{1-x}In_x$ alloys, respectively. The change in trend of (b) and (d) confirm the role of volume effects.

Chapter – 7

Fig. 7.1 Optical microstructure of the $Ni_{53.5}Mn_{26.0}Ga_{20.5}$ alloy recorded at RT showing multimode twinning including crossing twins, parallel bands and twins within twins as shown in (a), (c) and (d).

Fig. 7.2 Powder X-ray diffraction patterns recorded at ambient temperature. Based on the results from SAED patterns, XRD patterns are indexed to monoclinic structure with 7M superstructural ordering for the B-0, B-0.5 and 5M superstructural ordering for B-1.0 alloys.

Fig. 7.3 (a) Optical microstructure at RT in B-0.5 alloy showing multimode twinning. (b) shows the FESEM micrograph of B-0.5 alloy showing grain refinement and small amount of second phase segregation on boron addition.

Fig. 7.4 FESEM micrographs recorded at (a) low and (b) high magnifications in B-1.0 alloy. Grain refinement and enhanced second phase segregation at the grain boundaries are evident from the figure, with boron content.

Fig. 7.5 (a) Magnetic isotherms recorded at 5 K for $Ni_{53.5}Mn_{26.0}Ga_{20.5}B_x$ alloys up to a magnetic field of 3 T. A significant increase in M_{sat} can be observed on boron addition. (b) Schematic representation of arrangement of magnetic moments and their order in the case of off-stoichiometric Ni-excess alloys of $Ni_{50+x}Mn_{25}Ga_{25-x}$.

Fig. 7.6 (a)-(c) Compressive stress-strain curves recorded at RT in B-0, B-0.5 and B-1.0 alloys, respectively. The strain recovery on heating the samples to 150 ^oC after unloading is indicated as dashed line.

Fig. 7.7 (a) Martensitic transformation temperature T_M is plotted against e/a for 76 quasi-ternary Fe-doped Ni-Mn-Ga compounds. No systematic dependence is observed, (b) T_M vs. N_e/a plot for the same compounds shows a linear dependence with high regression factor, unlike the plot in (a).

TABLE CAPTIONS

List of publications

❖ Publications in Journals

[1] **M. Ramudu**, A. Satish Kumar and V. Seshu Bai "Influence of boron addition on the microstructural, structural and magnetic properties of $Ni_{53.5}Mn_{26.0}Ga_{20.5}$ alloys. (*Intermetallics* – Under Revision)

[2] **M. Ramudu**, A. Satish Kumar, V. Seshu Bai, K. Muraleedharan, K.S. Prasad and T. Rajasekharan "Modulated monoclinic crystal structure and large shape memory effect in nickel-rich $Ni_{53.5}Mn_{26.0}Ga_{20.5}$" *Scripta Materialia* 63 (2010) 1073.

[3] A. Satish Kumar, **M. Ramudu** and V. Seshubai "Site preference of magnetic atoms in Ni–Mn–Ga–M (M=Co, Fe) ferromagnetic shape memory alloys" *Phys. Status Solidi B*, 1–7 (2011) / DOI 10.1002/pssb.201147398

[4] A. Satish Kumar, **M. Ramudu** and V. Seshubai "Effect of selective substitution of Co for Ni or Mn on the superstructure and microstructural properties of $Ni_{50}Mn_{29}Ga_{21}$" *Journal of Alloys and Compounds* 509 (2011) 8215– 8222.

[5] A. Satish Kumar, **M. Ramudu** and V. Seshubai "Structural and magnetic investigations in the vicinity of first order transformations in Ni-Mn-Ga-Co ferromagnetic shape memory alloys" (Submitted to *Phase transitions*)

[6] **M. Ramudu**, A. Satish Kumar and V. Seshu Bai "Influence of boron addition on the microstructural and mechanical properties of $Ni_{53.5}Mn_{26.0}Ga_{20.5}$ alloys. (Under preparation)

[7] V. Seshubai, **M. Ramudu**, A. Satish Kumar and T. Rajasekharan "Counting non-bonding electrons to predict martensitic transformation temperatures in Ni—Mn—Ga—X alloys" (Under preparation)

[8] A. Satish Kumar, **M. Ramudu** and V. Seshu Bai "Microstructural evolution on annealing and its correlation to structural and magnetic properties of melt-spun $Ni_{50}Mn_{29}Ga_{21}$ ribbons" (Under preparation)

[9] A. Satish Kumar, **M. Ramudu** and V. Seshu Bai "0.7 % magnetic field induced strain in polycrystalline $Ni_{50}Mn_{29}Ga_{21}$ ferromagnetic shape memory alloy" (Under preparation)

Publications in the International/National Symposia/Workshops

[1] **M. Ramudu**, A. Satish Kumar and V. Seshubai "Structural and magnetic properties of ferromagnetic shape memory alloys of Ni-Mn-Ga system" Proceedings of International Conference on Condensed Matter Physics (ICCMP-2007) Page 89, November 25-28, 2007, Jaipur, India

[2] **M. Ramudu**, A. Satish Kumar and V. Seshubai "Low field magnetic entropy change in $Ni_{53.5}Mn_{26.0}Ga_{20.5}$ alloy" Proceedings of 54th DAE-Solid State Physics Symposium, Page 1025, December 14-18, 2009, Vadodara, India

[3] **M. Ramudu**, A. Satish Kumar and V. Seshubai "Effect of Boron addition on microstructural and microhardness properties of $Ni_{53.5}Mn_{26.0}Ga_{20.5}B_x$ (x = 0, 0.5, and 1) alloys" India-Singapore Joint Physics Symposium 2010 (ISJPS-2010), February 19-21, 2010 University of Hyderabad, Hyderabad.

[4] **M. Ramudu**, A. Satish Kumar, S. Pavan Kumar Naik and V. Seshubai "Magnetocaloric and shape memory effects in nickel-rich $Ni_{53.5}Mn_{26}Ga_{20.5}$ alloys" Andhra Pradesh Science Congress 2011(APSC-2011), Page 61, November 14-16, 2011 GITAM University, Vishakhapatnam

[5] A. Satish Kumar, **M. Ramudu** and V. Seshubai "Magnetic properties of (Ni, Co) – Mn – Ga" Proceedings of International Conference on Condensed Matter Physics (ICCMP-2007) Page 26, November 25-28, 2007, Jaipur, India

[6] A. Satish Kumar, **M. Ramudu** and V. Seshubai "Structural and magnetic properties of nano MnSb" International Conference on Recent Trends in Nanostructured Materials and Their Applications (*ICRNM-2008*),*Osmania University*, Hyderabad**.**

[7] A. Satish Kumar, **M. Ramudu** and V. Seshubai "Magnetic properties of ferromagnetic shape memory Ni-Mn-Ga melt spun ribbon" India-Singapore Joint Physics Symposium 2010 (ISJPS-2010), February 19-21, 2010 University of Hyderabad, Hyderabad.

Workshops / Training courses attended

- "Workshop on Superconductivity" organized at University of Hyderabad during January 27-28, 2007.
- International Conference on Ferromagnetic Shape Memory Alloys (ICFSMA-2007) at S.N. Bose National Centre for Basic Sciences, Kolkata during November 14-16, 2007.
- "Workshop on Low Temperature Physics" Organized at School of Physics, University of Hyderabad during March 14-15, 2008.
- "University of Hyderabad – Tata Institute of Fundamental Research (UoH-TIFR) Interaction Meeting organized at University of Hyderabad, Hyderabad during August 20-22, 2009.
- India-Singapore Joint Physics Symposium 2010 (ISJPS-2010), organized at University of Hyderabad, Hyderabad during February 19-21, 2010.
- Workshop on "Physics at small scales" organized at School of Physics, University of Hyderabad during March 18-19, 2011.